

AD# 602438

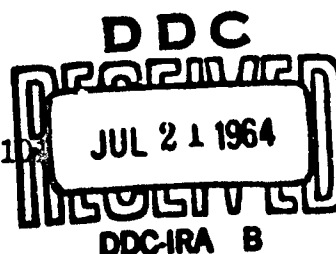
ML-TDR-64-57

RESEARCH OF DIELECTRIC MATERIALS

159 p \$5.00 lc  
\$1.00 mf  
TECHNICAL DOCUMENTARY REPORT NO. ML-TDR-64-57  
May 1964

AF Materials Laboratory  
Aeronautical Systems Division  
Air Force Systems Command  
Wright-Patterson Air Force Base, Ohio

Project No. 7371, Task No. 7371D1



(Prepared under Contract No. AF-33(657)-8825 by General Electric  
Research Laboratory, Schenectady, New York; J.C. Devins,  
H.L. Greenhaus, R.J. Wolff, D.R. Johnston,  
F.F. Carini, A. Pletenik, and  
H.G. Pfeiffer, authors)

19990503136

## NOTICES

When Government drawings, specifications, or other data are used for any purpose other than in connection with a definitely related Government procurement operation, the United States Government thereby incurs no responsibility nor any obligation whatsoever; and the fact that the Government may have formulated, furnished, or in any way supplied the said drawings, specifications, or other data, is not to be regarded by implication or otherwise as in any manner licensing the holder or any other person or corporation, or conveying any rights or permission to manufacture, use, or sell any patented invention that may in any way be related thereto.

Qualified requesters may obtain copies of this report from the Defense Documentation Center (DDC), (formerly ASTIA), Cameron Station, Bldg. 5, 5010 Duke Street, Alexandria 4, Virginia.

This report has been released to the Office of Technical Services, U.S. Department of Commerce, Washington 25, D.C., for sale to the general public.

Copies of this report should not be returned to the Research and Technology Division unless return is required by security considerations, contractual obligations, or notice on a specific document.

## FOREWORD

This report was prepared by the General Electric Research Laboratory under USAF Contract No. AF-33(657)-8825. This contract was continued under Project No. 7371, "Exploratory Development In Electronic and Magnetic Materials," Task No. 737101, "Dielectric and Optical Maser Materials." The work was administered under the direction of the AF Materials Laboratory, Research and Technology Division, with W.G.D. Frederick acting as project engineer.

This report covers work conducted from January 15, 1963, to January 15, 1964.

**BLANK PAGE**



## ABSTRACT

Phase I of this contract is concerned with electron impact ionization and attachment in polyatomic gases. In the first section, these processes have been examined using a mass spectrometer operating with a retarding potential difference electron source. In the second section, ionization and attachment coefficients have been measured using an electron swarm, or Townsend technique. Results were obtained principally with perfluorocarbon gases, many of which are of interest for use as high dielectric strength gases.

In Phase II, studies of the chemical degradation of materials under the action of corona, begun during our first contract, were continued. Besides continuing our studies on weight loss in Mylar, similar investigations were made on "H" film at the request of AF Materials Laboratory, Research and Technology Division. The chemical effects of different types of corona discharges, distinguished during our first contract, were studied on model compounds. By the use of d-c voltages it has been possible to compare damage caused by positive ion and electron bombardment.

This technical documentary report has been reviewed and is approved.



JULES I. WITTEBORT  
Chief, Thermal & Solid State Branch  
Materials Physics Division  
AF Materials Laboratory

## TABLE OF CONTENTS

### PHASE I. IONIZATION AND ELECTRON ATTACHMENT IN GASES

	<u>Page</u>
A. NEGATIVE ION MASS SPECTROMETRY .....	1
1. Introduction .....	1
2. Experimental Method .....	3
2.1 RPD Method .....	3
2.2 Electron Gun .....	6
2.3 Associated Electronic Equipment .....	7
3. Results and Discussion .....	8
REFERENCES .....	19
B. IONIZATION AND ATTACHMENT COEFFICIENTS .....	35
1. Introduction .....	35
2. Analysis of Data .....	38
3. Purity of Materials .....	39
4. Ionization Potentials .....	39
5. Results on Perfluoroalkanes .....	40
6. Comparison with Breakdown Measurements .....	41
7. Dependence on Pressure .....	43
8. Octafluorocyclobutane .....	44
9. Hexafluoropropene .....	44
10. <u>t</u> -Butyl Chloride .....	45
11. Discussion of Results .....	45
12. Conclusions .....	51
APPENDIX .....	53
REFERENCES .....	54

PHASE II. CHEMICAL EFFECTS OF CORONA ON MATERIALS

A. STUDIES OF CORONA DAMAGE TO MATERIALS USING POSITIVE AND NEGATIVE D-C DISCHARGES .....	79
1. Introduction .....	79
2. Experimental Method .....	80
3. Results .....	82
3.1 Stearyl Alcohol and Eicosane .....	82
3.2 Townsend-like Discharge on Dotriacontane .....	84
3.3 Streamerlike Discharge on Dotriacontane .....	85
B. CORONA EFFECTS IN COAXIAL CORONA CELLS .....	91
1. Introduction .....	91
2. Experimental .....	91
3. Discussion of Results .....	92
4. Life Tests on Insulation Systems .....	95
5. Conclusions .....	96
REFERENCES .....	97
C. SUMMARY AND CONCLUSIONS .....	129

# LIST OF TABLES

<u>Table</u>		<u>Page</u>
I-1	Negative Ions in Perfluoropropane, $C_3F_8$ . . . . .	21
I-2	Measured Negative and Positive Ion Appearance Potentials in $C_3F_8$ . . . . .	21
I-3a	Negative Ions from $C_2F_6$ . . . . .	22
I-3b	Negative Ion Appearance Potentials in $C_2F_6$ . . . . .	22
I-4	Negative Ions in Perfluorobutane, $C_4F_{10}$ . . . . .	22
I-5	Negative Ions in Perfluorohexane, $C_6F_{14}$ . . . . .	23
I-6	Materials Used in This Work . . . . .	57
I-7	Ionization Potentials of Gases Used in This Work . . . . .	57
I-8	Ionization and Attachment Coefficients for Tetrafluoromethane . . . . .	53
I-9	Ionization and Attachment Coefficients for Hexafluoroethane . . . . .	58
I-10	Ionization and Attachment Coefficients for Octafluoropropane . . . . .	59
I-11	Ionization and Attachment Coefficient for Decafluorobutane . . . . .	59
I-12	Ionization and Attachment Coefficients for Tetradecafluorohexane . . . . .	60
I-13	Values of B and Composite Cross Sections . . . . .	61
I-14	Pressure Dependence of the Ionization and Attachment Coefficient for Decafluorobutane . . . . .	61
I-15	Ionization and Attachment Coefficients for Octafluorocyclobutane . . . . .	62
I-16	Ionization and Attachment Coefficients for Hexafluoropropene . . . . .	62
I-17	Ionization and Attachment Coefficients for <u>t</u> -Butyl Chloride . . . . .	63
I-18	Limiting Value for Attachment Coefficients at High Pressure and the Transition Pressure . . . . .	63
II-1	Corona Damage to Eicosane . . . . .	99
II-2	Corona Damage to Eicosane . . . . .	99
II-3	Townsend Pulse Bombardment of Dotriacontane Film . . . . .	100

List of Tables (continued)

<u>Table</u>		<u>Page</u>
II-4	Electron and Ion Streamer Discharges on Dotriacontane . . . . .	100
II-5	Streamer Bombardment of Dotriacontane. Stagnant Air in Cell . . . . .	101
II-6	Streamer Bombardment of Dotriacontane. Flowing Air Through Cell . . . . .	101
II-7	Number of Streamer Pulses Per Minute with Air Flowing . . . . .	102
II-8	Streamer Bombardment of Radioactive Dotriacontane in Flowing N <sub>2</sub> . . . . .	102
II-9	Average Voltage across a 0.22-mm Gap During Corona Discharges . . . . .	103
II-10	Changes in $\delta\sigma_a$ as a Function of Pressure and Temperature . . . . .	104
II-11	Corona Damage to "H" Film. . . . .	104
II-12	Rate of Weight Loss/Corona Energy at 22° and 124°C. "H" Film . . . . .	105
II-13	Life Test of Insulation Systems . . . . .	105

# LIST OF FIGURES

<u>Figure</u>		<u>Page</u>
I-1	Schematic Diagram of Mass Spectrometer Ion Source. . . . .	25
I-2	Stopping Potential Curve for the Electron Current Associated with the RPD Method and Derived Electron Distribution . . . . .	25
I-3	$\text{SF}_6^-$ Difference Ion Current as a Function of Electron Accelerating Voltage Employing RPD Method . . . . .	26
I-4	Ionization Efficiency Curve for $\text{A}^+$ in Argon. . . . .	26
I-5	Cross-Sectional Drawings of Mass Spectrometer Ion Source. . . . .	27
I-6	A--Cross Section Through Electron Gun Slits Viewed Toward Top Plate; B--First Electron Gun Slit and Filament Assembly . . . . .	27
I-7	Eighty-Volt RPD Supply for Electron Gun . . . . .	28
I-8	Ionization Efficiency Curves for $\text{SF}_6^-$ , $\text{F}^-$ , $\text{CF}_3^-$ , and $\text{C}_2\text{F}_5^-$ in Sulfur-Hexafluoride- $\text{C}_3\text{F}_8$ Mixture. . . . .	29
I-9	Ionization Efficiency Curves for $\text{A}^+$ and $\text{CF}_3^+$ , $\text{C}_2\text{F}_5^+$ and $\text{C}_3\text{F}_7^+$ in an Argon- $\text{C}_3\text{F}_8$ Mixture . . . . .	30
I-10	Ionization Efficiency Curve for $\text{F}^-$ and $\text{CF}_3^-$ in Perfluoroethane, $\text{C}_2\text{F}_6$ . . . . .	30
I-11	Negative Ion Current-Electron Energy Curves for $\text{CF}_4$ . . . . .	31
I-12	Negative Ion Current-Electron Energy Curves for $\text{C}_2\text{F}_6$ . . . . .	31
I-13	Negative Ion Current-Electron Energy Curves for $\text{C}_3\text{F}_8$ . . . . .	32
I-14	Negative Ion Current-Electron Energy Curves for $\text{C}_4\text{F}_{10}$ . . . . .	32
I-15	Negative Ion Current-Electron Energy Curves for $\text{C}_6\text{F}_{14}$ . . . . .	33
I-16	$\text{F}^-$ and Parent Molecule Ion Current-Electron Energy Curves for $\text{CF}_4$ Through $\text{C}_6\text{F}_{14}$ . . . . .	33
I-17	Cell for Measuring Ionization and Attachment Coefficients. . . . .	65
I-18	Dependence of Current on Gap for $\text{CF}_2\text{Cl}_2$ at Various Values of $E/P$ . . . . .	65

# List of Figures (continued)

<u>Figure</u>		<u>Page</u>
I-19	Dependence of Ionization Coefficients on P/E for the Perfluoroalkanes. . . . .	66
I-20	Relationship Between Composite Cross Section and Number of Carbon-Fluorine or Carbon-Hydrogen Bonds in the Alkanes . . . . .	67
I-21	Dependence of $(\alpha-\eta)/P$ on E/P for the Perfluoroalkanes. . . . .	67
I-22	Dependence of $\eta/P$ on E/P for the Perfluoroalkanes. . . . .	68
I-23	Dependence of $\eta/P$ Measured at the Limiting E/P on the Number of C-F Bonds for the Perfluoroalkanes. . .	68
I-24	Variation of $(E/P)_{lim}$ with Chain Length for the Perfluoroalkanes. . . . .	69
I-25	Comparison of Measured and Calculated Values Sparking Potential for the Perfluoroalkanes. . . . .	69
I-26	Dependence of $\alpha/P$ , $(\alpha-\eta)/P$ , and $\eta/P$ on Pressure for $C_4F_{10}$ at E/P of 125 Volts $cm^{-1}$ torr $^{-1}$ . . . . .	70
I-27	Dependence of $\alpha/P$ , $(\alpha-\eta)/P$ , and $\eta/P$ on Pressure for $C_4F_{10}$ at E/P of 150 Volts $cm^{-1}$ torr $^{-1}$ . . . . .	70
I-28	Comparison of the Dependence of $\alpha/P$ on P/E for Octafluorocyclobutane and Octafluoropropane. . . . .	71
I-29	Comparison of the Dependence of $(\alpha-\eta)/P$ on E/P for Octafluorocyclobutane and Octafluoropropane. . . . .	71
I-30	Comparison of the Dependence of $\eta/P$ on E/P for Octafluorocyclobutane and Octafluoropropane. . . . .	72
I-31	Comparison of Measured and Calculated Values of Sparking Potential for Octafluorocyclobutane . . . . .	72
I-32	Comparison of the Dependence of $\alpha/P$ on P/E for Hexafluoropropene and Hexafluoroethane. . . . .	73
I-33	Comparison of the Dependence of $(\alpha-\eta)/P$ on E/P for Hexafluoropropene and Hexafluoroethane. . . . .	73
I-34	Comparison of the Dependence of $\eta/P$ on E/P for Hexafluoropropene and Hexafluoroethane . . . . .	74
I-35	Dependence of $\alpha/P$ on P/E for <i>t</i> -Butyl Chloride. . . . .	74
I-36	Dependence of $(\alpha-\eta)/P$ on E/P for <i>t</i> -Butyl Chloride. . . . .	75
I-37	Comparison of $\eta/P$ for <i>t</i> -Butyl Chloride and Isopropyl Chloride. . . . .	75

List of Figures (continued)

<u>Figure</u>		<u>Page</u>
I-38	Maximum Relative Cross Sections for Negative Ion Formation as a Function of Chain Length in the Perfluoroalkanes. . . . .	76
I-39	Relative Cross Sections for Total Negative Ion Production as a Function of Electron Energy in the Perfluoroalkanes. . . . .	77
I-40	Dependence According to Theory of $\eta/P$ on $P$ for $C_4F_{10}$ . . . .	78
II-1	Corona Cell . . . . .	107
II-2	Schematic Diagram of the Corona Cell and Associated Equipment . . . . .	107
II-3	Dependence of Pulse Magnitude on Overvoltage for Various Electrode Separations. Townsend Discharges . .	108
II-4	Positive Ion Bombardment of Stearyl Alcohol: 50 Discharges/Sec; 4 Monolayers. Townsend Discharges. . . . .	108
II-5	Corona Damage to Radioactive Stearyl Alcohol. Streamer Discharges; 30-Mil Gap; 7.33 kv . . . . .	109
II-6	Corona Damage to Eicosane. . . . .	109
II-7	Per Cent Loss of Radioactivity of Eicosane Film. . . . .	110
II-8	Absolute Loss in Radioactivity of Eicosane Film with Corona Exposure . . . . .	110
II-9	Morphology of Dotriacontane Films on Glass Plate . . . . .	111
II-10	Electron and Ion Discharges of Dotriacontane: 15-Mil Gap; 7.33 kv. . . . .	111
II-11	Discharge Area of Electron Bombarded Sample of Dotriacontane 25X . . . . .	112
II-12	Electron and Ion Discharges on Dotriacontane: 30-Mil Gap; 7.33 kv. . . . .	112
II-13	Change of Pulse Size with Time . . . . .	113
II-14	Streamer Bombardment of Radioactive Dotriacontane. Air Flowing Through Cell . . . . .	113
II-15	Streamer Bombardment of Radioactive Dotriacontane. $N_2$ Flowing Through Cell. . . . .	114
II-16	Number of Discharges Per Minute During Aging Dotriacontane. $N_2$ Atmosphere . . . . .	114



# List of Figures (continued)

<u>Figure</u>		<u>Page</u>
II-17	Pulse Shapes for A--Ion Bombardment; B--Electron Bombardment of Dielectric; 5 volts/cm; 0.5 $\mu$ sec/cm . . . . .	115
II-18	Pulse Shapes for Ion Bombardment of Dielectric; 5 volts/cm; 0.54 $\mu$ sec/cm . . . . .	115
II-19	Pulse Shapes for Electron Bombardment of Dielectric; 5 volts/cm; 0.5 $\mu$ sec/cm . . . . .	115
II-20	Pulse Shapes for Ion Bombardment of Dielectric: A--Cell 1; B--Cell 2. . . . .	116
II-21	Pulse Shapes for Electron Bombardment of Dielectric: A--Cell 1; B--Cell 2. . . . .	116
II-22	Streamerlike Discharges on Dotriacontane: A, C, and E are Electron Bombardment; B, D, and F are Ion Bombardment; 0.5 volt/cm; 0.1 $\mu$ sec/cm . . . . .	117
II-23	Schematic Diagram of Coaxial Corona Generator . . . . .	118
II-24	Weight Loss of Mylar Due to Corona. . . . .	118
II-25	Weight Loss of Mylar as a Function of Corona Exposure; 14.5 kv on Cell in Air . . . . .	119
II-26	Weight Loss of 7- to 8-Mil Mylar Film . . . . .	119
II-27	Weight Loss Rate Constant of Mylar as a Function of Inverse Absolute Temperature; 14.5 kv on Cell in Air . . . . .	120
II-28	Corona Energy as a Function of Voltage at 24°C . . . . .	120
II-29	Corona Energy as a Function of Voltage at 70°C . . . . .	121
II-30	Corona Energy as a Function of Voltage at 98°C . . . . .	121
II-31	Corona Energy as a Function of Voltage at 120°C . . . . .	121
II-32	Weight Loss of "H" Film . . . . .	122
II-33	Weight Loss of "H" Film . . . . .	123
II-34	Weight Loss of "H" Film . . . . .	124
II-35	Weight Loss of "H" Film; 10 kv; 500-mm Vacuum . . . . .	124
II-36	Weight Loss of "H" Film at 10.3 kv . . . . .	125
II-37	Per Cent Weight Loss of "H" Film as a Function of Temperature and Pressure. . . . .	125

List of Figures (continued)

<u>Figure</u>			<u>Page</u>
II-38	Corona Damaged "H" Film Surface	110X. ....	126
II-39	Corona Damaged "H" Film Edge	110X. ....	127

# RESEARCH OF DIELECTRIC MATERIALS

## PHASE I. IONIZATION AND ELECTRON ATTACHMENT IN GASES

### A. NEGATIVE ION MASS SPECTROMETRY

H. L. Greenhaus

#### 1. Introduction

Attempts to utilize gases as insulants in electrical equipment has led to the investigation of gases with high electric strength. Electron attachment to a molecule can provide a high electric strength by formation of negative ions. These ions, being too large to produce collisional ionization, in effect remove electrons that would otherwise contribute to the exponential buildup of electrons.

A quantitative treatment of the buildup of current in a plane-parallel gas-filled gap, including the effect of attachment, has been given previously. (1) If  $\eta$  is defined as the attachment coefficient, i. e., the number of attachments of electrons to a molecule per electron per centimeter in the field direction, the quantity  $\eta/P$  is a function of  $E/P$  where  $P$  is the pressure of the gas and  $E$  the field strength. This quantity  $\eta/P$  is a function of the total cross section for attachment and the electron energy distribution. These cross sections for the negative ion formation processes are functions of the electron energy.

The work reported here concerns the elucidation of electron impact processes in electronegative perfluorocarbons by the use of negative and positive ion mass spectrometry, and the correlation of these processes with molecular structure. Mass spectrometry permits studying the ionic species formed, by electron-molecule interactions, as a function of electron energy. We are interested in the series of normal perfluorocarbons from  $CF_4$  through  $C_6F_{14}$  as representative of a series of compounds with high dielectric strength.

Critical potential measurements in an electron impact mass spectrometer generally involve measurement of ionization efficiency curves, which are representations of ion current intensity as a function of the energy of the ionizing electrons for the general reaction shown in Eq. (1),



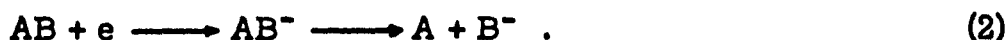
With a standard electron source, for positive ions, these curves are characterized by: (1) a threshold for ionization followed by an initially curved

---

Manuscript released February 1964 for publication as an ML Technical Documentary Report.

portion, (2) a linear portion extending over 10 to 20 ev, (3) a broad maximum between 50 and 100 ev, and (4) a monotonic decrease with increasing electron-accelerating potential. The initial curvature is primarily due to the inhomogeneity of the ionizing electron beam and makes accurate determination of the threshold appearance or ionization potential difficult. Broadness of the peak occurs because the two product electrons can carry away great amounts of kinetic energy in excess of that necessary for ionization.

Ion current curves, as functions of electron energy, for resonance capture or dissociative attachment processes, Eq. (2), for forming negative ions by electron impact generally start at low electron energies (below 10 ev) and go through a maximum, for each process, over a very narrow energy range.



In addition, the abundance of negative ions may be several orders of magnitude smaller than for positive ions. That is, the cross sections for electron attachment are small and have a narrow energy dependence.

Another mechanism exists for formation of negative ions by electron impact, which is an ion pair process illustrated by the general reaction



This process, for a given molecule, would occur at a higher electron energy than the dissociative attachment process. The observed appearance potential of the negative ion A. P. ( $B^-$ ) would be given, neglecting vibrational and excitation energy of product fragments, by

$$A. P. (B^-) = D(A-B) - E. A. (B) + I(A) + K. E. , \quad (4)$$

where  $D(A-B)$  is the dissociation energy of AB; E. A. is the electron affinity of B;  $I(A)$  the ionization potential of A; and K. E. the kinetic energy of the fragments.

Electron sources for electron impact guns are usually thermionic filaments operating at a high temperature that give a thermal electron distribution that is Maxwellian in character. This is the major cause of nonhomogeneity in electron beam energy. As previously mentioned, it causes curvature near threshold in ion efficiency curves.

For negative ions, if the cross section for the attachment process has a much narrower energy dependence than the electron distribution used to measure it, one gets an ion efficiency curve that reflects the distribution. A distribution narrow relative to the cross section will give the true energy dependence of the process.

## 2. Experimental Method

A mass spectrometer designed for negative and positive ions employing an effectively monoenergetic electron beam ( $\sim 0.1$  ev) has been constructed. A sensibly monoenergetic electron beam is necessary for negative ion studies because of the extremely narrow energy dependence of some of the electron attachment cross sections. It is also advantageous in determining appearance potentials for both negative and positive ions, minimizing the curvature near the threshold of ionization efficiency curves due to the energy distribution. The electron energy resolution obtainable with this spectrometer permits accurate determination of ionization and appearance potentials, bond dissociation energies and relative electron capture cross sections.

This resolution is obtained by employing a Retarding Potential Difference method<sup>(2)</sup> (RPD) in the electron gun of the ion source.

In the normal mode of operation for chemical analysis, the ionizing electrons may have an energy distribution with a half-peak width of about 1.5 ev owing, primarily, to the distribution of energies at the thermionic filament. The essential feature of the RPD method, which minimizes the effect of the distribution, is a "grid" interposed in the ionizing electron beam of the electron gun. An incremental retarding potential applied to this electrode gives a difference ion current due to the difference electron current. The difference ion current arises from electrons having a narrow ( $\sim 0.1$  ev) energy distribution.

The mass spectrometer described here was built by modification of an available instrument similar to the early version of the General Electric analytical spectrometer. Because of the more stringent requirements of the techniques described and their contemplated applications, most of the original circuitry has been replaced. Details of construction are given only where they are not typical of mass spectrometer construction or usage.

### 2.1 RPD Method

A standard Nier-type ion source<sup>(3)</sup> was modified to permit using a retarding potential difference technique similar to that previously described.<sup>(1)</sup> Figure I-1 is a simplified diagram of the source. Electrode (A) provides a positive potential to insure that the electron current is not space-charge limited at the filament. Electrodes (B) and (D) are maintained near filament potential. They serve to minimize penetration of fields into the volume between them. Electrode (C) is a retarding electrode that is kept negative with respect to the filament. It affects only those electrons in the electron energy distribution that have energies less than its potential, i.e., it provides an electron energy distribution entering the ionization chamber through (E) characterized by a sharp lower limit. A measured, variable electron accelerating potential is applied between the retarding electrode (C) and the ionization chamber (E). With this system, the only contact potential that could influence the energy of the electrons is that between the retarding electrode and ionization chamber.

These were gold plated to minimize this effect. Electrode (H) is an electron trap that collects the electron beam traversing the ionization chamber. It is maintained sufficiently positive to prevent secondary emission of electrons through the slit in (G). Electrode (F) is an ion repeller, which may be used to help focus ions into the analyzer tube.

If the variable accelerating potential is such that the electrons have sufficient energy to attach (negative ions) or ionize (positive ions), an ion current is recorded. Making the retarding potential on (C) more negative by a small increment,  $\Delta V$  ( $\sim 0.1$  ev), gives a difference ion current due to the difference electron current. The difference ion current arises from electrons having a narrow ( $\sim 0.1$  ev) distribution. Thus, an effectively monoenergetic electron beam is achieved whose width is determined primarily by  $\Delta V$ .

Stopping potential measurements on the electrons, within the slice determined by  $\Delta V$ , yield a difference ion current whose derivative is the electron distribution within this increment of the total distribution. The cross section for resonance attachment forming  $\text{SF}_6^-$  in sulfur hexafluoride has such a narrow energy dependence that its ionization efficiency curve reflects the electron distribution, (4) even with the narrow electron distribution used here. Figure I-2 shows the measured electron distribution for a 0.1 volt  $\Delta V$ . Over 75% of the electrons are within a centered 0.1 ev slice and over 92% within 0.2 ev. Figure I-3 shows the  $\text{SF}_6^-$  difference ion current, as a function of the electron accelerating voltage, reflecting the distribution. The electron curve determines the zero electron energy point on the voltage scale yielding an appearance potential of  $0.05 \pm 0.03$  ev in agreement with the literature value of 0.03 ev. The  $\text{SF}_6^-$  ion formation can thus be used as an electron energy calibration standard for negative ion attachment processes.

Conditions within the ion source may be different with the arrangement used for positive ions than for negative ions, owing to reversal of fields and higher electron energies. As a prelude to the use of the RPD method for positive ion appearance potential measurements, and because of the requirements of an energy calibration standard for positive ions, the formation of  $\text{A}^+$  from argon was studied. Figure I-4 shows the ionization efficiency curve for  $\text{A}^+$ ; the zero difference ion current point being assigned the value of the spectroscopic ionization potential. This figure shows the existence of two ionization processes separated by about 0.13 ev, which corresponds to the spectroscopic value of 0.18 ev for the separation of the  $2p_{3/2}$  and  $2p_{1/2}$  doublet ground states of  $\text{A}^+$ . Since the electron energy spread of the ionizing electron beam is about half the energy difference of the two states, the energy difference value obtained by extrapolation of the linear portions of the curve is considered in good agreement with the spectroscopic value. Similar results were obtained by Frost and McDowell(5) and Fox. (6)

The mass spectrometer is a 6-inch,  $60^\circ$  sectored magnetic field type. The glass envelope surrounding the ion source was modified to accommodate four

perpendicular four-lead stems to provide sufficient connections to a modified ion source. The original main electromagnet, supporting frame, and tube carriage assembly were retained. A Kepco Model 805 power supply (600 volts, 500 milliamperes) with a measured regulation of about 1 part in  $10^4$  furnished the current for the electromagnet. Several synchronous motors were incorporated into this supply to allow automatic magnetic scanning at various speeds.

To provide the high sensitivities required by the RPD method and for negative ion studies, a 10-stage electron multiplier detector was employed. This was constructed from a Dumont 6467 photomultiplier tube by removing the dynode structure from its envelope and base. A 12-pin stem, graded to Pyrex, was used in remounting the multiplier. The shield and first dynode were connected internally and the collector lead brought out the side to reduce electrical leakage. This unit is sealed into the Pyrex glass envelope at the exit of the analyzer tube after removing the usual ion collector plate. The multiplier could be baked out at  $300^\circ$  to  $425^\circ\text{C}$  for initial activation. A J. Fluke Model 408 d-c power supply furnished the interdynode potential through a resistance voltage divider. A multiplier gain of  $5 \times 10^5$  was obtained with an interdynode potential of 180 volts. This amplification factor was measured using singly ionized argon ions with about 2300 ev kinetic energy. After prolonged usage with organic vapors or after exposure to room air, some deterioration of the multiplier gain occurred. This was reversible on bakeout at  $425^\circ\text{C}$ . The output of the multiplier was fed into an Applied Physics Model 31 vibrating reed electrometer, which in turn feeds a Leeds and Northrup recorder. Two layers of soft iron plates,  $1/16$  inch thick, were placed around the magnet pole pieces to magnetically shield the multiplier and the ion source. In addition, several concentric insulated cylinders of annealed mu-metal were placed around the multiplier to provide further magnetic shielding.

The mass spectrometer and sample handling system are each evacuated with a Welch Duo-Seal 1405 fore pump and a mercury diffusion pump with a liquid nitrogen trap. With a bakeout of the spectrometer tube and multiplier, a pressure of  $1 \times 10^{-8}$  torr is readily achieved. A Veeco RG75 ionization gauge and RG31A power supply is used to measure the pressure. The gas handling system consists essentially of a sample manifold with several fixed calibrated leaks into the ionization source. McLeod gauges and a CEC Type 23-105 micromanometer are used to measure the pressure in the sample reservoir behind the leaks.

Because the large metal analyzer tube is electrically grounded by the supporting clamps and frame, and because an electron multiplier detector is used, different operating arrangements are required for positive and negative ion studies. The ion source is operated at 2300 volts above or below ground for positive and negative ions, respectively, to provide the ion accelerating voltage. Higher voltages occasionally result in flashover between the source leads. For positive ions, the first dynode is operated at about minus 1800 volts, with the anode at ground through the high-value input resistor of the

electrometer. The ions impacting on the multiplier, therefore, have about 4100 volts kinetic energy. For negative ions, both the source and first dynode are below ground, the latter 500 volts positive with respect to the former, thus establishing the ion energies at about this value. (The voltages given here are illustrative, others often being used.) Owing to the high-voltage operation of the ion source, all associated measuring circuitry had to be carefully insulated with Lucite and polystyrene for safety and to minimize electrical leakage.

## 2.2 Electron Gun

The electron gun assembly of the standard ion source used in the GE analytical spectrometer was modified for application of the RPD method. The lower shield plate and drawing out, focusing, beam centering, and ion beam defining slit plates remain unchanged. Modification of the top plate and attached electron gun enclosure was made as shown in the cross-sectional diagram in Figure I-5. Details of the electrical connections have been omitted. Figure I-6 is a sectional view, through the center of the electron gun slits, looking toward the top plate. All metal parts were made from Nichrome V. The sides of the box enclosure are attached to the top plate by spot-welded tabs. Electrodes (E) and (G) and the ends of the box are removable and are inserted into grooves in the side pieces. The spacings from the entrance of the ionization chamber, electrode (E), to the rear of the electron collector enclosure are unchanged. However, the front of the gun enclosure was extended to accommodate three additional slits behind the electron entrance slit, electrode (A). The latter, which had formed part of the removable filament assembly, was remade with clearance to the sides and bottom plate of the box. It is attached to the top side of the upper shield plate by sandwiching it between glass plate spacers and a mounting bracket illustrated in Figure I-6(B). These spacers are chosen so as to provide clearance between the rear of electrode (A) and the rear edge of the filament opening in the top plate. A filament lead stem is clamped to an adjustable saddle on electrode (A); 0.001- by 0.030-inch tungsten ribbon serving as the filament.

Electrodes (B), (C), (D), (E) and (G) are fabricated from 0.010-inch Nichrome V. A grooved quartz spacer on each side of the box supports electrodes (B), (C) and (D). A 0.020-inch quartz spacer insulates these electrodes from the top shield plate. It is a split spacer with one side notched to allow for electrical connections. A 0.030-inch quartz spacer insulates electrodes (A) to (D) from the bottom shield plate. When assembled, these spacers align the slits on center. The spacing between adjacent electrodes from electrodes (B) to (E) is 0.030 inch.

Very narrow slits have been used to prevent electrons with an appreciable transverse velocity component from entering the ionization chamber. The slits in electrodes (A), (B), and (D) are 0.020 inch wide and 0.160 inch long, while the slit in electrode (C) is 0.008 inch wide and 0.200 inch long. Electrodes (E) and (G) have slits 0.060 by 0.200 inch. All these are knife-edge slits cut



into the electrodes. Electrode (F) is a U-shaped ion repeller that tends to focus the ions on the first ion slit giving increased collection efficiency over that obtained with the original flat plate. Electrode (H) is a plate electron collector. All the electrodes in the electron gun are gold plated. They can be removed individually for cleaning or modification.

### 2.3 Associated Electronic Equipment

The mass spectrometer is designed to study both positive and negative ions by means of reversing switches on the magnet and voltage supplies.

The ion source filament supply is primarily two Gould Type CS1366 volt storage batteries isolated from ground. Filament current control is effected by suitable resistors on two low contact resistance Leeds and Northrup rotary switches. When the filament is not in use, the batteries are charged by a Triple-A Co. battery charger. Direct-current heating of the filament is employed in order to minimize the energy spread of the electron beam. Electron beam currents of a few microamperes saturation current, measured at the electron collector, are generally used for the RPD method to minimize the spread in the effective electron energy distribution due to space-charge effects. This mode of operation cannot use automatic emission regulation as this varies the filament temperature, and thus the electron energy distribution. However, for normal analytical work not using the RPD technique, an emission regulator may be switched into service, providing an electron accelerating voltage of 0 to 75 volts, electron collector of plus 75 volts with respect to the ionization chamber, and a regulated emission current with a-c heating of the filament.

The potentials for the various electrodes in the ion gun are provided by the 80-volt supply shown in Figure I-7. This supply is used in conjunction with the battery-operated filament and may be used either with or without the RPD method. Appropriate helipot in parallel allow the potentials to be controlled independently. When not using the RPD method, electrodes (A) to (D) are electrically connected to the ionization chamber. Included in the supply shown in Figure I-7 is a series of measuring resistors, which, when used in conjunction with a J. Fluke Model 801B differential voltmeter, operated as a precision potentiometer, accurately measures the total ionizing electron beam current and difference electron current. In addition, the supply furnished the ion repeller potential to the main control panel. An isolated 6.3-volt power also supplies the box galvanometer lamp.

Adjustment of the electron accelerating potential is effected by either a 10-turn, 10 k-ohm helipot (manually operated or motor driven by a General Radio Type 907-R dial drive) or by a General Radio Type 1454-A 10 k-ohm decade voltage divider, the latter allowing changes in 0.008-volt steps. This voltage can be made 2 volts negative to 78 volts positive with respect to the retarding electrode. The electron accelerating and other electron gun potentials can be read on a panel meter or measured by a Rubicon potentiometer

used in conjunction with a sensitive box-type galvanometer. Low contact resistance Daven rotary switches are used for interchanging these measuring circuits.

The ion accelerating and focusing voltages are obtained from a Hamner Model N-413 5-kv voltage supply with a line and load regulation of 0.005%. This feeds several voltage dividers in the main control panel that control the ion accelerating potential and the various focusing electrodes in the ion gun. The ion accelerating potential is determined by the potential of the ionization chamber with respect to the analyzer tube. Included in the main control panel are helipot and polarity reversing switches that adjust the ion repeller potentials.

### 3. Results and Discussion

Reese, Dibeler, and Mohler<sup>(7)</sup> in a paper on negative ions from polyatomic molecules surveyed the negative ions in perfluoropropane,  $C_3F_8$ , and perfluorobutane,  $C_4F_{10}$ , mass spectrometrically. Their results are shown in Tables I-1 and I-4. They attribute the formation of these ions to dissociative attachment processes. Percentage abundances given have been changed to values relative to the most abundant ion. Absence of an appreciable number or abundance of negative ions in perfluoropropane compared to perfluorobutane, in the work of Reese *et al.*, is not in accord with the relative magnitude of attachment coefficients from prebreakdown current measurements in these gases.\* To resolve this discrepancy, a study was made of the negative ions formed in these gases by electron impact in the mass spectrometer.

In Tables I-1 and I-4 are shown the ions found, in this work, in  $C_3F_8$  and  $C_4F_{10}$  along with their abundances relative to the most abundant ion. In perfluoropropane, we have found, in addition to the  $CF_3^-$  ion reported by Reese *et al.*,  $F^-$  and  $C_2F_5^-$ , the  $F^-$  being by far the most abundant. Repeated attempts were made to detect  $C_3F_7^-$  and the parent molecular ion  $C_3F_8^-$ , in this gas, but without success. The lifetimes of these ions may be much shorter than the transit time through the spectrometer tube, which required about  $10^{-6}$  second, thus precluding their detection. Several factors combine to hamper detection of negative ions. The narrow energy dependence of the cross sections, low abundances, and lack of accurate mass-scale calibration for negative ions require a systematic scanning procedure with stepwise adjustment of ion gun and spectrometer controls.

It is somewhat surprising that Reese *et al.*<sup>(7)</sup> had not found the  $F^-$  and  $C_2F_5^-$  ions in  $C_3F_8$ . However, these ions are formed by a dissociative attachment process, e.g., Eq. (5),




---

\*Phase I, Section B, this report.

where  $\Sigma e$  represents the kinetic energy of the fragments plus any energy of excitation. This is determined by the difference in energy between the electron affinity of B and the bond dissociation energy,  $D(A-B)$ . If it is assumed that the fragments are not formed in an excited state,  $\Sigma e$  is divided inversely as the fragment masses. It is well known that there is discrimination against ions formed with kinetic energy because of the alteration of focusing and ion collection properties in the mass spectrometer. A combination of low negative ion currents and the narrow energy dependence of the cross section for the attachment process may have caused these ions to be overlooked. The abundances of the ions in  $C_3F_8$  and  $C_4F_{10}$  found in this work are more in accord with the measurements of attachment coefficients from prebreakdown current measurements than are those of Reese *et al.*

The energy dependence of the cross sections for formation of  $F^-$ ,  $CF_3^-$  and  $C_2F_5^-$  in perfluoropropane,  $C_3F_8$ , have been determined utilizing the retarding potential difference method (RPD) and are shown in Figure I-8. The  $CF_3^-$  curve has been multiplied by a factor of three to separate it from  $C_2F_5^-$  in the figure. Included is the ion efficiency curve for  $SF_6^-$  from sulfur hexafluoride. This curve is normalized to the low energy  $F^-$  peak height. Sulfur hexafluoride, which is run admixed with the gas under investigation, calibrates the energy scale and gives the electron energy distribution.<sup>(4)</sup> The point of initial  $SF_6^-$  difference ion current is taken as the zero for the electron energy. The shape of the curve indicates an electron energy distribution with a half-peak width of 0.07 eV. An appearance potential of  $1.08 \pm 0.04$  eV is obtained for  $F^-$  formation in the dissociative attachment process corresponding to the lowest energy peak. The  $F^-$  curve is seen to consist of two broad peaks. The lowest energy one extends over about 2.2 eV and the high energy one about 3 eV. Appearance potentials for  $CF_3^-$  and  $C_2F_5^-$  are each 1.52 eV; the energy range for formation of these ions being approximately 2.3 and 2.0 eV, respectively.

Tailing exhibited by the ion curves in this figure, above 6 eV, has since been attributed to secondary emission or reflection of electrons into the ionization chamber of the mass spectrometer from the electron beam collector. Maintaining the collector a few volts positive with respect to the ionization chamber eliminated this effect without any appreciable spreading of the electron energy distribution in the beam.

A study was made of the appearance potentials of some positive ions in perfluoropropane using the retarding potential difference technique to minimize curvature near the ionization threshold due to the electron energy spread. These were  $CF_3^+$ ,  $C_2F_5^+$ , and  $C_3F_7^+$ ; the first two are two possible ions, which would be formed by breaking a C-C bond and the latter a single C-F bond. These are also the positive ions that would correspond to the observed negative ions in an ion pair process such as Eq. (3). If such a process occurred, both positive and negative ions with the same appearance potential would be observed. The positive ion provides a much more sensitive indicator for this process mass spectrometrically.

Argon was used, as an internal standard, to calibrate the energy scale for positive ions. Measurements were made on a mixture of  $C_3F_8$  and argon to eliminate the problem of variation of contact potentials within the ion source when gases are studied separately.

Ionization efficiency curves for these ions and  $A^+$  are shown in Figure I-9. No parent ion,  $C_3F_8^+$ , was found, in agreement with the published positive ion spectrum for this gas. (8) The lowest energy process is for formation of  $CF_3^+$  with an appearance potential of  $13.61 \pm 0.04$  ev. Dibeler, Reese, and Mohler (9) report a value of 14.4 ev using a mass spectrometer with a standard source. Appearance potentials for  $C_2F_5^+$  and  $C_3F_7^+$  were  $14.13 \pm 0.10$  and  $15.88 \pm 0.10$  ev, respectively. Appearance potentials for these ions have not been reported previously. Because the ion efficiency curves for the latter two ions approach the axis less abruptly than those for  $CF_3^+$  and  $A^+$  and the region of greatest interest (initial ion current) is the region of poorest signal-to-noise ratio in the ion detector, their appearance potentials carry a greater error than is usually the case when monoenergetic electrons are used. Even so, it is obvious the values are more accurate than those obtained by use of one of the many extrapolation procedures used in treating the data obtained without a sensibly monoenergetic electron beam. Factors militating against accurate results by the latter methods are the electron energy spread and the nonlinear dependence of the ion current on electron energy above the threshold potential. No positive ions were detected in the region of 6 to 13 ev, precluding ion pair processes in this energy region.

Experimentally determined appearance potentials, for the negative and some positive ions formed in  $C_3F_8$ , are given in Table I-2. The  $F^-$  ion is formed in the reaction



The appearance potential of  $F^-$  involves the bond dissociation energy,  $D(C_3F_7-F)$ , electron affinity of F, E.A. (F), and excess energy,  $\Sigma e$  (kinetic energy of fragments plus any energy of excitation). This can be represented as

$$A(F^-) = D(C_3F_7-F) - E.A. (F) + \Sigma e \quad (7)$$

The dissociation energy of the C-F bond is then

$$D(C_3F_7-F) = A(F^-) + E.A. (F) - \Sigma e \quad (8)$$

which gives a maximum value; the excess energy is unknown. Using a value of 3.63 for E.A. (F) (10) and the measured appearance potential of  $F^-$  as 1.08 ev

$$D(C_3F_7-F) \leq 108 \text{ kcal.} \quad (9)$$

No estimates could be made of  $\Sigma e$ .

For the positive ionization processes in  $C_3F_8$



the appearance potential of  $C_3F_7^+$  can be expressed as

$$A(C_3F_7^+) = D(C_3F_7-F) + I(C_3F_7) + \Sigma e \quad (11)$$

and, therefore, the ionization potential of the radical  $C_3F_7$  is given by

$$I(C_3F_7) = A(C_3F_7^+) - D(C_3F_7-F) - \Sigma e \quad (12)$$

By the use of the measured appearance potential of  $C_3F_7^+$  of 15.88 ev and the above calculated  $D(C_3F_7-F) \leq 108$  kcal, a value of 11.17 ev is obtained for the ionization potential of the  $C_3F_7$  radical. No measurements could be made of the possible excess energy of the system; however, the shapes of the ion efficiency curves for  $C_3F_7^+$  and  $C_2F_5^+$  indicate that these ions are formed with kinetic energy. (11) An indirect determination of the ionization potential of  $CF_3$  radical was made by Dibeler *et al.* (12) and directly by Farmer, Henderson, Lossing, and Marsden (13) giving the values 8.9 and 10.10 ev, respectively. Therefore,  $I(C_3F_7)$  appears to be greater than  $I(CF_3)$ . However, the above calculation disregards excess energy that would tend to make  $I(C_3F_7)$  smaller. The  $D(C_3F_7-F)$  used is a maximum and a lower value would have an opposite effect on  $I(C_3F_7)$ .

The C-C maximum bond dissociation energy for the reaction



is given by

$$D(C_2F_5-CF_3) = A(CF_3^+) - I(CF_3) - \Sigma e \quad (14)$$

Our appearance potential for this ion, 13.61 ev, and the ionization potential of  $CF_3$  radical of 10.10 ev given by Farmer, Henderson, Lossing, and Marsden (13) gives

$$D(C_2F_5-CF_3) \leq 80.7 \text{ kcal.} \quad (15)$$

Dibeler (12) calculated a maximum value of  $D(C_2F_5-CF_3)$  as 126 kcal using an indirectly calculated value for the ionization potential of  $CF_3$ . Using the directly measured value for  $I(CF_3)$  from Farmer *et al.*, Dibeler calculated  $D(C_2F_5-CF_3) = 98.9$  kcal. Our value of 80.7 kcal is the same as  $D(C_2H_5-CH_3)$  found in  $C_3H_8$  by electron impact. (14)

Using the appearance potential measurement  $A(C_2F_5^+)$  from  $C_3F_8$  with  $D(C_2F_5-CF_3)$  taken as 3.51 eV (80.7 kcal), an ionization potential of 10.62 eV is calculated for the  $C_2F_5$  radical. The same uncertainty applies to this measurement as to  $I(C_3F_7)$  discussed above. These results, without the knowledge of the excess energy of the system, indicate the ionization potentials of the radicals increase from  $CF_3$  to  $C_3F_7$ .

Bryant<sup>(15)</sup> developed a method of "group contributions" for estimating thermodynamic quantities for fluorocarbon compounds not yet investigated experimentally with the ultimate objective of evaluation of reactions associated with polymerization and polymer degradation in fluorocarbon systems. From his correlations, he estimates bond dissociation energies of 123 and 110 kcal for the primary and secondary C-F bonds, respectively, in  $C_3F_8$ . In view of Bryant's results, our value of  $D(C_3F_7-F) \leq 108$  kcal, calculated from the low-energy limit of the cross section for the dissociative attachment process for  $F^-$  formation, probably corresponds to the breaking of a secondary C-F bond. Not enough is known about the shape of the potential energy surfaces for the ground and electronically excited states of  $C_3F_8$  to interpret the shape of the cross section in terms of unique molecular processes. A linear extrapolation of the rising portion of the higher energy  $F^-$  peak in Figure I-8 gives an intercept with the abscissa at approximately 3 eV. A C-F bond dissociation energy based on this value yields a value of 152 kcal. It will be shown below that a C-F bond dissociation energy of 147 kcal is obtained in  $C_2F_6$ . It is speculated that the second higher energy peak in the cross section of  $C_3F_8$  may correspond to the breaking of a primary C-F bond. However, these values are approximately 1 eV greater than Bryant's estimate of the dissociation energy for a primary C-F bond.

Bryant also states that fluorination of a saturated hydrocarbon appears to have a negligible effect on the length of a C-C single bond. This is in accord with our findings, shown above, of exact agreement between the C-C bond dissociation energy for  $C_3F_8$  and the literature value<sup>(14)</sup> for  $C_3H_8$ .

Negative ion formation processes in perfluoroethane,  $C_2F_6$ , were investigated mass spectrometrically. This gas was obtained from E.I. duPont Co. with a purity of >99.9% as determined by vapor phase chromatography. The ions found in this gas and their relative abundance are given in Table I-3. The energy dependence of the cross sections for formation of  $F^-$  and  $CF_3^-$  in perfluoroethane have been determined using the RPD method and are shown in Figure I-10. The formation of each of these ions is attributed to a dissociative attachment process.

The electron energy scale was calibrated using the point of initial difference electron current determined from stopping potential measurements on the ionizing electron beam as described previously. The derivative of this curve shows an effective electron energy distribution with a half-peak width of 0.14 eV.

Appearance potentials for the  $F^-$  and  $CF_3^-$  ions in  $C_2F_6$  were determined as  $2.75 \pm 0.10$  and  $3.33 \pm 0.10$  ev, respectively. The half-peak widths for both the  $F^-$  and  $CF_3^-$  curves were 1.5 ev. The shapes of the negative ion efficiency curves were essentially superimposable when normalized at their maxima. Since the effective electron energy distribution half-peak width was smaller by approximately a factor of 10 than the half-peak width of the ion efficiency curves, Figure I-10 shows the energy dependence of the dissociative attachment cross sections for formation of  $F^-$  and  $CF_3^-$  in  $C_2F_6$ .

Experimentally determined appearance potentials for the negative ions formed in  $C_2F_6$  are given in Table I-3b. The dissociative attachment process for formation of  $F^-$  ion is



The dissociation energy of the C-F bond in the  $C_2F_6$  molecule can thus be represented by

$$D(C_2F_5-F) = A(F^-) + E.A. (F) - \Sigma e \quad (17)$$

Neglecting  $\Sigma e$  (kinetic energy of fragments and any excitation energy) and using the measured appearance potential of  $F^-$  as 2.75 ev and a value of 3.63 ev for E.A. (F),

$$D(C_2F_5-F) \leq 147 \text{ kcal.} \quad (18)$$

This value seems high in view of Bryant's<sup>(15)</sup> estimate of 123 kcal for the bond dissociation energy of the C-F bond in  $C_2F_6$ . However, our value is approximately 1 ev higher, and this is a reasonable value for  $\Sigma e$ .

Bibby and Carter<sup>(16)</sup> published a paper on ion formation processes in  $C_2F_6$  during the course of this work. They did not employ techniques for obtaining a monoenergetic electron beam. Using their results for the appearance potential of  $F^-$  as 2.2 ev, a C-F bond dissociation energy of 134 kcal can be calculated. This is almost one-half an electron volt higher than Bryant's estimate.

The appearance potential of  $CF_3^+$  in  $C_2F_6$  has been measured as 14.3<sup>(9)</sup> and 15.4<sup>(16)</sup> ev. Calculating a C-C bond dissociation energy from

$$D(CF_3-CF_3) = A(CF_3^+) - I(CF_3) \quad (19)$$

with  $I(CF_3) = 10.10$  ev, values of approximately 97 and 122 kcal are obtained. Patrick<sup>(17)</sup> estimates that the bond dissociation energy in  $C_2F_6$  is likely to be close to 83 kcal, similar to that in ethane. Using the value of 97 kcal for the C-C bond dissociation energy in  $C_2F_6$ , an electron affinity for the  $CF_3$  radical

is calculated from

$$E.A.(CF_3) = D(CF_3-CF_3) - A(CF_3^-) + \Sigma e \quad (20)$$

with our value of  $A(CF_3^-) = 3.33$  ev and neglecting  $\Sigma e$ . This gives 0.9 ev for  $E.A.(CF_3)$ . From the higher value of 122 kcal, an  $E.A.(CF_3)$  of 2.0 ev is calculated. The  $E.A.(CF_3)$  of 3.25 ev given by Bibby and Carter<sup>(16)</sup> reflects their high appearance potential for  $CF_3^+ = 15.4$  ev as compared to the value of Dibeler, Reese, and Mohler<sup>(9)</sup> of 14.3 ev, and their value of  $A(CF_3^-) = 2.8$  ev, which is lower than the  $A(CF_3^-) = 3.33$  ev obtained in this work.

Perfluorobutane,  $C_4F_{10}$ , was studied in the mass spectrometer at a pressure of approximately  $5 \times 10^{-6}$  torr. It was of particular interest to see if a careful survey of the negative ion spectrum would show the presence of a parent negative ion,  $C_4F_{10}^-$  not found in the work of Reese et al. Detection of this ion mass spectrometrically would help in understanding a pressure dependence for attachment in this gas found in prebreakdown current measurements.\* Owing to the low abundances of some of the negative ions in this gas, the RPD technique was not used. The negative ions found in the spectrum of  $C_4F_{10}$  are given in Table I-4, and a parent negative ion is indeed observed. Relative abundances are expressed as per cent of the  $F^-$  peak height. As can be seen in this table, the ion current curves as a function of electron energy, for  $CF_3^-$  and  $C_4F_9^-$  consist of at least two peaks with an abundance given for each. These double peaks were discernible with the electron energy distribution used (half-peak width 0.5 ev). The two peaks corresponding to ion formation processes at different electron energies for  $C_4F_9^-$  have previously been reported by Reese et al., but not for  $CF_3^-$ .

Appearance potentials for the negative ions found in  $C_4F_{10}$  were determined using an electron distribution with a half-peak width of 0.53 ev as determined by calibration with the  $SF_6^-$  ion. This was obtained by using the retarding electrode in the RPD source to retard the low-energy electrons. The appearance potentials are shown in Table I-4 along with the values determined by Reese et al. and show good agreement considering the uncertainty in their values is unknown.

The positive ion spectrum of perfluorobutane,  $C_4F_{10}$ , showed the presence of the parent molecular ion  $C_4F_{10}^+$ . Observation of this ion has not previously been reported and is not shown in the published positive ion spectrum for  $C_4F_{10}$ .<sup>(8)</sup>

The C-F bond dissociation in  $C_4F_{10}$  calculated from the approximate  $A(F^-) = 1.6$  ev is 120 kcal. Bryant's estimate is 123 kcal. No further comparisons are made because of the uncertainties in the measurements.

---

\*Phase I, Section B, this report.



A sample of perfluorohexane,  $C_6F_{14}$ , was obtained from the 3M Company. It was an impure sample characterized, from boiling point measurements, as 86% main product. Several negative ion peaks were observed in a preliminary survey of the spectrum of this sample. The presence of impurities made identification of all the ions of little value. Attention was concentrated on the ions found in the region between  $m/e$  202 and 333. The most abundant ion at  $m/e$  338 corresponds to  $C_6F_{14}^-$  and is identified as the parent molecular ion. A negative ion peak was found in the spectrum of this sample at  $m/e$  300 corresponding to  $C_6F_{12}^-$ . Since there is no positive ion of this  $m/e$  in the published spectrum of  $C_6F_{14}$  (8) the positive ion mass spectrum of our sample was investigated in the range  $m/e$  202 to 338. Peaks were detected in the positive ion spectrum at  $m/e$  values of 300 and 281 corresponding to  $C_6F_{12}^+$  and  $C_6F_{11}^+$ . These ions, not found in  $C_6F_{14}$  (8) are formed in cyclo- $C_6F_{12}$  (8) indicating the latter as one of the impurities present.

Attempts were made to purify the sample of  $C_6F_{14}$  by vapor phase chromatography, as described in Section B of this report. It was concluded from a VPC analysis that the final sample contained a mixture of isomers of  $C_6F_{14}$ . Several repeated mass spectrometric examinations were made of the positive ion spectrum of this purified sample. These spectra did not quantitatively correspond to the published relative abundances of the positive ions in  $n$ - $C_6F_{14}$ . However, differences would be expected between the spectra obtained, even for a known pure substance, in different mass spectrometers. As previously pointed out, the mass spectrometer differentiates against ions formed with kinetic energy. The collection efficiency for these ions in different instruments can vary considerably and would affect observed relative abundances. In addition, there are several discriminatory effects attributable to the electron multiplier collector. (18) Some of these are the energy, mass, electronic configuration, and charge of the incident particle. Thus mass spectrometric analysis of our isomeric mixture is not possible without the pure isomers to calibrate the relative abundances. For negative ion analysis, the discriminatory effects of the multiplier must be tolerated where detection sensitivity would not be adequate without its use.

The positive ion spectrum of the purified isomeric  $C_6F_{14}$  mixture showed less than 1% cyclo- $C_6F_{12}$  based on the  $m/e$  281 peak corresponding to cyclo- $C_6F_{11}^+$ . Also indicated was a peak at  $m/e$  85 that could not be accounted for on the basis of fragment ions from the perfluorocarbons. Beynon (19) attributes this peak to the  $SiF_3^+$  ion from  $SiF_4$  that is formed by the interaction of  $F_2$  or  $HF$  with the glass parts of the mass spectrometer. It is noted here that a negative ion was also detected in the mass spectrometer at this  $m/e$  and may be  $SiF_3^-$ . Vought (20) has reported the formation of  $SiCl_2^-$  and  $Cl^-$  in  $SiCl_4$ . No ion was detected that corresponds to  $SiF_2^-$ , and any  $F^-$  that may be formed from  $SiF_4$  would be masked by the  $F^-$  formed in the perfluorohexane.

The negative ions found in  $C_6F_{14}$  are given in Table I-5. They were obtained with an electron energy distribution with a half-peak width of 0.54 eV

in a similar manner described previously for perfluorobutane. Relative abundances given are determined from the relative maximum peak heights based on the  $C_6F_{14}^-$  ion. These are subject to the mass discrimination effects mentioned. Several of the ions gave multiple ion current peaks as a function of electron energy. Due to the energy spread in the electron distribution these peaks are not completely resolved. This overlapping of the multiple peaks alters, somewhat, the relative abundances determined. Where multiple peaks were discernible, a relative abundance and energy at which the peak maximum occurs are given. In the  $F^-$  ion curve in  $C_6F_{14}$ , a peak occurs at about 9 ev and extends over approximately 10 ev with a peak relative abundance of 11.5%. This may be due to an ion pair formation process such as Eq. (3). The presence of  $CF_3^-$  is noted in Table I-5. Its presence was detected using different experimental conditions and its abundance, which is very low, is not given.

Appearance potentials given were not determined using the RPD technique. They may, therefore, be in error by as much as the half-width of the electron energy distribution used. The retarding electrode of the RPD source was used to provide a narrow distribution, but the ionization efficiency curves obtained were from the total collected ion currents for each ion.

An appearance potential of  $1.5 \pm 0.3$  ev yields a C-F bond dissociation energy of 118 kcal, which compares with Bryant's estimate of 123 kcal.

Of especial importance in the negative ion spectra in perfluorohexane is the abundance of the parent molecular ion  $C_6F_{14}^-$ . The most abundant ion in all the lower molecular weight perfluoroalkanes investigated is  $F^-$ . In the perfluorohexane the  $C_6F_{14}^-$  ion is the most abundant ion being 1.6 times greater than  $F^-$ .

A preliminary study was made of the negative ion formation processes in perfluoropropene,  $C_3F_6$ , in the mass spectrometer. The only ion found was  $F^-$ . However, a great deal of difficulty was experienced in attempting to record the cross section as a function of electron energy for the  $F^-$  ion formation process. Reproducible results could not be obtained. Peculiar behavior of the ion currents was also noticed when this gas was studied in admixture with sulfur hexafluoride. It is possible that this gas is causing some unexplained changes in the filament electron emission. From our results on  $C_3F_6$ , it probably can be concluded that the only ion formed is  $F^-$  in low abundance relative to most of the perfluoroalkanes. There was insufficient time to explore this gas further.

It was desired to correlate the negative ion mass spectra obtained in this work with the results of the prebreakdown current measurements described in Section B of this report. To do so, it was felt that the spectrum for each gas should be obtained under as similar conditions as possible. Some of the gases in this work were studied under conditions of maximum resolution and sensitivity (e.g., using the RPD technique) to obtain accurate appearance

potentials and detailed cross sections for electron attachment and others, because of low ion abundances were not. Because of this, abundances of all the ions in all the gases were not relative to each other. Differences in the instrumental conditions used preclude comparison of ion abundances from the several gases.

Negative ion spectra were obtained for all the gases under as similar conditions as possible. As narrow an electron energy distribution was used as would give adequate sensitivity for detection of the low abundance ion. The procedure was to utilize the retarding electrode in the RPD source to prevent the low-energy electrons from entering the ionization chamber. Sulfur hexafluoride was used to determine the half-peak width of the electron distribution, which was 0.5 ev, and to calibrate the energy scale.  $\text{SF}_6$  was not admixed with each sample as it would contribute  $\text{F}^-$  ions to the spectra. (21) This procedure, therefore, introduces an uncertainty in the energy scale due to contact potential differences in the electron gun in each gas. The ionization efficiency curves, i. e., ion current curves as a function of electron energy were obtained by sweeping the electron accelerating voltage from -2 to 10 volts. This was accomplished by using the synchronous motor-driven helipot voltage divider described in the Experimental portion of this section. Ion currents were then recorded as a function of this increasing electron voltage.

The magnet current was adjusted for collection of each ion of interest. The ion accelerating voltage was maintained constant throughout the entire series of experiments, as was the interdynode potentials on the electron multiplier ion collector. Thus the kinetic energy of the ions impinging on the first dynode of the multiplier was constant, within the variation of the kinetic energy of formation of the ions. The latter probably represents less than 1/2% of the total kinetic energy of the impinging particle, and, so far as secondary emission of electrons at the collector is concerned, is a negligible variation.

The ion drawout and ion repeller potentials were held constant with respect to the ionization chamber. They were adjusted to provide optimum collection efficiency for all the ions studied. Differences in kinetic energy of formation of the various ions would require different ionization chamber extraction voltages for maximum ion collection. However, the ion repeller electrode and the ion drawout electrode exert a retarding and accelerating effect, respectively, on the electron energy distribution and would, in this case, vary the electron energy distribution and energy scale for each ion. The latter would be a much greater effect than the loss of ion collection efficiency.

All the other electrodes in the electron gun were held at fixed voltages. The other electrodes in the ion gun, i. e., the beam centering and ion focusing electrodes, were varied to maximize collection of each ion. These electrodes are sufficiently far removed from the ionization chamber to have little effect on the electrons.

The ion current curves thus obtained for  $\text{CF}_4$  through  $\text{C}_6\text{F}_{14}$  (with the exception of  $\text{C}_5\text{F}_{12}$ , which was not available) are shown in Figures I-11 through I-15. It should be noted that some of these curves are plotted on different ordinate scales. The negative ion efficiency curves shown in these figures have been smoothed to show the gross energy dependence of the cross sections. In all cases, the half-peak width of the electron energy distribution used was narrower than the half-peak widths of the ion current peaks observed. The occurrence of multiple peaks, most of which were incompletely resolved in this series of experiments, is not shown. However, some of these features are given in some of the other figures and tables in this section of the report.

The important features clearly illustrated by this series of curves is the predominance of the  $\text{F}^-$  ion in the series through  $\text{C}_4\text{F}_{10}$ , and the appearance at  $\text{C}_4\text{F}_{10}$  of the parent molecular ion. At  $\text{C}_6\text{F}_{14}$ , the abundance of the parent molecular ion exceeds that of the  $\text{F}^-$  ion. This is further emphasized in Figure I-16, which shows the  $\text{F}^-$  ion and the parent molecular ion where applicable, for each gas, as a function of electron energy.

Resonance electron capture leading to formation of parent negative ions are seldom observed in mass spectrometers. The Franck-Condon region of potential energy curves defines the attainable energy states of the ions. Electrons in this range that do not have sufficient energy to cause spontaneous decomposition will form a vibrationally excited ion. This may be stabilized by collision that is not very probable at low pressures of the mass spectrometer, and the ion tends to lose its electron. With complex ions where the excess energy can be distributed among several degrees of freedom, a comparatively stable ion may be detected as is probably the case with  $\text{SF}_6^-$  from sulfur hexafluoride.

No parent negative ions were observed in  $\text{CF}_4$ ,  $\text{C}_2\text{F}_6$ , and  $\text{C}_3\text{F}_8$ . The lifetimes of these ions may be much shorter than the transit time through the mass spectrometer (about  $1\ \mu\text{sec}$ ) precluding their detection. Molecular negative ions are found, however, in  $\text{C}_4\text{F}_{10}$  and  $\text{C}_6\text{F}_{14}$  and have been reported in  $\text{C}_7\text{F}_{16}$ .<sup>(7)</sup>

As mentioned above, to form a long-lived negative parent ion, in the absence of collisional stabilization, the kinetic energy of the electron must be redistributed rapidly between the vibrational states of the molecular ion before reverse dissociation into the molecule and electron takes place. Our results indicate that for perfluorocarbons below  $\text{C}_4\text{F}_{10}$  either not enough vibrational states are available for redistribution of the excess energy or the electronic transitions all result in dissociation of the molecular ion.

The features illustrated in Figures I-11 to I-15 will be discussed further in Section B of this report in relation to attachment coefficients determined from prebreakdown current measurements.

## REFERENCES

1. "Research and Development on Corona-Resistant Materials," ASD Technical Rept. 61-693, 71-81 (March 1962).
2. R.E. Fox, W.M. Hickam, D.J. Grove, and T. Kjeldaas, Jr., Rev. Sci. Instr., 26, 1101 (1955).
3. A.O. Nier, Rev. Sci. Instr., 18, 398 (1947).
4. W.M. Hickam and R.E. Fox, J. Chem. Phys., 25, 642 (1956).
5. D.C. Frost and C.A. McDowell, Proc. Roy. Soc., A232, 227 (1955).
6. R.E. Fox, J. Chem. Phys., 35, 1379 (1961).
7. R.M. Reese, V.H. Dibeler, and F.L. Mohler, J. Res. Nat. Bur. Stds., 57, 367 (1956).
8. Catalog of Mass Spectral Data, American Petroleum Inst., Research Project 44.
9. V.H. Dibeler, R.M. Reese, and F.L. Mohler, Phys. Rev., 87, 213 (1952).
10. D.C. Frost and C.A. McDowell, J. Chem. Phys., 29, 503 (1958).
11. H.D. Hagstrum and J.T. Tate, Phys. Rev., 59, 354 (1941).
12. V.H. Dibeler, R.M. Reese, and F.L. Mohler, J. Chem. Phys., 20, 761 (1952).
13. J.B. Farmer, I.H.S. Henderson, F.P. Lossing, and D.G.H. Marsden, J. Chem. Phys., 24, 348 (1956).
14. R.I. Reed, Ion Production by Electron Impact, Academic Press (1962), p. 37.
15. W.M.D. Bryant, J. Polymer Sci., 56, 277 (1962).
16. M.M. Bibby and G. Carter, Trans. Faraday Soc., 59, 2455 (1963).
17. C.R. Patrick, Advances in Fluorine Chemistry, Vol. 2, eds. M. Stacey, J.C. Tatlow, and A.G. Sharpe, Butterworth & Co., Washington (1961), p. 19.
18. M.G. Inghram and R.J. Hayden, A Handbook on Mass Spectroscopy, Nuclear Science Series Rept. No. 14, Natl. Acad. Sci.--Natl. Res. Council (1954).
19. J.H. Beynon, Mass Spectrometry and Its Applications to Organic Chemistry, Elsevier Publishing Co. (1960), p. 416.
20. R.H. Vought, Phys. Rev., 71, 93 (1947).
21. R.K. Curran, J. Chem. Phys., 34, 1069 (1961).

**BLANK PAGE**

TABLE I-1  
NEGATIVE IONS IN PERFLUOROPROPANE,  $C_3F_8$

	<u>m/e</u>	<u>Ion</u>	<u>% Relative Abundance</u>
Reese et al. (7)	69	$CF_3^-$	Very low
This work	19	$F^-$	100
			35.5*
	69	$CF_3^-$	3.9
	119	$C_2F_5^-$	6.3

\*Values for ion formation processes at different electron energies.

TABLE I-2  
MEASURED NEGATIVE AND POSITIVE ION APPEARANCE  
POTENTIALS IN  $C_3F_8$

<u>Ion</u>	<u>Appearance Potential (ev)</u>
$F^-$	$1.08 \pm 0.04$
$CF_3^-$	$1.52 \pm .06$
$C_2F_5^-$	$1.52 \pm .06$
$CF_3^+$	$13.61 \pm .04$
$C_2F_5^+$	$14.13 \pm .10$
$C_3F_7^+$	$15.88 \pm .10$

TABLE I-3a  
NEGATIVE IONS FROM C<sub>2</sub>F<sub>6</sub>

<u>m/e</u>	<u>Ion</u>	<u>% Relative Abundance</u>
19	F <sup>-</sup>	100
69	CF <sub>3</sub> <sup>-</sup>	15

TABLE I-3b  
NEGATIVE ION  
APPEARANCE POTENTIALS IN C<sub>2</sub>F<sub>6</sub>

<u>m/e</u>	<u>Ion</u>	<u>Appearance Potential (ev)</u>
19	F <sup>-</sup>	2.75 ± 0.05
69	CF <sub>3</sub> <sup>-</sup>	3.33 ± .05

TABLE I-4  
NEGATIVE IONS IN PERFLUOROBUTANE, C<sub>4</sub>F<sub>10</sub>

	<u>m/e</u>	<u>Ions</u>	<u>% Relative Abundance</u>	<u>Appearance Potential (ev)</u>
Reese et al. (7)	19	F <sup>-</sup>	100	1.2
	69	CF <sub>3</sub> <sup>-</sup>	0.9	3.3
	119	C <sub>2</sub> F <sub>5</sub> <sup>-</sup>	17.1	2.8
	169	C <sub>3</sub> F <sub>7</sub> <sup>-</sup>	5.7	2.8
	219	C <sub>4</sub> F <sub>9</sub> <sup>-</sup>	5.7	2.1
			5.7*	4.1
This work	19	F <sup>-</sup>	100	1.6 ± 0.3
	69	CF <sub>3</sub> <sup>-</sup>	1.0	4.0 ± .3
			1.2*	
	119	C <sub>2</sub> F <sub>5</sub> <sup>-</sup>	13.7	2.6 ± .3
	169	C <sub>3</sub> F <sub>7</sub> <sup>-</sup>	2.8	3.6 ± .3
	219	C <sub>4</sub> F <sub>9</sub> <sup>-</sup>	0.2	2.2 ± .3
			.2*	
	238	C <sub>4</sub> F <sub>10</sub> <sup>-</sup>	.8	0.32 ± .3

\*Peak values for ion formation processes at different electron energies.



TABLE I-5  
NEGATIVE IONS IN PERFLUOROHEXANE, C<sub>6</sub>F<sub>14</sub>

<u>m/e</u>	<u>Ion</u>	<u>% Relative Abundance</u>	<u>Appearance Potential (ev)</u>	<u>Potential at Peak (ev)</u>
19	F <sup>-</sup>	64.5	1.5 ± 0.3 9.0 ± .5*	4.8 ± 0.3
69	CF <sub>3</sub> <sup>-</sup>	Very low		
119	C <sub>2</sub> F <sub>5</sub> <sup>-</sup>	1.0	1.0 ± .3	2.6 ± .3
143	C <sub>4</sub> F <sub>5</sub> <sup>-</sup>	2.8	0.5 ± .3	2.4 ± .3
169	C <sub>3</sub> F <sub>7</sub> <sup>-</sup>	32.5	.6 ± .3	2.9 ± .3 <sup>†</sup>
200	C <sub>4</sub> F <sub>8</sub> <sup>-</sup>	1.0 0.6**	.6 ± .3	2.2 ± .3
219	C <sub>4</sub> F <sub>9</sub> <sup>-</sup>	12.3 15.0**	.6 ± .3	2.9 ± .3
250	C <sub>5</sub> F <sub>10</sub> <sup>-</sup>	10.0	.6 ± .3	2.6 ± .3
269	C <sub>5</sub> F <sub>11</sub> <sup>-</sup>	5.1	1.0 ± .3	2.9 ± .3 <sup>†</sup>
319	C <sub>6</sub> F <sub>13</sub> <sup>-</sup>	7.3 3.8** 0.4**	0.4 ± .3	2.2 ± .3 3.1 ± .3 4.4 ± .3
338	C <sub>6</sub> F <sub>14</sub> <sup>-</sup>	100 67.2** 4.1**	0 ± .3	2.2 ± .3 5.0 ± .3 4.3 ± .3

\*Possibly due to ion pair formation.

<sup>†</sup>Unresolved shoulder at approximately 4.5 ev.

\*\*Peak values for ion formation processes at different electron energies.

**BLANK PAGE**

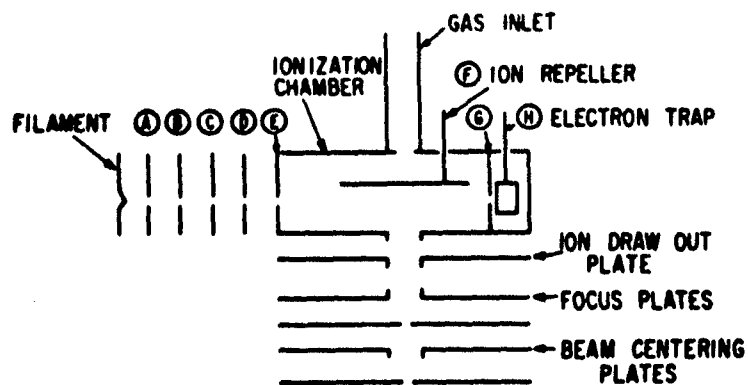


Figure I-1. Schematic Diagram of Mass Spectrometer Ion Source

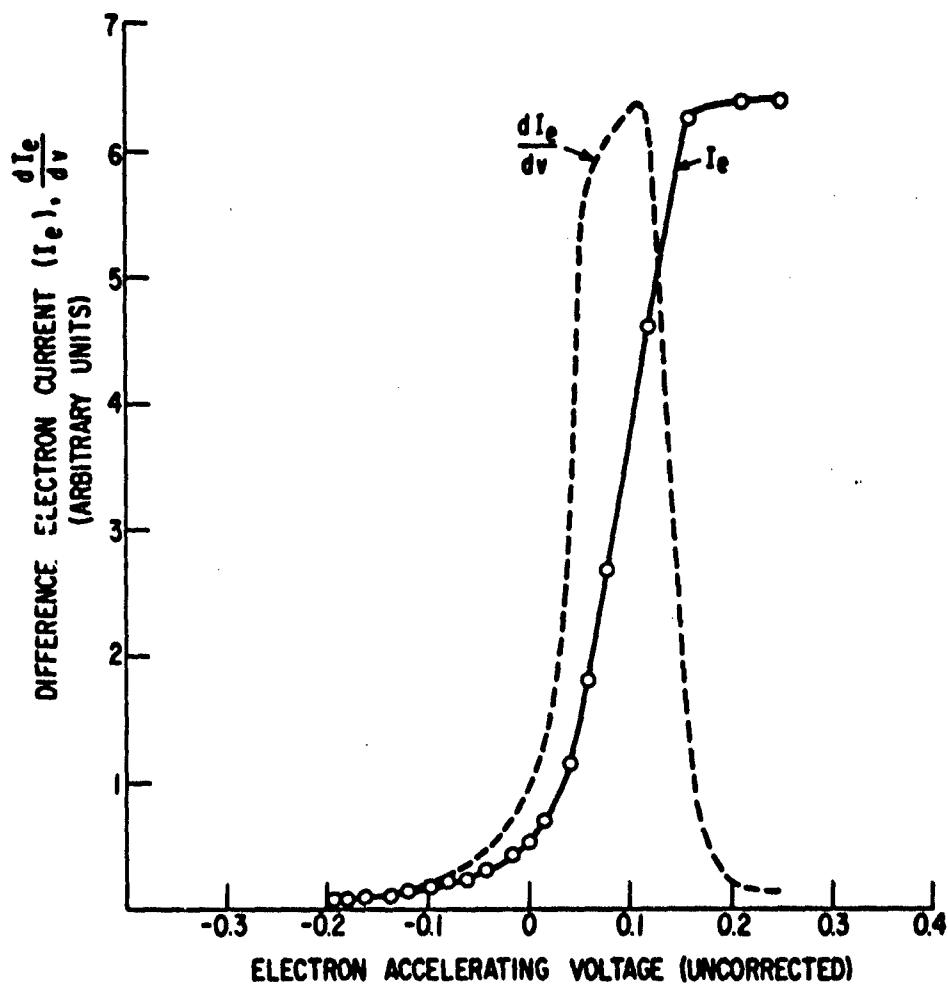


Figure I-2. Stopping Potential Curve for the Electron Current Associated with the RPD Method and Derived Electron Distribution

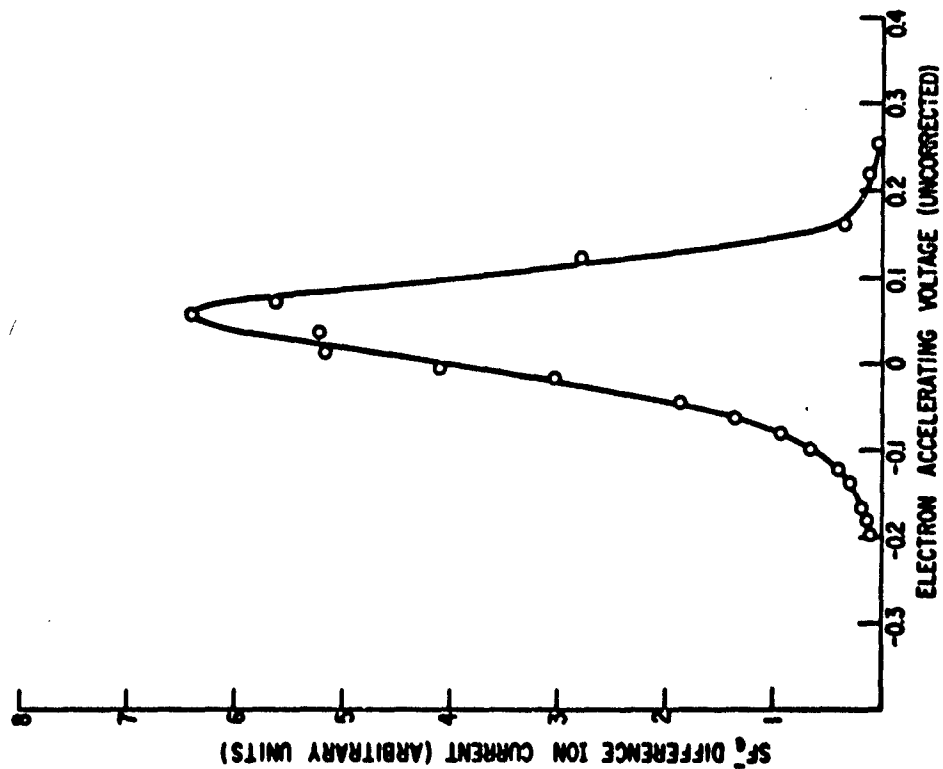


Figure I-3.  $\text{SF}_6^-$  Difference Ion Current as a Function of Electron Accelerating Voltage Employing RPD Method

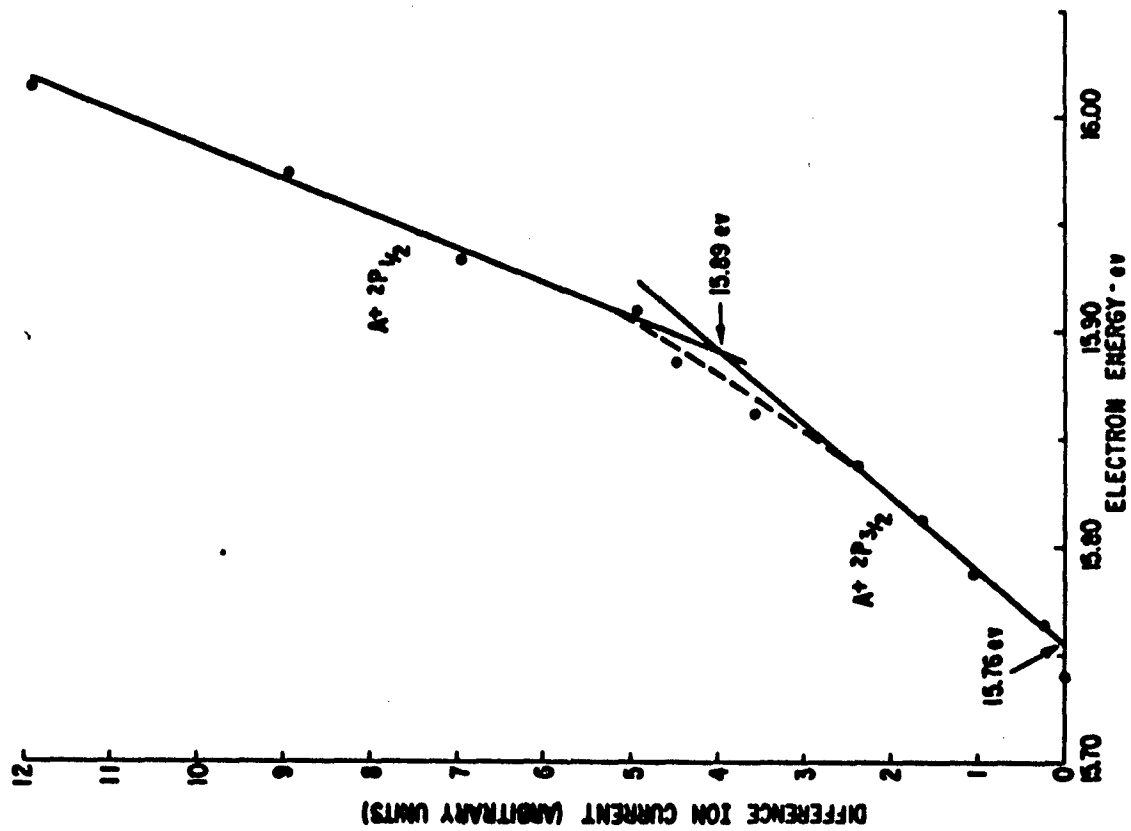


Figure I-4. Ionization Efficiency Curve for  $\text{A}^+$  in Argon

**BLANK PAGE**

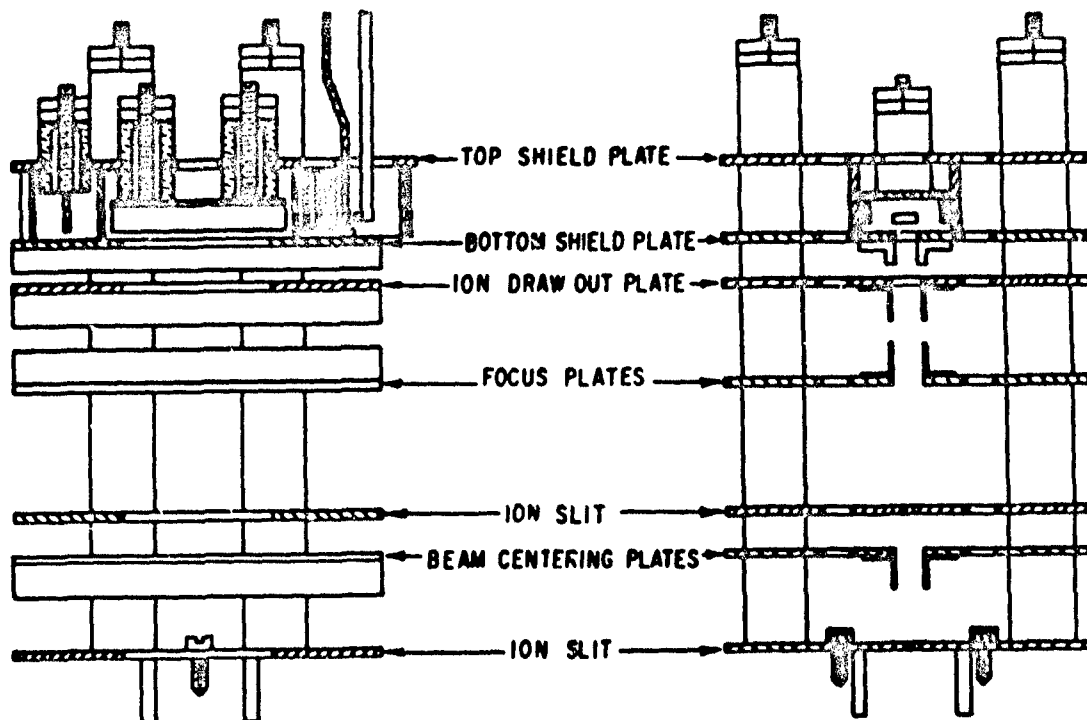


Figure I-5. Cross-Sectional Drawings of Mass Spectrometer Ion Source

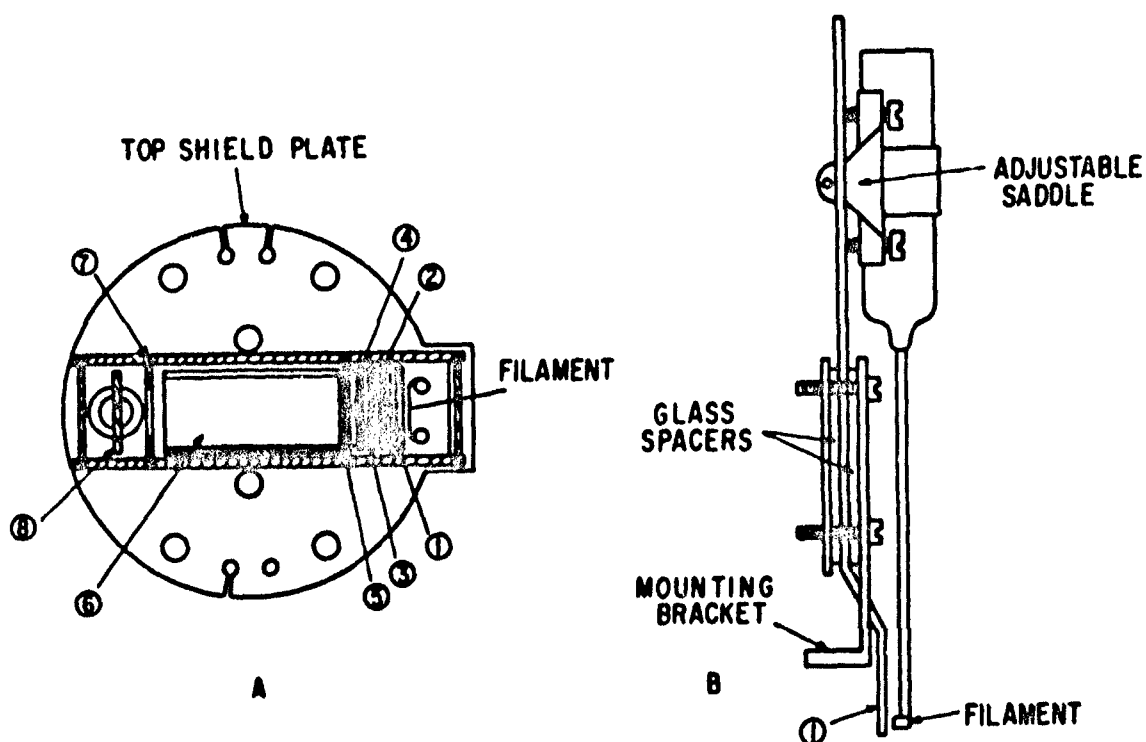


Figure I-6. A--Cross Section Through Electron Gun Slits Viewed Toward Top Plate; B--First Electron Gun Slit and Filament Assembly

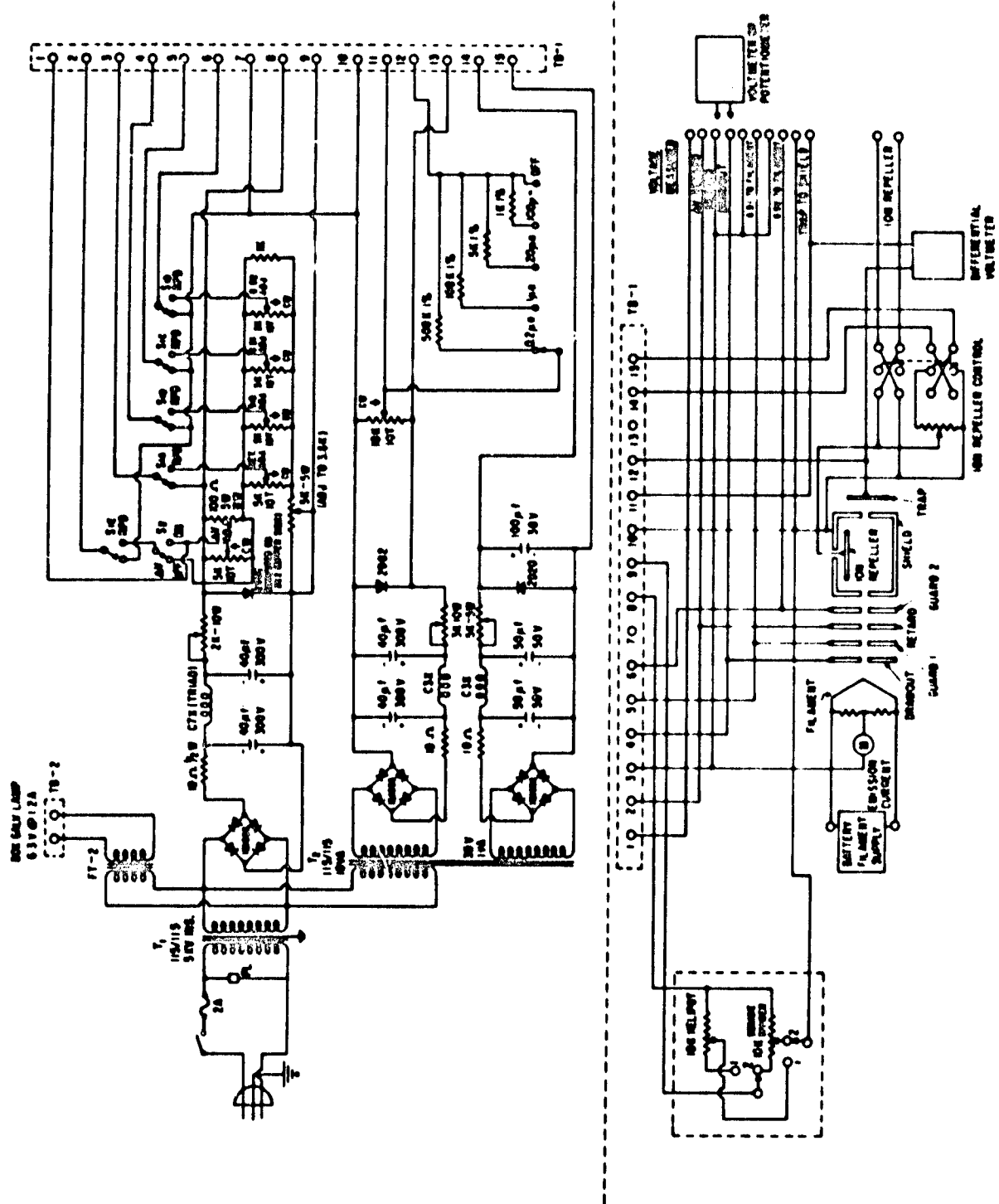


Figure I-7. Eighty-Volt RPD Supply for Electron Gun

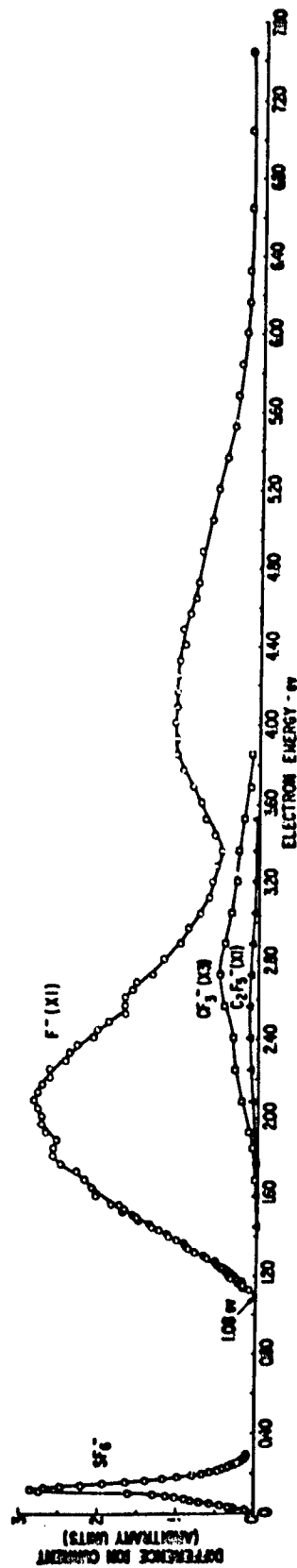


Figure I-8. Ionization Efficiency Curves for  $\text{SF}_6$ ,  $\text{F}^-$ ,  $\text{CF}_3^-$  and  $\text{C}_2\text{F}_5^-$  in Sulfur-Hexafluoride-  
 $\text{C}_3\text{F}_8$  Mixture



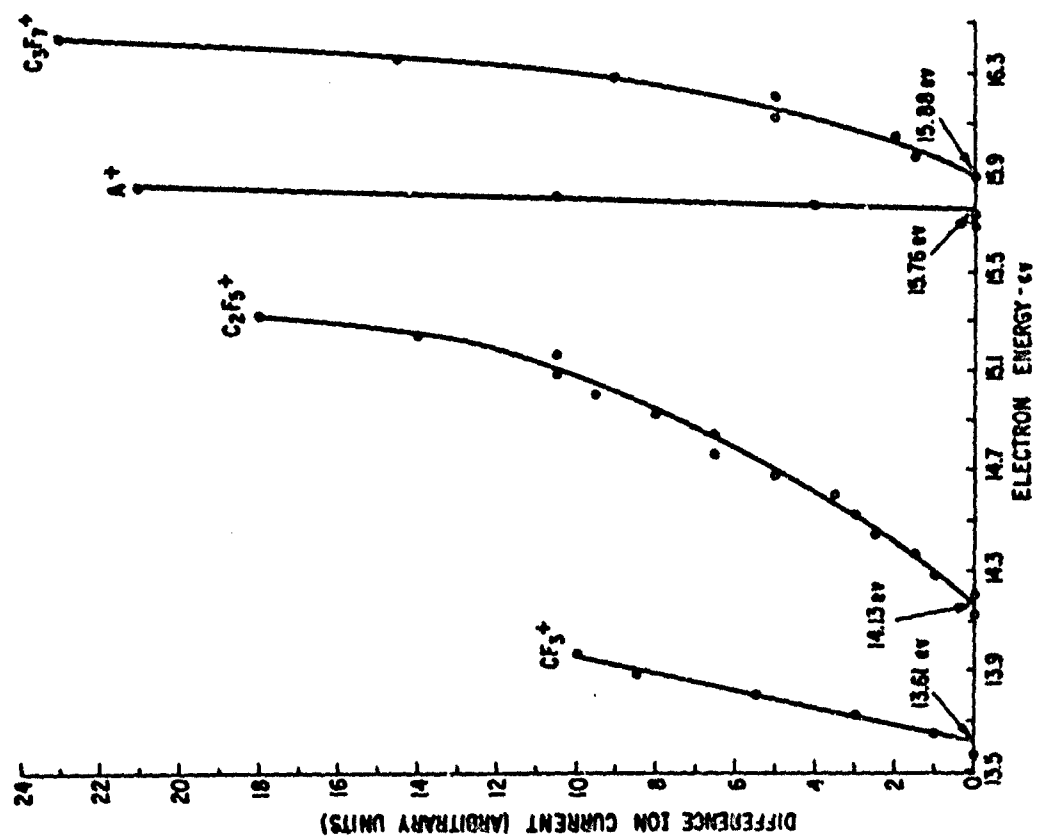


Figure I-9. Ionization Efficiency Curves for A<sup>+</sup> and CF<sub>3</sub><sup>+</sup>, C<sub>2</sub>F<sub>5</sub><sup>+</sup> and C<sub>3</sub>F<sub>7</sub><sup>+</sup> in an Argon-C<sub>3</sub>F<sub>8</sub> Mixture

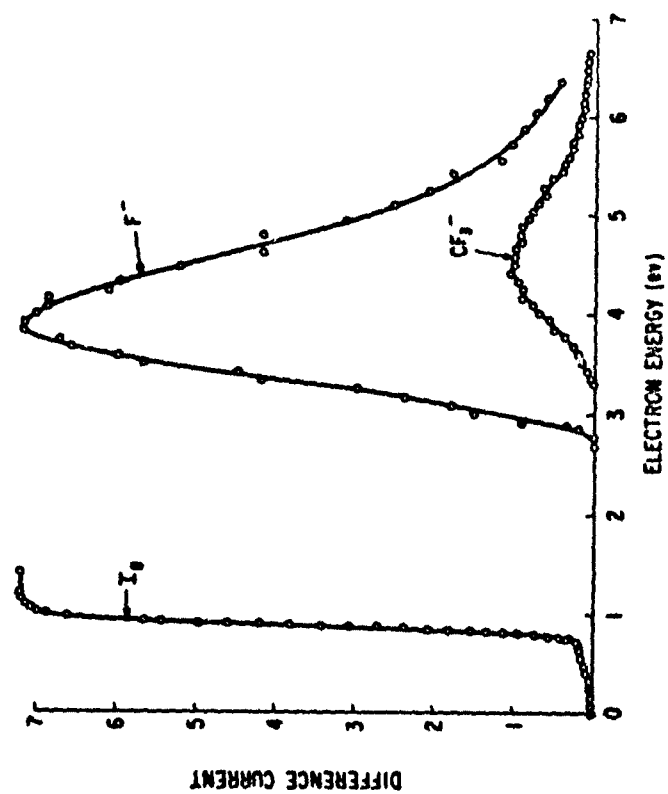


Figure I-10. Ionization Efficiency Curve for F<sup>-</sup> and CF<sub>3</sub><sup>-</sup> in Perfluoroethane, C<sub>2</sub>F<sub>6</sub>

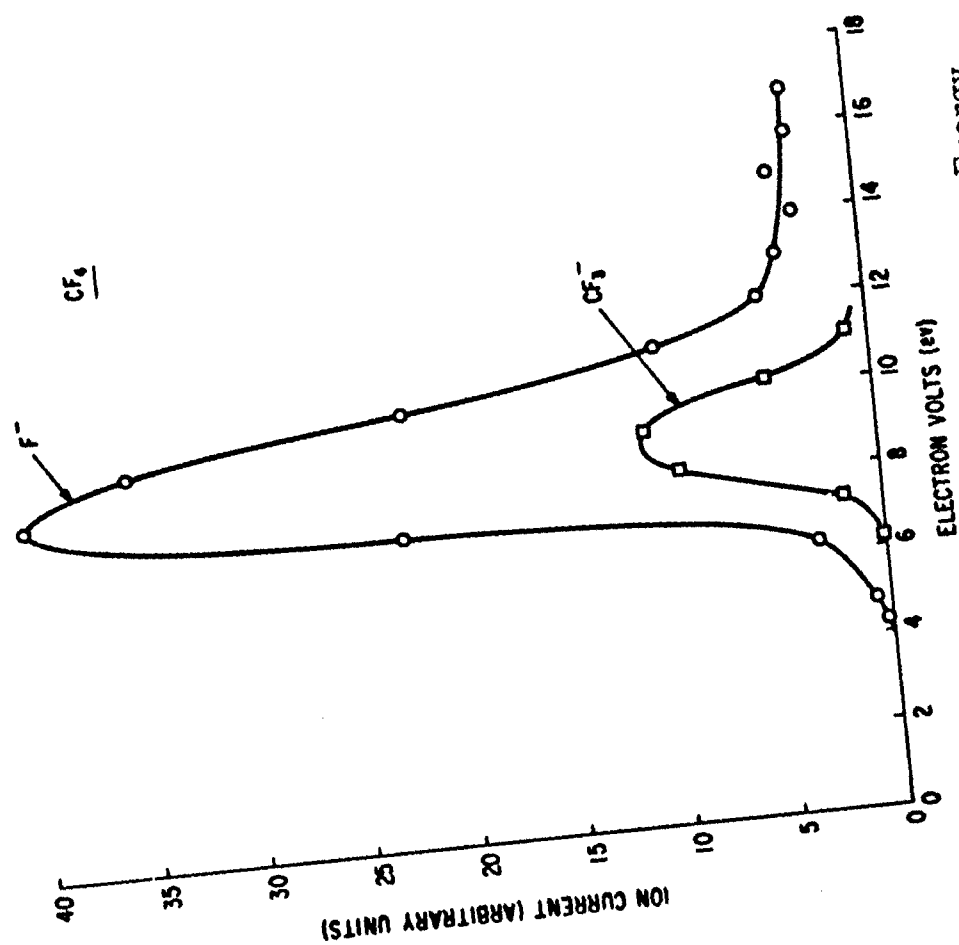


Figure I-11. Negative Ion Current-Electron Energy Curves for  $\text{CF}_4$

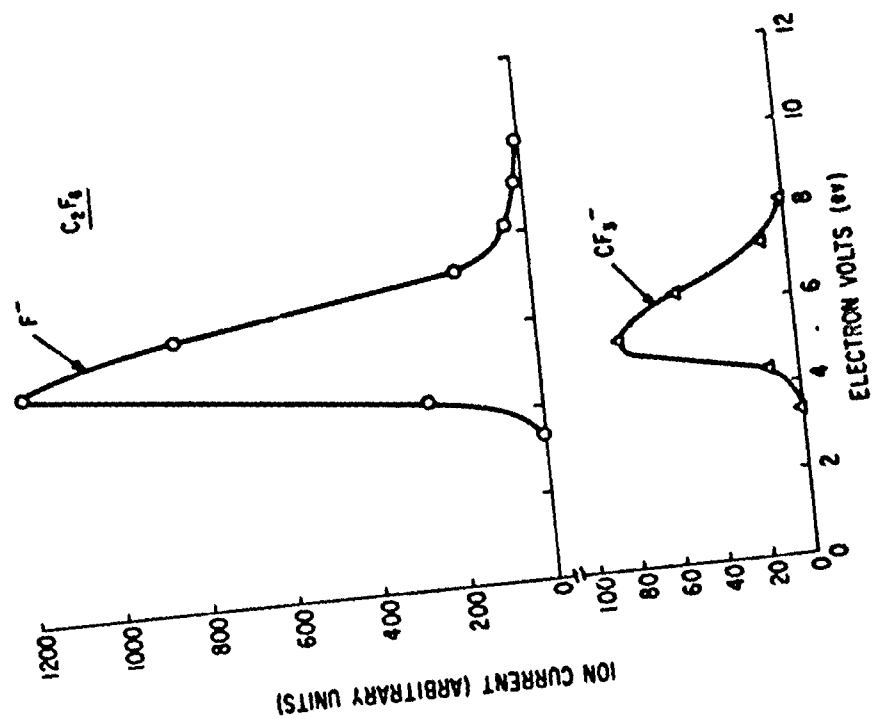


Figure I-12. Negative Ion Current-Electron Energy Curves for  $\text{C}_2\text{F}_6$

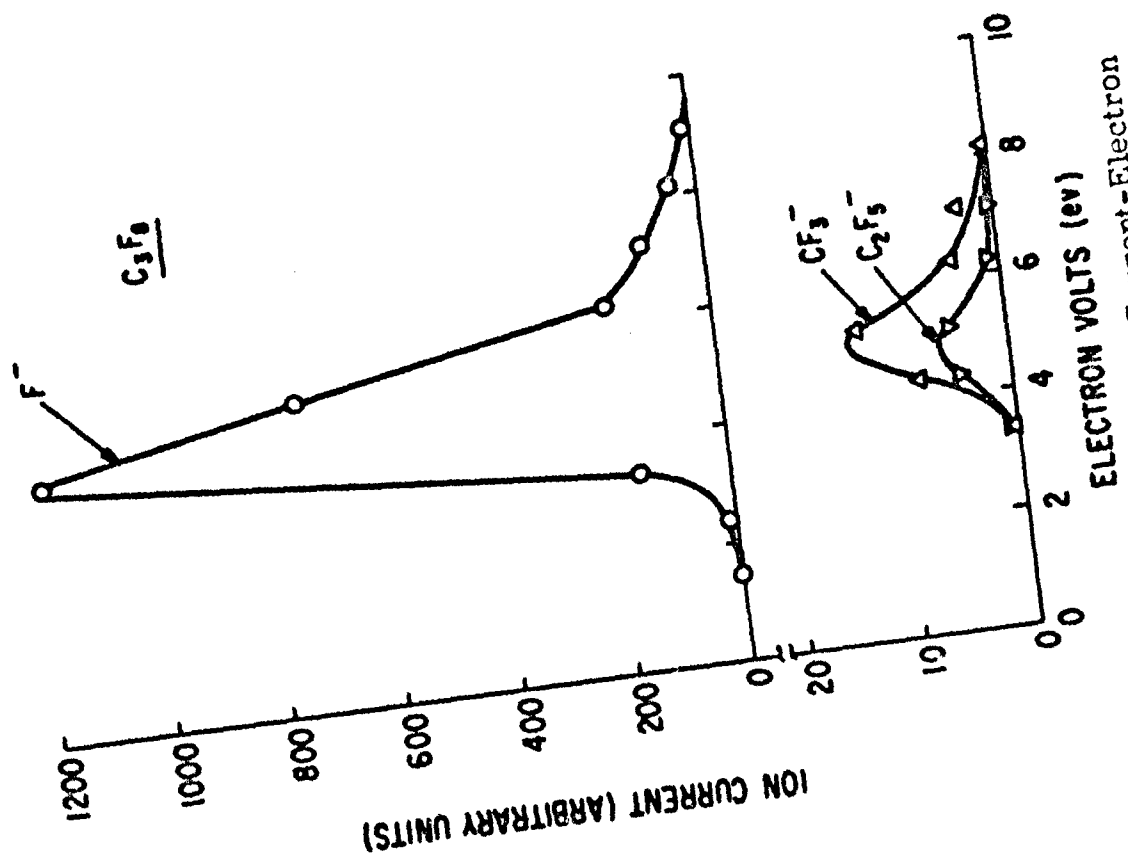


Figure I-13. Negative Ion Current-Electron Energy Curves for  $C_3F_8$ .

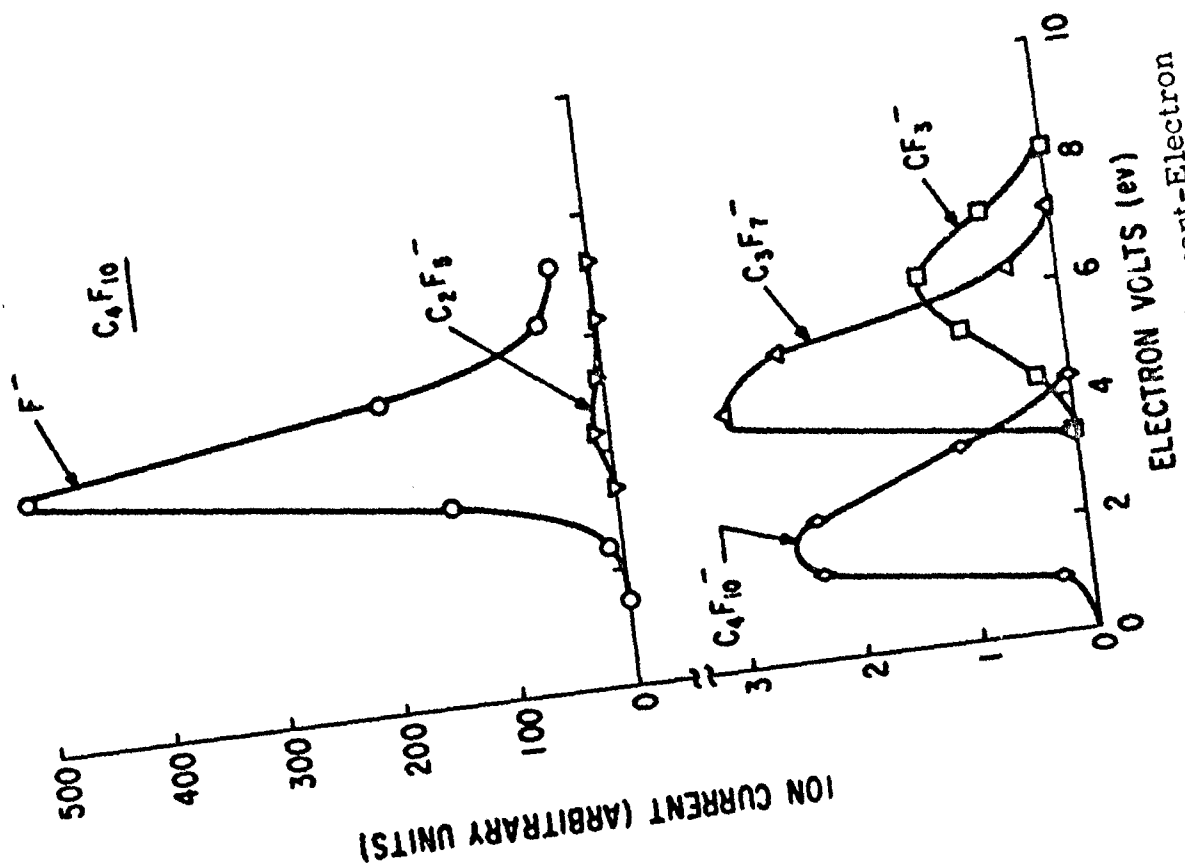


Figure I-14. Negative Ion Current-Electron Energy Curves for  $C_4F_{10}$ .

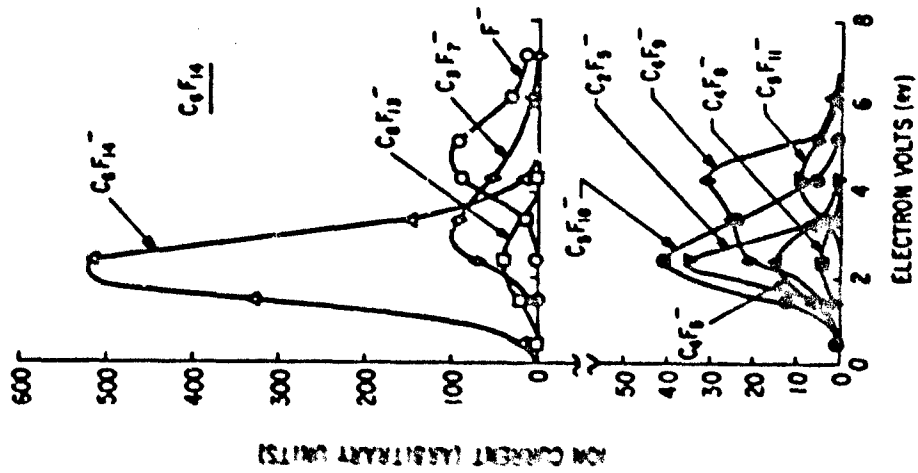


Figure I-15. Negative Ion Current-Electron Energy Curves for  $C_6F_{14}$

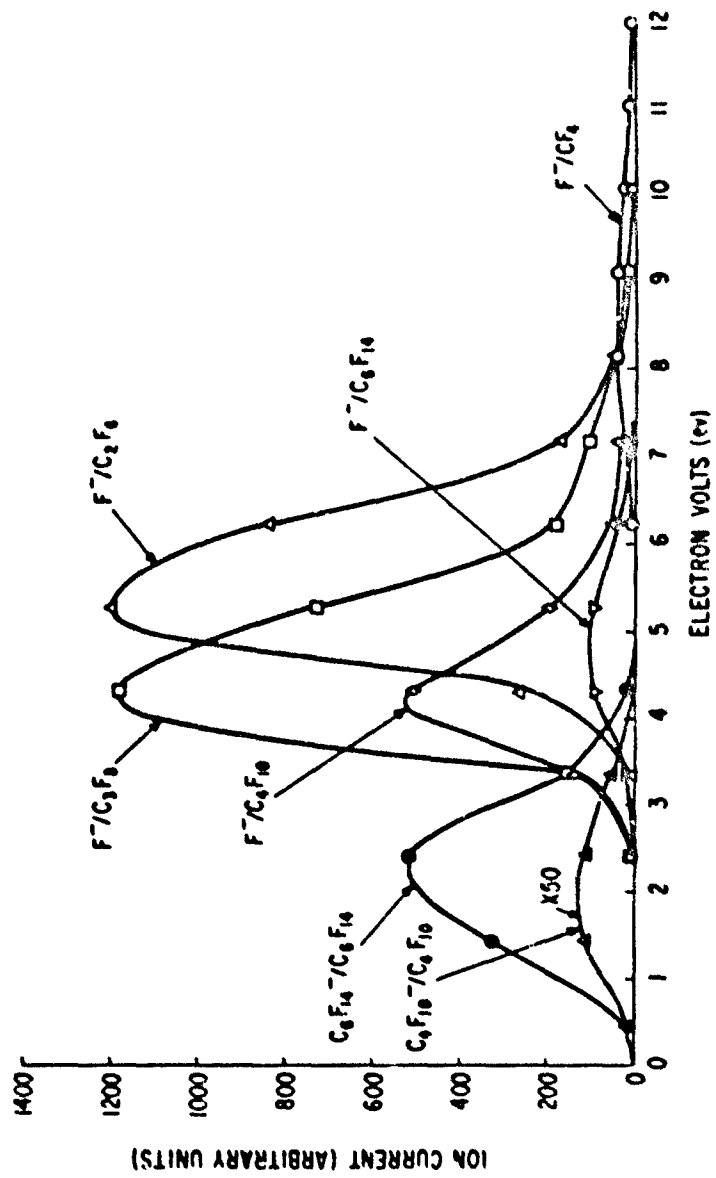


Figure I-16.  $F^-$  and Parent Molecule Ion Current-Electron Energy Curves for  $CF_4$  Through  $C_6F_{14}$

**BLANK PAGE**

## B. IONIZATION AND ATTACHMENT COEFFICIENTS

J. C. Devins and R. J. Wolff

### 1. Introduction

The work reported in this section is a continuation of that begun under U.S. Air Force Contract No. AF-33(616)-7485, the results of which are given in ASD Technical Report No. 61-693, Section C. <sup>(1)</sup> For a complete description of the experimental methods, results to date, and for references, the reader is referred to that report. For convenience, however, a summary of the methods will be given here.

A complete understanding of the relationship between sparking potentials of electronegative gases, and thus corona onset voltages, and their molecular structure requires a knowledge of the first Townsend ionization coefficients,  $\alpha$ , and the attachment coefficients,  $\eta$ , and their dependence on molecular structure of the gases. Here  $\alpha$  is the number of ionizing collisions and  $\eta$  is the number of collisions resulting in attachment that one electron makes in traveling 1 cm in the field direction.

In a plane-parallel gap of  $\delta$  cm width on which is superimposed a field,  $E$ , and in which the cathode is illuminated by ultraviolet light so as to supply a photoelectric current,  $i_0$ , the total current flowing in the gap to steady state may be shown to be

$$i = \frac{i_0 [\alpha/(\alpha-\eta)] \exp(\alpha-\eta) \delta - \eta/(\alpha-\eta)}{1 - \gamma \alpha/(\alpha-\eta) [\exp(\alpha-\eta) \delta - 1]} \quad (1)$$

Here  $\gamma$  is the second Townsend coefficient, the number of secondary electrons produced at the cathode for each primary electron produced in the gas by collisional ionization. In general,  $\alpha/P$  and  $\eta/P$  have been found to be functions of  $E/P$  for any one gas at pressure  $P$ . There is a range of values for  $\delta$ , for any one value of  $E/P$ , over which the second term in the denominator is small compared to unity, so that over this range a measurement of  $i$  vs  $\delta$  permits the evaluation of  $\alpha$  and  $\eta$  by curve-fitting to Eq. (1). This is the method used in the experiments described here.

The cell used in this work is shown in Figure I-17. The electrode system is mounted in a bell jar, A, containing a quartz window, B. The copper cathode, C, is at high potential and the current is measured in the anode circuit with a Keithley electrometer (Model 210) whose output is connected to a recorder. Ultraviolet irradiation from a GE BH-4 lamp (with outer jacket removed) passes to the cathode through the quartz window and through a screened nickel section, E, of the stainless steel anode 1 inch in diameter. Leveling screws F, together with an observation of color fringes from light shining through the gap, allow the 9-cm-diameter electrodes to be

made parallel. The cathode is movable through the sylphon bellows G with a vernier screw not shown in the figure. The gap is adjustable from 0 to 1 inch and is measured to within 0.0002 inch. A cylindrical nickel shield, H, surrounds the gap and this, as well as the aquadag coating on the inside of the bell jar, can be connected through Stupakoff seals, I, to any desired potential. In this work it has been found satisfactory to ground both of these shields. Voltage is supplied from a Hamner N-413, 0 to 5000-volt d.c. supply with line and load regulations of 0.0005% and noise and ripple of less than 50 mv. For voltages less than 170 volts, batteries are used. Voltages are measured using a precision voltage divider and a potentiometer, and are accurate to better than 1 volt.

Two vacuum systems are used: (1) an oil diffusion pump for the bell jar, and (2) a smaller mercury diffusion pump for the gas handling and filling system. The pressure in the cell is monitored with an Alphatron gauge, although the final pressure of the gas being investigated is measured by expanding from a calibrated volume at a higher pressure measured with an aneroid manometer.

The apparatus has been checked by measurements on Freon 12,  $\text{CF}_2\text{Cl}_2$ , which has also been measured by Harrison and Geballe.<sup>(2)</sup> In Figure I-18 we plot current against electrode separation. The full lines were calculated from Eq. (1) using values of  $\alpha$  and  $\eta$  given by G.H. The numbers on the curves refer to values of  $E/P$ , the ratio of field to pressure in  $\text{volt cm}^{-1} \text{ torr}^{-1}$ . The points are those obtained by us. Since  $i_0$  is an arbitrary constant, the curves were fitted at one point ( $\delta = 1.5 \text{ cm}$ ).

If the electrode separation,  $\delta$ , is increased sufficiently, the second term in the denominator of Eq. (1) is no longer negligible. When it approaches unity the denominator approaches zero and the current becomes very large. Thus

$$[\gamma\alpha/(\alpha-\eta)] [\exp(\alpha-\eta)\delta - 1] = 1 \quad (2)$$

defines the so-called Townsend threshold for breakdown of an electronegative gas. Since  $\alpha/P$  usually increases faster than does  $\eta/P$  with increasing  $E/P$ , it may be shown from Eq. (2) that usually there will exist a lower limiting value for  $E/P$  below which breakdown cannot occur, no matter what the gap; since below this value, attachment exceeds collisional ionization. It is noteworthy that the limiting value,  $(E/P)_{\text{lim}}$ , given by the condition

$$\alpha/P = \eta/P \quad (3)$$

is independent of  $\gamma$ , and is therefore determined only by the nature of the gas.

Earlier work with a large number of nonattaching gases has shown that the functional relationship between  $\alpha/P$  and  $E/P$  may be written to a

good approximation over the range of interest to breakdown as

$$\alpha/P = Ae^{-\frac{BP}{E}} \quad (4)$$

The constant, B, for these gases, was related to the Ramsauer cross section,  $\theta$ , by the equation

$$B = \rho \theta \epsilon_i^{3/2} \quad (5)$$

where  $\epsilon_i$  is the ionization potential for the molecule. The number  $\rho$  was found to be a constant for the hydrocarbons. Finally, it was observed that  $\theta$  could be written as the sum of cross sections for each pair of bonding electrons in the molecules, i.e.,

$$B/\epsilon_i^{3/2} = \sum_i n_i \theta_i \quad (6)$$

For the alkanes and cyclic hydrocarbons the cross section associated with the electrons of the carbon-carbon bonds was essentially zero, the total cross section being attributable to the carbon-hydrogen bonds. (3) A large contribution was found from the  $\pi$  electrons in the olefins, and in the conjugated systems of butadiene and benzene an even larger cross section was observed for each  $\pi$  electron. (4) The normal alkyl chlorides showed no electron attachment, and the value for B indicated about the same contributions from the carbon-hydrogen bonds, and in addition a contribution from the electrons associated with the chlorine atom. (5) Isopropylchloride, on the other hand, did show a small amount of attachment. Substituted propanes and butanes containing two or more chlorine atoms showed considerable attachment unless the chlorine atoms were separated by two or more carbon atoms in the molecule. As the chlorine atoms were moved closer together, attachment increased. (6)

During the last contract (1) measurements were begun on a series of fluorocarbons, but, owing to a lack of time, partial data were obtained on only two compounds: hexafluoroethane and octafluoropropane. In the work to be reported here, further measurements were made on both of these compounds, and in addition complete sets of data were obtained on tetrafluoromethane, decafluorobutane, tetradecafluorohexane, octafluorocyclobutane, hexafluoropropene, and t-butyl chloride.

With the exception of the last two of these and  $CF_4$ , all these gases are presently being used or considered for use as insulating gases in commercial equipment. They are promising because of their high thermal stability and low boiling points as well as their high electric strength resulting from electron attachment. A principal object of this work is to discover the relationship between molecular structure and the attachment and ionization coefficients in gases. Thus, in spite of its low electric strength,  $CF_4$  was



included as one of the five members available of the normal perfluoroalkane series. Hexafluoropropene was chosen to illustrate the effect of an olefinic double bond, and octafluorocyclobutane to examine the influence of cyclization. As we mentioned above branching in the alkyl chloride series resulted in some attachment, as was shown in isopropyl chloride; t-butyl chloride was investigated to determine whether such an effect could be observed in another branched compound.

## 2. Analysis of Data

In our earlier work, (1) a method was described for curve-fitting our data to Eq. (1) using straight line fits. While the results were satisfactory, the least squares fitting required approximately 4 hours to obtain a single value for  $\alpha$  and  $\eta$ . This was twice as long as required to make the measurements.

Since it was anticipated that a large amount of data would be taken, it was decided to program the IBM 704 computer to do the fitting. A large number of crosschecks have shown no significant differences in the results obtained by the computer and by hand calculations.

Let us consider Eq. (1) under conditions in which the second term in the denominator may be neglected compared with unity. For  $\alpha - \eta > 0$ , the first term will dominate for larger gaps and the current will increase very nearly exponentially with gap at a rate largely determined by the magnitude of  $\alpha - \eta$ . At small gaps, however, expansion of Eq. (1) shows that

$$i \doteq i_0 [1 + \alpha \delta]$$

neglecting terms in  $(\alpha - \eta) \delta$  higher than first order. Thus, to obtain reliable values for  $\alpha$ , considerable data must be taken with small gaps, while to obtain reliable values of  $\alpha - \eta$ , and, therefore,  $\eta$ , considerable data must also be taken for large gaps. Our procedure, therefore, is first to measure currents at gaps ranging from 0.254 to 2.79 cm in 0.254-cm intervals, and then at gaps ranging from 0.0381 to 0.254 cm in 0.0254-cm intervals.

From the large gap data we guess at a value for  $\alpha - \eta$ . Using the small gap data we do a least squares fit to the straight line expected from Eq. (1) for  $i$  vs  $\exp(\alpha - \eta) \delta$  with the IBM 704, obtaining the value  $\alpha i_0 / (\alpha - \eta)$  from the slope, and  $i_0$  from the intercept at  $\delta = 0$ . Equation (1) may now be rewritten as

$$\ln \left[ 1 - \frac{(\alpha - \eta)}{\alpha} + \frac{(\alpha - \eta)}{\alpha} \cdot \frac{1}{i_0} \right] = (\alpha - \eta) \delta + C \quad (7)$$

where  $C$  is a constant that will be zero if a perfect fit is obtained. Now, using both the large and small gap data and the values for  $(\alpha - \eta)/\alpha$  and  $i_0$

obtained above, a machine least squares fit is made to Eq. (7) and a new value for  $\alpha \cdot \eta$  is obtained from the slope. This new value for  $\alpha \cdot \eta$  is inserted again in Eq. (1) together with the small gap data and new values for  $(\alpha \cdot \eta)/\alpha$  and  $i_0$  are obtained. This iterative procedure is repeated until changes in  $\alpha$  are minimized. Usually less than 20 iterations are required, the total machine time being between 0.2 and 0.8 minute per run, depending upon the number of runs analyzed at one time.

### 3. Purity of Materials

The compounds investigated and their sources, methods of purification, and purities as used are listed in Table I-6. In all cases the figures for purity are based on vapor phase chromatography using a 12-foot by 1/4-inch diisodecyl phthalate column in a Perkin Elmer 154C instrument.

The  $C_6F_{14}$  as supplied\* showed a considerable number of impurity peaks. Purification was effected on a 12-foot by 3/8-inch preparation column containing diisodecyl phthalate in a FM Model 720 fractometer. While the impurity peaks originally present were removed by this technique, the major peak was somewhat broad, and in the light of the experience of Reed<sup>(7)</sup> it seems likely that separation of the isomers was not obtained. Assuming the method of preparation of our sample to be similar to that used by Reed, there may have been present as much as 30% perfluoro-2-methyl pentane as well as 5% to 10% perfluoro-3-methyl pentane and perfluoro-dimethyl butane isomers.

The *t*-butyl chloride as supplied also showed a number of impurity peaks. Attempts to purify this material with the vapor fractometer were unsuccessful owing to decomposition on the column. Distillation in a 20-plate column also failed to produce the necessary purification. The impurity was finally successfully removed by passing the material through a 2-foot silica gel column.

### 4. Ionization Potentials

To calculate composite cross sections from our values of  $B$ , the ionization potentials must be known. Values available in the literature, together with those we have chosen for calculation of cross sections, are shown in Table I-7. Since, as may be seen in the table, a number of discrepancies occur, we shall discuss here the justifications for our choices.

For the two perfluoroalkanes for which more than one value is available, rather large variations are found. By analogy with the corresponding hydrocarbons, a gradual decrease in ionization potential with increasing chain

---

\*We are grateful to the Minnesota Mining and Manufacturing Co. for supplying us with a sample of  $C_6F_{14}$  from its supply prepared for research purposes.

length is expected, and in earlier reports we have assumed a constant ratio for fluorocarbon to hydrocarbon values of 1.19. Bibby and Carter<sup>(9)</sup> find such a decrease in going from  $C_2F_6$  to  $C_3F_8$ , but their values seem inordinately high compared with those found by other workers. On the other hand, Dibeler et al.<sup>(10)</sup> report no variation with chain length. The single value reported in this work (for  $C_3F_8$ ) was measured using the RPD method and was, therefore, much less subject to the usual errors associated with the method of extrapolation (Section A). The ratio of ionization potentials for  $C_3F_8/C_3H_8$  using our value for  $C_3F_8$  and the value of 11.21 ev for  $C_3H_8$  given by Honig<sup>(12)</sup> is 1.21. The ratio for  $CF_4$ , using Honig's value<sup>(12)</sup> for  $CH_4$  of 13.04 ev is 1.19. It is, therefore, believed that the most reliable values can be obtained by using a constant ratio of 1.20, and it is on this basis that the values reported in column 3 of Table I-7, and used in this work, are given.

All of the ionization potentials for the perfluoroalkanes refer to the appearance of  $CF_3^+$ , which is by far the most predominant ion. Parent ions have been observed in  $C_4F_{10}$  and  $C_6F_{14}$ , although their appearance potentials have not been measured. In any event, their relative abundances are negligibly small. In  $C_4F_8$ , however,  $C_2F_4^+$  and  $C_3F_5^+$ , appear at the same potentials, about 3.5 ev below that for  $CF_3^+$ , and their abundances are four to five times that of  $CF_3^+$ . Thus, the ionization potential appearing in Table I-7 refers to the appearance of  $C_2F_4^+$  and  $C_3F_5^+$  ions.

Unfortunately, the only value for an olefinic perfluorocarbon that we have been able to find in the literature<sup>(13)</sup> is that for  $C_2F_4$ ,  $9.3 \pm 0.2$  ev, corresponding to the production of a parent ion. The value for parent ion production<sup>(14)</sup> in  $C_2H_4$  is 10.5 ev, while that<sup>(15)</sup> for  $C_3H_8$  is 9.7 ev. In the absence of a measured value, therefore, we have assumed in Table I-7 that the ionization potential for  $C_3F_8$  is  $(9.3 \times 9.7)/10.5$ , that is, 8.6 ev.

No parent positive ion is formed in  $t\text{-}C_4H_9Cl$ ; the lowest appearance potential is for the  $C_4H_9^+$  ion, which is also the most abundant.<sup>(11)</sup> We are interested in comparing this compound with  $n\text{-}C_4H_9Cl$  whose ionization potential has not been measured. This is estimated as being about 10.6 ev based on values<sup>(16)</sup> for  $CH_3Cl$  of 11.3,  $C_2H_5Cl$  of 10.9, and  $n\text{-}C_3H_7Cl$  of 10.7. In each case these values refer to the production of parent ions.

## 5. Results on Perfluoroalkanes

Values of  $(\alpha-\eta)/P$ ,  $\alpha/P$ , and  $\eta/P$  for a range of values of  $E/P$  are given in Tables I-8 through I-12 for the normal perfluoroalkanes. For all gases the range of  $E/P$  extends from such high values that  $\eta/P$  is negligibly small compared with  $\alpha/P$  to such low values that  $(\alpha-\eta)/P$  is zero or negative and multiplication of the photocurrent,  $i_0$ , becomes slight. It should be mentioned that in order to prevent space-charge distortion of the field, current densities never exceeded  $10^{-9}$  amp/cm<sup>2</sup>. Also, to avoid effects of secondary electron production, the multiplication of primary photocurrent was always kept below  $10^4$ .

Figure I-19 shows a plot of the logarithm of  $\alpha/P$  against the ratio  $P/E$ , and, except at the lowest values of  $E/P$  (high  $P/E$ ), these are linear as predicted by Eq. (4). Such a falloff in  $\alpha/P$  at low values of  $E/P$  has been observed for the hydrocarbons<sup>(17)</sup> and may be attributed to the contribution of energy losses by elastic scattering that has been neglected in obtaining the electron energy distribution from which Eq. (4) was derived. The straight lines drawn are least squares fit to the data, points to the right of the cutoff shown being omitted in the analysis.

Values of  $B$  obtained from the slopes of these lines are given in Table I-13, and show the expected regular increase with chain length. Values of  $B/\epsilon_i^{3/2}$  in Table I-13 are plotted against the number of carbon-fluorine bonds (or fluorine atoms) in Figure I-20. The corresponding values for the hydrocarbons are also plotted in Figure I-20, and it appears that the values of  $\rho_9$  [Eq. (5)] for these are slightly higher than for the fluorocarbons. The value for  $CF_4$  is somewhat below the line drawn.

Since over a large part of the range of  $E/P$  of interest,  $\eta/P$  is considerably smaller than  $\alpha/P$ , and since  $\eta/P$  is obtained from the difference between  $\alpha/P$  and  $(\alpha-\eta)/P$ , small fluctuations in either of the last two quantities will result in rather large fluctuations in  $\eta/P$ . These are evident on examining Tables I-8 through I-12. Accordingly, smoothed values of  $\eta/P$  are obtained by utilizing points picked from the best curves through  $(\alpha-\eta)/P$  vs  $E/P$  and  $\alpha/P$  vs  $P/E$ . The use of such a technique introduces the risk that rapid variations of  $\eta/P$  with  $E/P$  will be missed. However, the examination of a large amount of data has shown no evidence that the fluctuations observed are other than random and due to experimental error.

The dependence of  $(\alpha-\eta)/P$  on  $E/P$  is shown in Figure I-21 for the normal perfluoroalkanes. The curves are very nearly linear over most of the range of  $E/P$  with some curvature near zero. From these curves and those of Figure I-19, smoothed values for  $\eta/P$  are calculated and plotted against  $E/P$  in Figure I-22. Only the range of  $E/P$  for which  $\eta/P$  is a reasonable fraction of  $\alpha/P$  ( $> 10\%$ ) is used. It is clear from the figures that in these ranges attachment is rather small in  $CF_4$ , very large in  $C_6F_{14}$ , and does not differ greatly in  $C_2F_6$ ,  $C_3F_8$ , and  $C_4F_{10}$ . It appears, in fact, that the attachment coefficients lie generally in the order  $C_6F_{14} > C_3F_8 > C_2F_6 > C_4F_{10} > CF_4$ . Such a behavior was entirely unexpected and indicates that the attachment coefficient, unlike the ionization coefficient, is not simply related to molecular size. In all of these compounds,  $\eta/P$  decreases with increasing  $E/P$ .

## 6. Comparison with Breakdown Measurements

As discussed above [see Eq. (3)], the lower limiting  $E/P$  at which breakdown can occur is given by the crossover points of the curves in Figure I-21 with the line  $(\alpha-\eta)/P = 0$ . From these limiting values of  $E/P$  and the curves for  $\alpha/P$  vs  $P/E$  of Figure I-19, we may determine the values of

$\alpha/P = \eta/P$  at  $(E/P)_{\text{lim}}$ . Since over a fairly wide range of  $P \delta$  for breakdown in electronegative gases  $E/P$  lies near to  $(E/P)_{\text{lim}}$ , these values are particularly appropriate to breakdown. They are plotted against the number of C-F bonds for the perfluoroalkanes in Figure I-23. The curve possesses a maximum at  $\text{C}_3\text{F}_8$  and a minimum at  $\text{C}_4\text{F}_{10}$ .

Qualitative arguments may be made to show that if the sparking potential curves are linear with respect to  $P \delta$ , the slopes of these lines will be very nearly equal to  $(E/P)_{\text{lim}}$  (see Appendix). In Figure I-24 are plotted values for  $(E/P)_{\text{lim}}$  as a function of the number of carbon-fluorine bonds obtained from sparking potential measurements<sup>(13)</sup> and from Figure I-21. It is clear that while the agreement is satisfactory for the lower three members of the series, serious differences occur for  $\text{C}_4\text{F}_{10}$ . Agreement for  $\text{C}_6\text{F}_{14}$  is better though the value obtained from sparking potential measurements is still about 10% higher than that predicted from Figure I-21.

Since some doubt exists as to the validity of the assumption that the slopes of the  $V_S$ - $P \delta$  curves equal  $(E/P)_{\text{lim}}$ , we have attempted to calculate these curves directly using the condition that the denominator of Eq. (1) shall be zero, the Townsend criterion, and using our measured values for  $\alpha$  and  $\eta$ . The coefficient  $\gamma$  with its dependence on  $E/P$  is, of course, unknown, and it was necessary to fit to the experimental sparking potential curves at one point, and to assume that  $\gamma$  does not change with field. The latter assumption is not unreasonable for our purpose, provided that  $\gamma$  does not change by orders of magnitude with  $E/P$ , since it appears as a pre-exponential factor. With non-attaching gases this assumption has been found to be entirely adequate. A comparison between the calculated and measured sparking potential curves is shown in Figure I-25. While the agreement is entirely satisfactory for  $\text{CF}_4$  and  $\text{C}_2\text{F}_6$ , small differences are in evidence for  $\text{C}_3\text{F}_8$  and  $\text{C}_6\text{F}_{14}$ , and these are very significant for  $\text{C}_4\text{F}_{10}$ . It is noteworthy that the values of  $\gamma$  required for a fit range from  $10^{-6}$  to  $10^{-11}$  for the first three members, while for  $\text{C}_4\text{F}_{10}$  it is  $10^{-30}$ . The higher values are consistent with those which have been measured in nonattaching polyatomic gases, but it is difficult to imagine how values as low as  $10^{-30}$  could be physically meaningful.

The disagreement between measured sparking potentials and those predicted from the Townsend criterion using our measured values of  $\alpha$  and  $\eta$  for  $\text{C}_4\text{F}_{10}$  and to a lesser extent for  $\text{C}_3\text{F}_8$  and  $\text{C}_6\text{F}_{14}$  are particularly interesting. One possibility is that  $\gamma$  changes rapidly (by many orders of magnitude) with field, although as has already been mentioned the very low values for  $\gamma$  required to fit the data are difficult to explain. While it is easily understood that  $\gamma$  may decrease with increasing molecular complexity, owing to more complete absorption of light produced during avalanching, with a consequent reduction in photoelectrons produced at the cathode, the positive ions would still be expected to lead to reasonably efficient secondary electron production at the cathode.

Another possible explanation for the discrepancies in sparking potentials for the larger molecules involves the assumption that  $\eta/P$  is independent of pressure. To obtain the best accuracy in evaluating  $\alpha$  and  $\eta$  in our experiments we have chosen an optimum pressure for each value of  $E/P$ . Examination of Tables I-8 through I-12 will show that for this reason a check on the possible dependence of  $\eta/P$  on pressure has not been made. It is to be expected, at least for the smaller molecules, that attachment to form parent negative ions will be unlikely in our system, since the kinetic energy of the electron must be removed from the negative ion in a very short time or the electron will again fly off. Dissociative attachment, involving the dissociation of the molecule to form a negative ion and neutral fragment, seems more likely since some of the excess energy can be absorbed as kinetic energy of the fragments.

Assuming, however, that in forming a parent negative ion with a larger molecule the kinetic energy of the electron can be converted to molecular vibrational energy, the lifetime of this molecule-ion will be greatly increased. As a consequence, a collision of the excited negative ion with a third body, with a resultant sharing of energy and stabilization, becomes more likely with the larger molecules and at higher pressures. Since our sparking potential measurements were made at higher pressure (300 to 500 torr) than our measurements of  $\eta$  (1 to 10 torr), values for  $\eta$  should be higher in the former case if this effect is of importance. This would lead to higher values of sparking potentials and  $(E/P)_{lim}$  than predicted using the low-pressure values of  $\eta$ . Metastable positive ions, having a lifetime of ca. 1  $\mu$ sec, have been observed<sup>(19)</sup> in a number of hydrocarbons including  $C_4H_{10}$ , with a mass spectrometer. Recently, evidence for such effects in  $SF_6^+$  has also been obtained.<sup>(20)</sup> A dependence of  $\eta/P$  on pressure has also been recently observed in oxygen<sup>(21)</sup> and has been interpreted in a manner similar to that discussed here.

## 7. Dependence on Pressure

To test this hypothesis measurements of attachment and ionization coefficients were made on  $C_4F_{10}$  over a range of pressures at constant  $E/P$ . The range of pressures over which we may work at a given value of  $E/P$  is severely restricted. At higher pressures the voltages required become excessive and noise, owing presumably to leakage currents, limits our precision. At lower pressures multiplication is drastically reduced so that, again, the results become inaccurate. The measurements reported here cover very nearly the maximum range we can use without modification of our apparatus.

Table I-14 and Figures I-26 and I-27 show the dependence of  $\alpha/P$ ,  $(\alpha-\eta)/P$  and  $\eta/P$  on pressure for two values of  $E/P$ . It is clear that  $(\alpha-\eta)/P$  does, in fact, decrease with increasing pressure, and that this decrease is a result of an increase in  $\eta/P$ ,  $\alpha/P$  remaining essentially constant. The range of pressures over which the change occurs is similar for the two values of  $E/P$ , though the

magnitude of the change is different. Measurements were also made for a value of  $E/P$  of 110 volts  $\text{cm}^{-1}$  torr $^{-1}$ , but, owing to the low value of  $(\alpha-\eta)/P$ , scatter was high. Consequently, the results are not included here, although they appeared to show a similar falloff in  $(\alpha-\eta)/P$  with increasing pressure.

Since  $(\alpha-\eta)/P$  passes through zero at a pressure of 30 torr and  $E/P$  of 125 volts  $\text{cm}^{-1}$  torr $^{-1}$  and appears to be approaching a positive value at high pressures for  $E/P$  of 150 volts  $\text{cm}^{-1}$  torr $^{-1}$ ; it may be concluded that the limiting value of  $E/P$  at high pressures lies between these values. This is consistent with our sparking potential measurements, made at high pressures that give a value for the limiting  $E/P$  of 140 volts  $\text{cm}^{-1}$  torr $^{-1}$ .

Attempts to measure a pressure effect with  $\text{C}_6\text{F}_{14}$  were inconclusive although it may be concluded that if such an effect exists it is considerably smaller than with  $\text{C}_4\text{F}_8$ . Similar measurements are planned for  $\text{C}_3\text{F}_8$  but have, as yet, not been made.

#### 8. Octafluorocyclobutane

Table I-15 and Figures I-28, I-29, and I-30 show the dependence of  $\alpha/P$ ,  $(\alpha-\eta)/P$  and the smoothed values of  $\eta/P$  on  $E/P$  for  $\text{C}_4\text{F}_8$ . For comparison, the curves for  $\text{C}_3\text{F}_8$  are included. It was found that, for reasons unknown, the scatter of results for this compound was unusually high, and attempts to establish a pressure dependence were inconclusive.

From slopes of the lines in Figure I-28 it is clear that  $B$  for  $\text{C}_4\text{F}_8$  is considerably higher than that for  $\text{C}_3\text{F}_8$ . The cross section,  $B/\epsilon_1^{3/2}$ , given in Table I-13 is relatively even higher than that for  $\text{C}_3\text{F}_8$ . The attachment coefficient is only slightly lower for  $\text{C}_4\text{F}_8$  than for  $\text{C}_3\text{F}_8$ , as seen in Figure I-30. Thus, as is confirmed from the limiting value of  $E/P$  obtained from Figure I-29, this gas has an unusually high sparking potential for its molecular size. A comparison between measured sparking potentials and those calculated from our data are shown in Figure I-31, where it is seen that only fair agreement is obtained.

#### 9. Hexafluoropropene

The effect of introducing a double bond is illustrated in Figures I-32, I-33, and I-34 where we compare  $\text{C}_3\text{F}_8$  with  $\text{C}_2\text{F}_6$ . The data are given in Table I-16. This gas was unusual in that preliminary measurements showed a very low primary photocurrent. To restore the photocurrent to values similar to those used in measurements on the other compounds, it was necessary to increase the light intensity by removing a number of filtering screens normally present. Since on removal of the gas it returned immediately to its normal value, it is probable that absorption of the ultraviolet light by the gas, rather than a poisoning of the photoelectric cathode, was occurring.

It is clear from a comparison of the slopes of the lines in Figure I-32 that the double bond contributes significantly to the cross section for electron scattering. The difference is even more apparent on comparing the values of  $B/\epsilon_i^{3/2}$  in Table I-13 owing to the low ionization potential of  $C_3F_6$ . A similar, though not so pronounced, effect was observed<sup>(4)</sup> for the corresponding olefinic hydrocarbons.

The negative values for  $\eta/P$  appearing in Table I-16, as they occasionally appear in some of the other data, have, of course, no physical significance. They arise from errors in fitting as a result of the fact that the attachment coefficient is so low. It is clear that the attachment coefficient is surprisingly low in  $C_3F_6$ , being essentially zero for the lower values of  $E/P$ . This is reflected in the asymptotic approach of the  $(\alpha-\eta)/P$  curve to zero at low values of  $E/P$  with a consequent very low, if indeed positive, value for the limiting value of  $E/P$ . It appears that the value of  $\eta/P$  increases with increasing  $E/P$ , in contrast to the behavior of most of these compounds.

#### 10. t-Butyl Chloride

The ionization and attachment coefficients obtained are listed in Table I-17. Figure I-35 shows a plot of  $\alpha/P$  against  $P/E$ . The slope of this line gives a least squares value for  $B$  of  $457 \pm 14$  volts  $cm^{-1}$  torr $^{-1}$ , in good agreement with the value for *n*-butyl chloride<sup>(5)</sup> 471 volts  $cm^{-1}$  torr $^{-1}$ . The ionization potentials of the two are very nearly the same, so that, as has been found for the hydrocarbons, branching does not appear to influence the cross section for electron scattering.

A plot of  $(\alpha-\eta)/P$  against  $E/P$  is shown in Figure I-36. From this curve the limiting value of  $E/P$  is 88 volts  $cm^{-1}$  torr $^{-1}$ .

The dependence of attachment coefficient on  $E/P$  is shown in Figure I-37 for both *t*-butyl chloride and isopropyl chloride.<sup>(6)</sup> It is clear that in both compounds, unlike in *n*-butyl chloride, a small but definite amount of attachment occurs. The attachment coefficient is of the same order for both compounds in spite of the higher degree of branching in the *t*-butyl chloride.

#### 11. Discussion of Results

For the perfluoroalkanes, at least, the simple correlations between composite cross sections for electron scattering (more properly,  $B/\epsilon_i^{3/2}$ , or  $\rho\theta$ ) and molecular size that have been observed for the hydrocarbons and alkyl chlorides still appear to hold. Thus, as shown in Figure I-20,  $\rho\theta$  is proportional to the number of carbon-fluorine bonds, the values being somewhat smaller than for the corresponding hydrocarbons. This latter result is somewhat surprising in view of the fact that each fluorine atom possesses six non-bonding electrons, in its outer shell, which one might have expected to contribute to the scattering cross section. It seems likely that the Ramsauer cross section,  $\theta$ , is larger for each C-F scattering center than for the



corresponding C-H in the hydrocarbons, but that  $\rho$ , the probability that an electron colliding with the molecule will produce electronic excitation, is more than proportionately lower. The zero intercept in Figure I-20 suggests that, as with the hydrocarbons, the C-C bonds do not contribute to the cross sections.

The contribution of the double bond in  $C_3F_6$  to  $\rho\theta$  shown in Table I-13 also was observed in the olefinic hydrocarbons.<sup>(4)</sup> Using a value for  $\rho\theta$  for a single C-F bond of  $0.91 \text{ volt cm}^{-1} \text{ torr}^{-1} \text{ ev}^{-3/2}$  obtained from the slope of the line in Figure I-20, and assuming additivity of cross sections<sup>(3)</sup> we find that  $\rho\theta$  for the double bond is 11.0. This is much higher than the corresponding value for the hydrocarbons, 3.4. This suggests that if the attachment coefficient could be increased by "tailoring" of the molecule, such olefinic gases should have particularly high electric strengths.

The influence of molecular shape on the composite cross sections is of considerable interest. In all compounds investigated to date, no effect has been found of altering molecular shape, either by branching or cyclization. In the hydrocarbons, for example, the same values for  $\rho\theta$  were found for neopentane, normal pentene, and cyclohexane, all compounds containing 12 carbon-hydrogen bonds. This remains true of *t*-butyl chloride in this work where  $\rho\theta$  is the same as for *n*-butyl chloride. With octafluorocyclobutane, however, the composite cross section, as shown in Table I-13, is 1.8 times as large as the value for  $C_3F_8$ . The value is, in fact, larger than that for  $C_6F_{14}$ . Even allowing for any reasonable errors in the values for the ionization potentials could not change the conclusion that, in this case, cyclization has profoundly increased the composite cross section. Since the attachment coefficient does not differ greatly from that for  $C_3F_8$  (see Figure I-22) this gas should, and in fact does, have an unusually high electric strength (see Figure I-31).

An important conclusion that can be drawn from Figure I-23, relating the attachment coefficients to the number of fluorine atoms in the perfluoroalkanes, is that the relationship to geometric cross sections is rather complex. It had been hoped that simple relationships such as those found for the ionization coefficients would be observed. Nevertheless, it is possible to relate our attachment coefficients to mass spectrographic observations reported in Section A and to account for our results in terms of specific attachment processes.

The calculation of attachment coefficients requires a knowledge not only of the cross sections for attachment as a function of electron energy, but also of the energy distribution of the electrons in the gas for a particular value of  $E/P$ . While the cross sections for attachment were measured in Section A (see Figures I-11 to I-16) energy distributions are not available. Until such data become available for these gases, we may argue only qualitatively.

For the three lowest perfluoroalkanes, only  $F^-$  was observed in the mass spectrometer. As we have seen for  $C_4F_{10}$  this does not preclude the possibility that parent ions may be produced and stabilized by collision at the higher pressures of our experiments. However, since no pressure dependence was observed in our experiments, utilizing sparking potential and prebreakdown current measurements, for the three smaller molecules it seems safe to conclude that parent ions are not of importance over the pressure range we have examined.

A small amount of parent ion is found in the mass spectrometer for  $C_4F_{10}$  together with small amounts of a number of other ions. However,  $F^-$  still seems to be the predominant ion (Figure I-14). Again the pressure dependence we have observed shows that this is true also for our measurements of attachment coefficients, although at the higher pressures used in measuring sparking potentials the parent ion plays an important role. In  $C_6F_{14}$  the parent ion predominates in the mass spectrometer, with a number of other ions showing appreciable relative abundances (Figure I-15).

A plot of peak ion currents for  $F^-$  and parent ion against number of carbon-fluorine bonds is shown in Figure I-38, the data being taken from Figure I-16. It is evident that the cross section for  $F^-$  goes through a maximum at  $C_2F_6$  or  $C_3F_8$ , and that for the parent ion rises from zero above  $C_3F_8$ . These results now permit an explanation of the dependence of attachment coefficient on chain length shown in Figure I-23. Since the principal negative ion up to and including  $C_4F_{10}$  at low pressures is  $F^-$ , this part of the attachment coefficient curve mirrors that for  $F^-$  in Figure I-38. The rise in attachment coefficient at  $C_6F_{14}$  is largely due to the importance of the parent ion even at the lowest pressures we have used. As is evident in Figure I-16, the parent ions have relatively large cross sections at considerably lower electron energies than the  $F^-$  ions. It is undoubtedly for this reason that, while in Figure I-38, the peak cross section for  $C_6F_{14}^-$  is lower than, for example, that for  $F^-$  for either  $C_2F_6$  or  $C_3F_8$ , the attachment coefficient for  $C_6F_{14}$  is by far the largest value. Thus, more low-energy electrons in the distribution can lead to attachment in the latter gas.

In Figure I-39 we have plotted as a function of electron energy the total cross section for all negative ions produced in each of the perfluoroalkanes. It is interesting to note that if we assume the electron energy distribution to have the same mean energy at the limiting value of  $E/P$ , 3.3 ev, and plot relative cross sections (normalized at  $C_6F_{14}$ ) taken from these curves against the number of carbon-fluorine bonds, the points shown in Figure I-23 result. In view of the assumptions made the agreement with measured values is surprisingly good. It seems clear that the mean electron energies in  $CF_4$  and  $C_2F_6$  must be somewhat higher than the constant value assumed above in order to produce a better fit.

The danger of such qualitative arguments, however, may be illustrated by comparing the predicted dependence of  $\eta/P$  on  $E/P$  using the above value of 3.3 eV for the mean energy of the distribution. It is clear that with  $C_6F_{14}$  an increase in  $E/P$  with its consequent increase in the mean energy should cause a decrease in attachment, just as observed in Figure I-22. However, for the other gases this value for the mean energy places us on the low-energy side of the cross section curves, so that an increase in  $E/P$  should cause an increase in  $\eta/P$ , contrary to what we observe in Figure I-22. It seems clear that more quantitative arguments must await further data on the true electron energy distributions in these gases.

The increase in attachment coefficient caused by branching of the alkyl chlorides, as evidenced in isopropyl chloride, (6) was found also in this work in *t*-butyl chloride (see Figure I-37). The magnitude of the effect is about the same in both compounds. The very small attachment found in  $C_3F_8$  (see Figure I-34) is somewhat surprising, and further measurements on other olefinic compounds containing halogen atoms should prove of interest. If, for example, the addition of a  $CF_2$  group should markedly increase the attachment coefficient, then, as has been already noted, the large value of  $\rho\theta$  due to the double bond may result in a gas of particularly high electric strength. The fact that  $C_3F_8$  is the only one of the fluorocarbons investigated for which the attachment coefficient increases with increasing  $E/P$  suggests that the attachment process occurs at higher electron energies in this gas, relative to the peak in the electron energy distribution. This may be partly due to the low ionization potential of the gas, which results in a relatively low average electron energy.

The dependence of attachment coefficient on pressure in  $C_4F_{10}$  is of particular interest, not only because it allows us to explain discrepancies between measured electric strengths and those calculated from ionization and attachment coefficients, but also because it gives us some insight into the nature of the attachment processes.

As we have suggested above an increase in  $\eta/P$  with increasing pressure such as we have observed might be expected if the parent negative ion were metastable, reverting to the original molecule and electron unless stabilized by energy removal on collision with another molecule. Massey and Burhop<sup>(22)</sup> have considered the consequences of such a situation. Thus, let the average lifetime of a negative ion before spontaneous dissociation in the absence of collisional stabilization be  $\theta$ , and let  $\tau$  be the average time taken for collisional stabilization. If, at time  $t = 0$ , we have an excited negative ion, the chance that it will not have dissociated in time  $t$  is  $e^{-t/\theta}$ . The chance that it will be stabilized by collision in a time between  $t$  and  $t + dt$  is  $e^{-t/\tau} dt/\tau$ , so that the total probability of the ion being stabilized by collision before it breaks up will be

$$\rho = \int_0^{\infty} \exp \left[ -t \left( \frac{1}{\tau} + \frac{1}{\theta} \right) \right] \frac{dt}{\tau}$$

$$= \theta / (\theta + \tau)$$

But  $1/\tau \propto P$ , and  $\theta$  is independent of  $P$ , so that

$$\rho = P / (P + P')$$

where  $P'$  is the pressure for which  $\theta = \tau$ . The observed attachment coefficient may be written

$$\frac{\eta}{P} = \rho \left( \frac{\eta}{P} \right)_{P=\infty} + \left( \frac{\eta}{P} \right)_{P=0}$$

where the subscripts refer to infinite and zero pressure, respectively. The last term is included to allow for dissociative attachment processes that may not proceed via the parent ion. Combining these results we have

$$\frac{1}{\eta/P - (\eta/P)_{P=0}} = \frac{1}{(\eta/P)_{P=\infty}} + \frac{P'}{P} \cdot \frac{1}{\left( \frac{\eta}{P} \right)_{P=\infty}}$$

Examination of Figures I-26 and I-27 shows that it is difficult to decide whether  $(\eta/P)_{P=0}$  is zero, though it must have a fairly small value. If it is zero a plot of  $P/\eta$  against  $1/P$  should produce a straight line, and any curvature may be attributed to a nonzero value for  $(\eta/P)_{P=0}$ . In testing this theory a procedure has been adopted to reduce the scatter in the results. As has already been discussed, because of the nature of the experiment,  $(\alpha-\eta)/P$  can usually be measured much more accurately than either  $\alpha/P$  or  $\eta/P$ . Since there is no theoretical reason to expect that  $\alpha/P$  will be pressure sensitive, and in fact the data of Figures I-26 and I-27 support this conclusion within the scatter of the measurements, we have assumed constant values for  $\alpha/P$ , (0.57 for  $E/P = 125$  and 1.00 for  $E/P = 150$ ) and have recalculated  $\eta/P$  from these and the corresponding values of  $(\alpha-\eta)/P$ .

The reciprocal plots suggested by the theory are shown in Figure I-40 and within the limits of the scatter the curves are linear. From the slopes and intercepts we may calculate values for  $(\eta/P)_{P=\infty}$  and  $P'$ , and these are shown in Table I-18. The value of  $(\eta/P)_{P=\infty}$  drops strongly with increasing  $E/P$ . It may be noted that, using the low pressure values for  $\eta/P$ ,  $(\alpha-\eta)/P$  is positive even for  $E/P$  of 125, so that the limiting value of  $E/P$  is predicted to be lower than this value. However, with the values of  $(\eta/P)_{P=\infty}$ , which should apply to our measurements of sparking potentials,  $(\alpha-\eta)/P$  is negative at  $E/P$

of 125 and positive at E/P of 150, indicating that at higher pressures the limiting value of E/P should lie between these values. As has already been mentioned, the limiting E/P from sparking potential measurements is about 140 for  $C_4F_{10}$  (Figure I-24).

The value  $P'$ , the pressure at which  $\tau = \theta$ , is about 4 torr. In view of the scatter of the data at E/P = 150, it cannot be definitely concluded that  $P'$  is dependent upon E/P, though it is not strongly dependent upon it. Assuming that one molecular collision is sufficient to stabilize the negative ion, one may calculate the value  $\tau$  at  $P'$  and thus the value of  $\theta$ . The value of  $\tau$  is given by kinetic theory as

$$\tau = \frac{\lambda}{\bar{c}} = \frac{1}{\sqrt{2} nr^2 \left( \frac{\pi RT}{M} \right)^{1/2}}$$

where  $\lambda$  is the molecular mean free path;  $\bar{c}$  is the mean velocity;  $n$  is the number of molecules per cc;  $r$  is the molecular radius;  $T$  is the absolute temperature; and  $M$  is the molecular weight.

No direct measurements of the molecular radius of  $C_4F_{10}$  have been made. Using values for bond lengths given by Pauling<sup>(23)</sup> and approximating the resulting cylindrical molecule by a sphere gives a molecular radius of 3.5 Å. The critical pressure and temperature of  $C_4F_{10}$  have been measured<sup>(24)</sup> at 24 atm and 113.3°C. From these we may calculate a value for the Van der Waals constant  $b$ ,

$$b = \frac{RT_c}{8P_c} = 165 \text{ cc/mole}$$

In many cases, this is about four times the molar volume, from which we deduce that  $r = 2.5$  Å. Since the actual collision radius for energy transfer may be somewhat different from either of these values, a precise number cannot be given at this time. For purposes of calculation we shall take the larger value of  $r = 3.5$  Å.

The value of  $\tau$  at  $P = 4$  torr, and thus of  $\theta$ , calculated in this way is  $8.7 \times 10^{-6}$  second. Such a value for the mean lifetime of a vibrationally excited  $C_4F_{10}^-$  ion is consistent with mass spectrometric data now available. Since the lifetime of an ion must be greater than about  $10^{-6}$  second in order that it may be detected with a mass spectrometer, our value would explain the failure of investigators to find it to date. However, it might be expected that occasional ions may have a sufficiently long lifetime so that a sensitive mass spectrometer might detect a small peak. Furthermore, it must be recalled that the lifetime  $\theta$ , as calculated, represents a minimum value, since

more than the one kinetic theory collision assumed in the calculation above may be required for stabilization of the ion. For these reasons a careful search was made for the parent negative ion of  $C_4F_{10}$ , and, as shown in Section A, a small peak was observed.

As has been suggested above, agreement between sparking potentials measured up to pressures of 500 torr and those calculated from our values of  $\alpha$  and  $\eta$ , measured down to pressures of about 2 torr, indicates that  $\eta/P$  is independent of pressure, at least over this pressure range. From Figure I-25 this appears to be true for the lower members of the perfluoroalkanes series,  $CF_4$ ,  $C_2F_6$ , and very nearly,  $C_3F_8$ . On the basis of the theory outlined above, this may be interpreted as indicating that the lifetime,  $\theta$ , of these compounds with their fewer vibrational modes is sufficiently short so that collisional stabilization cannot occur at the maximum pressures used. Thus, the pressure,  $P'$ , at which a transition occurs from lower to higher values of  $\eta/P$  is above 500 mm. Since, for  $C_4F_{10}$ ,  $P'$  appears to be about 4 torr, it is to be expected that for  $C_6F_{14}$ , parent negative ions will be stabilized over the pressure range we have been able to investigate. This is consistent with the mass spectrometer observations of Section A where  $C_6F_{14}^-$  is found to be a predominant negative ion. The agreement between measured and calculated sparking potentials is much better for  $C_6F_{14}$  than for  $C_4F_{10}$  (using low-pressure measurements) though some disagreement still exists as shown in Figures I-24 and I-25. Whether the disagreement for  $C_6F_{14}$  is significant is not known at this time. Attempts to measure a pressure dependence of  $\eta/P$  over the range 1 to 10 torr as shown in Table I-12 at  $E/P$  of 230 must be considered inconclusive.

## 12. Conclusions

1. Measurements of ionization and attachment coefficients have been made on five normal perfluoroalkanes,  $CF_4$ ,  $C_2F_6$ ,  $C_3F_8$ ,  $C_4F_{10}$ , and  $C_6F_{14}$ , as well as cyclic  $C_4F_8$ , the olefin  $C_3F_6$ , and  $t\text{-}C_4H_9Cl$ .

2. As has been previously found for hydrocarbons, the "composite" cross sections for electron scattering obtained from ionization coefficients are linear functions of the number of carbon-fluorine bonds or fluorine atoms in the molecules. The value per C-F bond is slightly lower than that for the C-H bond. As for the hydrocarbons, the C-C bonds do not appear to contribute to the cross sections. Values of cross sections for  $c\text{-}C_4F_8$  and  $C_3F_6$  are inordinately high.  $t\text{-}C_4H_9Cl$  has the same cross section as  $n\text{-}C_4H_9Cl$ , again showing the lack of influence of branching.

3. A comparison of measured sparking potentials and those calculated from ionization and attachment coefficients shows reasonably good agreement for all gases except  $C_4F_{10}$ . The disagreement has been identified with a pressure dependence of  $\eta/P$ .

4. The dependence of  $\eta/P$  on pressure for  $C_4F_{10}$  has been explained in terms of a metastable parent negative ion that can be stabilized by collision. It is postulated that the lifetime of the negative ion increases with increasing molecular complexity because of sharing of excess energy among the vibrational modes. For  $C_4F_{10}$  the lifetime is  $>10^{-8}$  second.

5. For all gases except  $C_3F_8$ ,  $\eta/P$  decreases with increasing  $E/P$  over the range of  $E/P$  for which reliable measurements could be made. For  $C_3F_8$ ,  $\eta/P$  increased with increasing  $E/P$ .

6. Values of  $\eta/P$  are not simply related to geometric cross sections, as has been found to be usually true for  $\alpha/P$ . It appears that until a detailed quantum mechanical treatment of attachment in polyatomic molecules is available, reliable prediction of values for  $\eta/P$  will not be possible. Certain trends may, however, be useful. For example, chain branching in the alkyl chlorides leads to attachment in the two cases investigated: isopropyl chloride and t-butyl chloride.

7. A semiquantitative correlation between attachment cross sections measured in the mass spectrometer and  $\eta/P$  has been found for the perfluoroalkanes, and the processes responsible for attachment have been identified. For the lower three members, simple dissociative attachment to produce  $F^-$  is the most important process. This is true also of  $C_4F_{10}$  below about 2 torr. At higher pressures the production of  $C_4F_{10}^-$  becomes of major importance. For  $C_6F_{14}$ ,  $F^-$  is of little significance, and parent ion production dominates. Several other ions also contribute appreciably.

## APPENDIX

### IDENTIFICATION OF THE SLOPE OF THE $V_S$ - $P\delta$ LINES WITH $(E/P)_{lim}$

According to the Townsend criterion for breakdown,

$$\frac{\gamma \alpha}{(\alpha - \eta)} \cdot \exp(\alpha - \eta) \delta = 1 \quad ,$$

neglecting unity compared with  $\exp(\alpha - \eta) \delta$ . Rewriting, we have

$$\frac{(\alpha - \eta)}{P} \cdot P \delta = \ln \left[ \frac{(\alpha - \eta)}{\alpha \cdot \gamma} \right] \quad .$$

Over the range of  $E/P$  covered in our sparking potential measurements, the term on the right may be considered a constant,  $K$ , unless  $\gamma$  changes very rapidly with  $E/P$ .

To the extent that  $(\alpha - \eta)/P$  may be considered linear with respect to  $E/P$  over the  $E/P$  range of interest, we may write

$$\frac{(\alpha - \eta)}{P} = a \left[ E/P \cdot \left( \frac{E}{P} \right)_{lim} \right] \quad .$$

By combining these two expressions for  $(\alpha - \eta)/P$  and writing

$$E/P = V_S/P\delta \quad ,$$

we have

$$V_S = \left( \frac{E}{P} \right)_{lim} \cdot P \delta + \frac{K}{a} \quad .$$

Thus, to the extent of the approximations made, the slope of the  $V_S$  vs  $P\delta$  curve may be identified with  $(E/P)_{lim}$ .



## REFERENCES

1. J. C. Devins, H. L. Greenlaus, D. R. Johnston, L. Y. DuPont, A. L. Lynn, A. Pletenik, and H. G. Pfeiffer, "Research and Development on Corona-Resistant Materials," ASD Technical Rept. 61-693, Section C.
2. M. A. Harrison and R. Geballe, *Phys. Rev.*, 91, 1 (1953).
3. J. C. Devins and R. W. Crowe, *J. Chem. Phys.*, 25, 1053 (1956).
4. R. W. Crowe and J. C. Devins, *J. Chem. Phys.*, 33, 413 (1960).
5. J. C. Devins and O. H. LeBlanc, Jr., *Nature*, 187, 409 (1960).
6. J. C. Devins and O. H. LeBlanc, Jr., unpublished work.
7. T. M. Reed, III, *J. Chromatography*, 9, 419 (1962).
8. J. W. Warren and J. D. Craggs, Mass Spectrometry, Institute of Petroleum, London (1952), p. 36.
9. M. M. Bibby and G. Carter, *Trans. Faraday Soc.*, 59, 2455 (1963).
10. V. H. Dibeler, R. M. Reese, and F. L. Mohler, *Phys. Rev.*, 87, 213 (1952).  
[The value for  $C_4F_{10}$  in this reference is in error and is corrected in *J. Nat. Bur. Stds.*, 49, 343 (1952).]
11. D. P. Stevenson and J. A. Hipple, *J. Am. Chem. Soc.*, 64, 2766 (1942).
12. R. E. Honig, *J. Chem. Phys.*, 16, 105 (1948).
13. J. L. Margrave, *J. Chem. Phys.*, 31, 1432 (1959).
14. F. H. Field and J. L. Franklin, Electron Impact Phenomena, Academic Press, New York (1957), p. 253.
15. F. H. Field and J. L. Franklin, ibid., p. 259.
16. F. H. Field and J. L. Franklin, ibid., p. 290.
17. O. H. LeBlanc and J. C. Devins, *Nature*, 188, 219 (1960).
18. J. C. Devins and R. W. Crowe, unpublished work.
19. F. H. Field and J. L. Franklin, loc. cit., pp. 194-202.

20. D. Edelson, J.E. Griffiths, and K.B. MacAfee, J. Chem. Phys., 37, 917 (1962).
21. L.M. Chanin, A.V. Phelps, and M.A. Biondi, Phys. Rev., 128, 219 (1962).
22. H.S.W. Massey and E.H.S. Burhop, Electronic and Ionic Impact Phenomena, Oxford at the Clarendon Press (1952), pp. 225-228.
23. L. Pauling, The Nature of the Chemical Bond, Oxford Univ. Press, London (1952), Chap. V.
24. H. Simons, Fluorine Chemistry, Vol. 1, Academic Press, New York (1950), p. 459.

**BLANK PAGE**

TABLE I-6  
MATERIALS USED IN THIS WORK

<u>Compound</u>	<u>Source</u>	<u>Purification</u>	<u>Purity (%)</u>
CF <sub>4</sub>	Matheson	None	> 99
C <sub>2</sub> F <sub>6</sub>	duPont	None	> 99.9
C <sub>3</sub> F <sub>8</sub>	Matheson	None	> 99
<u>n</u> -C <sub>4</sub> F <sub>10</sub> (No. 1)	Columbia	None	> 98
<u>n</u> -C <sub>4</sub> F <sub>10</sub> (No. 2)	Columbia	None	> 99
<u>n</u> -C <sub>6</sub> F <sub>14</sub>	M.M.M.	VPC	?
<u>c</u> -C <sub>4</sub> F <sub>8</sub>	Peninsular	None	> 99
C <sub>3</sub> F <sub>8</sub>	Columbia	None	> 99
<u>t</u> -C <sub>4</sub> H <sub>9</sub> Cl	Eastman	Silica gel	> 99.9

TABLE I-7  
IONIZATION POTENTIALS OF GASES USED IN THIS WORK

<u>Compound</u>	<u>Ionization Potentials Measured (ev)</u>	<u>Ionization Potentials Used (ev)</u>
CF <sub>4</sub>	15.44 ± 0.05(a)	15.44
C <sub>2</sub> F <sub>6</sub>	15.4(b); 14.3(c)	14.1
C <sub>3</sub> F <sub>8</sub>	14.65(b); 14.4(c); 13.6(d)	13.5
<u>n</u> -C <sub>4</sub> F <sub>10</sub>	14.4(c)	13.0
<u>n</u> -C <sub>6</sub> F <sub>14</sub>	14.4(c)	12.5
<u>c</u> -C <sub>4</sub> F <sub>8</sub>	12.25(b)	12.25
C <sub>3</sub> F <sub>8</sub>	--	8.6
<u>t</u> -C <sub>4</sub> H <sub>9</sub> Cl	10.27(e)	10.3
<u>n</u> -C <sub>4</sub> H <sub>9</sub> Cl	--	10.6

(a) J. W. Warren and J. D. Craggs, Reference 8.

(b) M. M. Bibby and G. Carter, Reference 9.

(c) V. H. Dibeler, R. M. Reese, and F. L. Mohler, Reference 10.

(d) Value found in this work, Section A.

(e) D. P. Stevenson and J. A. Hipple, Reference 11.

TABLE I-8  
IONIZATION AND ATTACHMENT COEFFICIENTS  
FOR TETRAFLUOROMETHANE

$E/P$ ( $\text{cm}^{-1} \text{ torr}^{-1}$ )	$P$ (torr)	$(\alpha-\eta)/P$ ( $\text{cm}^{-1} \text{ torr}^{-1}$ )	$\alpha/P$ ( $\text{cm}^{-1} \text{ torr}^{-1}$ )	$\eta/P$ ( $\text{cm}^{-1} \text{ torr}^{-1}$ )
150	1.59	2.49	2.47	--
135	1.77	2.11	2.23	0.12
120	2.22	1.80	1.77	.03
100	2.73	1.30	1.36	.06
95	2.75	1.14	1.29	.15
90	3.28	1.07	1.08	.01
85	3.28	0.89	1.02	.13
80	3.28	.78	0.88	.10
70	3.83	.56	.63	.07
65	5.68	.42	.52	.10
60	5.68	.32	.41	.09
55	9.5	.17	.31	.14
50	5.68	.13	.25	.12
46	15.0	.01	.15	.14
40	15.0	- .08	.11	.19

TABLE I-9  
IONIZATION AND ATTACHMENT COEFFICIENTS  
FOR HEXAFLUOROETHANE

$E/P$ ( $\text{v cm}^{-1} \text{ torr}^{-1}$ )	$P$ (torr)	$(\alpha-\eta)/P$ ( $\text{cm}^{-1} \text{ torr}^{-1}$ )	$\alpha/P$ ( $\text{cm}^{-1} \text{ torr}^{-1}$ )	$\eta/P$ ( $\text{cm}^{-1} \text{ torr}^{-1}$ )
250	0.81	4.03	4.43	0.40
240	.81	3.77	4.16	.39
230	.81	3.49	4.18	.69
210	1.08	3.06	3.39	.33
200	1.16	2.80	3.02	.22
190	1.08	2.54	2.93	.39
180	1.16	2.28	2.52	.24
170	1.08	2.01	2.62	.62
160	1.16	1.77	1.98	.21
140	2.50	1.27	1.66	.39
130	2.50	1.00	1.50	.70
120	2.50	0.75	1.23	.48
110	6.62	.49	0.91	.42
100	6.62	.23	.74	.51
90	6.62	.02	.45	.43
85	10.0	- .09	.24	.33
85	10.0	- .08	.30	.38
75	10.0	- .11	.06	.17
75	10.0	- .14	.10	.24

TABLE I-10  
IONIZATION AND ATTACHMENT COEFFICIENTS  
FOR OCTAFLUOROPROPANE

$E/P$ ( $v \text{ cm}^{-1} \text{ torr}^{-1}$ )	$P$ (torr)	$(\alpha-\eta)/P$ ( $\text{cm}^{-1} \text{ torr}^{-1}$ )	$\alpha/P$ ( $\text{cm}^{-1} \text{ torr}^{-1}$ )	$\eta/P$ ( $\text{cm}^{-1} \text{ torr}^{-1}$ )
250	1.49	3.58	3.73	0.15
250	1.14	3.58	4.31	.74
250	1.14	3.54	3.60	.06
250	1.14	3.44	4.06	.62
225	1.49	3.00	2.83	--
210	1.41	2.60	2.67	.07
200	1.69	2.33	2.54	.21
190	1.69	2.08	2.25	.17
180	1.49	1.90	1.83	--
175	1.49	1.70	2.15	.45
170	2.90	1.60	2.13	.53
165	1.49	1.47	1.89	.42
155	2.90	1.26	1.66	.40
150	4.11	1.13	1.50	.37
150	2.25	1.12	1.53	.41
140	2.90	0.89	1.31	.42
140	2.25	.83	1.26	.43
130	4.11	.64	1.19	.55
125	4.11	.53	0.99	.46
115	10.0	.34	.68	.34
110	10.0	.23	.61	.38
100	2.25	.09	.33	.24
90	4.37	- .17	.32	.49
80	4.37	- .28	.18	.46

TABLE I-11  
IONIZATION AND ATTACHMENT COEFFICIENTS  
FOR DECAFLUOROBUTANE

$E/P$ ( $v \text{ cm}^{-1} \text{ torr}^{-1}$ )	$P$ (torr)	$\alpha-\eta/P$ ( $\text{cm}^{-1} \text{ torr}^{-1}$ )	$\alpha/P$ ( $\text{cm}^{-1} \text{ torr}^{-1}$ )	$\eta/P$ ( $\text{cm}^{-1} \text{ torr}^{-1}$ )
250	1.14	.3.43	3.52	0.09
228	1.13	2.99	3.06	.07
225	1.41	2.74	2.97	.23
200	1.69	2.14	2.31	.17
175	1.66	1.53	1.72	.19
160	2.22	1.22	1.39	.17
150	2.25	0.95	1.24	.29
135	2.73	.58	0.81	.23
125	2.59	.52	.74	.23
110	3.28	.09	.48	.38
100	3.26	- .06	.32	.38
90	3.83	- .20	.16	.35

TABLE I-12  
IONIZATION AND ATTACHMENT COEFFICIENTS  
FOR TETRADECAFLUOROHEXANE

$E/P$ ( $v \text{ cm}^{-1} \text{ torr}^{-1}$ )	$P$ (torr)	$\alpha-\eta/P$ ( $\text{cm}^{-1} \text{ torr}^{-1}$ )	$\alpha/P$ ( $\text{cm}^{-1} \text{ torr}^{-1}$ )	$\eta/P$ ( $\text{cm}^{-1} \text{ torr}^{-1}$ )
460	0.54	7.00	6.72	--
420	.54	5.98	5.52	--
380	.81	4.85	5.21	0.36
350	.81	4.03	4.37	.34
320	.54	3.30	3.84	.54
320	1.08	3.13	3.99	.86
320	2.12	3.10	4.16	1.06
300	0.54	2.66	3.75	1.09
300	1.08	2.59	3.42	0.83
300	2.12	3.54	3.16	.62
280	4.13	1.94	3.08	1.14
275	3.14	1.79	3.13	1.34
260	4.13	1.35	2.88	1.53
250	3.14	1.09	2.22	1.13
250	4.13	1.13	2.10	0.96
250	5.16	1.09	2.43	1.34
240	4.13	0.84	1.78	0.94
240	10.00	.67	1.16	.49
230	4.13	.54	1.63	1.09
230	5.16	.42	1.40	0.98
230	10.00	.36	1.22	.86
220	10.00	.08	1.08	1.00

TABLE I-13  
VALUES OF B AND COMPOSITE CROSS SECTIONS

	$\epsilon_i$ (ev)	$\epsilon_i^{3/2}$ (ev <sup>3/2</sup> )	B (v cm <sup>-1</sup> torr <sup>-1</sup> )	$B/\epsilon_i^{3/2}$ (v cm <sup>-1</sup> torr <sup>-1</sup> ev <sup>-3/2</sup> )
CF <sub>4</sub>	15.44	60.8	176 ± 14	2.89
C <sub>2</sub> F <sub>6</sub>	14.1*	52.9	307 ± 15	5.81
C <sub>3</sub> F <sub>8</sub>	13.5*	49.6	361 ± 22	7.28
C <sub>4</sub> F <sub>10</sub>	13.0*	46.8	420 ± 12	8.98
C <sub>6</sub> F <sub>14</sub>	12.5*	44.2	560 ± 17	12.68
C-C <sub>4</sub> F <sub>8</sub>	12.25	42.9	568 ± 23	13.2
C <sub>3</sub> F <sub>8</sub>	8.6	25.2	414 ± 20	16.4
t-C <sub>4</sub> H <sub>9</sub> Cl	10.6	34.5	457 ± 14	13.3

\*Assuming  $(\epsilon_i) C_n F_{2n+2} = 1.2 (\epsilon_i) C_n H_{2n+2}$ .

TABLE I-14  
PRESSURE DEPENDENCE OF THE IONIZATION  
AND ATTACHMENT COEFFICIENTS FOR DECAFLUOROBUTANE

E/P (v cm <sup>-1</sup> torr <sup>-1</sup> )	P (torr)	$(\alpha-\eta)/P$ (cm <sup>-1</sup> torr <sup>-1</sup> )	$\alpha/P$ (cm <sup>-1</sup> torr <sup>-1</sup> )	$\eta/P$ (cm <sup>-1</sup> torr <sup>-1</sup> )
125	1.08	0.23	0.79	0.56
125	2.12	.32	.61	.29
125	5.16	.22	.54	.32
125	7.5	.15	.55	.39
125	10.0	.17	.65	.48
125	10.0	.13	.59	.46
125	13.0	.08	.58	.50
125	15.0	.05	.55	.50
125	30.0	.00	.05	.05
150	2.12	.87	1.01	.14
150	5.16	.80	1.02	.22
150	10.0	.76	0.97	.21
150	15.0	.67	1.05	.38
150	20.0	.67	0.57	- .10



TABLE I-15  
IONIZATION AND ATTACHMENT COEFFICIENTS  
FOR OCTAFLUOROCYCLOBUTANE

$\frac{E}{P}$ ( $v \text{ cm}^{-1} \text{ torr}^{-1}$ )	P (torr)	$\frac{\alpha-\eta}{P}$ ( $\text{cm}^{-1} \text{ torr}^{-1}$ )	$\frac{\alpha}{P}$ ( $\text{cm}^{-1} \text{ torr}^{-1}$ )	$\frac{\eta}{P}$ ( $\text{cm}^{-1} \text{ torr}^{-1}$ )
250	1.08	3.39	3.66	0.27
200	1.59	2.02	2.09	.07
180	1.59	1.50	1.54	.04
160	1.08	1.06	1.30	.24
160	7.50	0.82	1.02	.20
150	4.13	.64	0.82	.18
150	5.16	.62	.78	.16
150	7.50	.57	.67	.10
150	10.00	.50	.62	.12

TABLE I-16  
IONIZATION AND ATTACHMENT COEFFICIENTS  
FOR HEXAFLUOROPROPENE

$\frac{E}{P}$ ( $v \text{ cm}^{-1} \text{ torr}^{-1}$ )	P (torr)	$\frac{(\alpha-\eta)}{P}$ ( $\text{cm}^{-1} \text{ torr}^{-1}$ )	$\frac{\alpha}{P}$ ( $\text{cm}^{-1} \text{ torr}^{-1}$ )	$\frac{\eta}{P}$ ( $\text{cm}^{-1} \text{ torr}^{-1}$ )
250	1.02	2.56	2.62	0.06
240	1.35	2.34	2.38	.04
230	1.35	2.05	2.21	.16
200	2.02	1.52	1.63	.11
180	2.02	1.15	1.20	.05
150	2.23	0.68	0.71	.03
140	6.36	.63	.63	.00
130	6.36	.49	.48	- .01
120	7.98	.37	.37	.00
100	7.98	.15	.21	- .06
90	20.00	.06	.15	.09
80	20.00	.07	.00	- .07

TABLE I-17  
IONIZATION AND ATTACHMENT COEFFICIENTS  
FOR t-BUTYL CHLORIDE

$E/P$ ( $v \text{ cm}^{-1} \text{ torr}^{-1}$ )	$P$ (torr)	$(\alpha-\eta)/P$ ( $\text{cm}^{-1} \text{ torr}^{-1}$ )	$\alpha/P$ ( $\text{cm}^{-1} \text{ torr}^{-1}$ )	$\eta/P$ ( $\text{cm}^{-1} \text{ torr}^{-1}$ )
250	1.00	3.85	3.91	0.05
235	1.00	3.41	3.39	--
230	1.02	3.26	3.64	.38
215	1.02	2.81	3.23	.42
200	1.59	2.41	2.44	.03
180	1.59	1.86	1.88	.02
160	1.59	1.33	1.42	.09
150	1.59	1.10	1.18	.08
125	7.08	0.55	0.63	.08
115	7.08	.37	.49	.12
110	7.08	.30	.35	.05
100	7.08	.14	.28	.14
100	19.60	.15	.27	.12
90	7.08	.02	.15	.13
80	7.08	- .07	.08	.15

TABLE I-18  
LIMITING VALUES FOR ATTACHMENT COEFFICIENTS  
AT HIGH PRESSURE AND THE TRANSITION PRESSURE

$E/P$ ( $v \text{ cm}^{-1} \text{ torr}^{-1}$ )	$\eta/P_{P=\infty}$ ( $\text{cm}^{-1} \text{ torr}^{-1}$ )	$P'$ (torr)
125	0.63	5.2
150	.36	3.9

**BLANK PAGE**

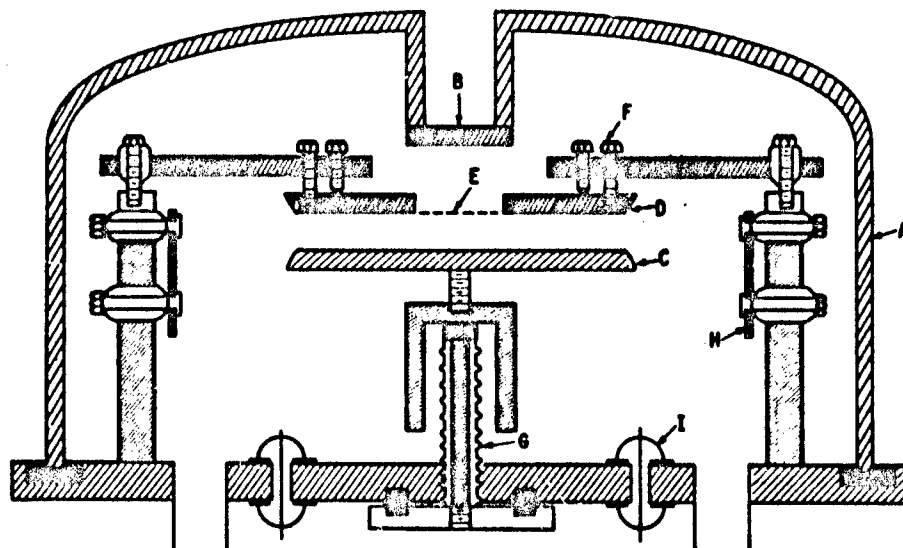


Figure I-17. Cell for Measuring Ionization and Attachment Coefficients

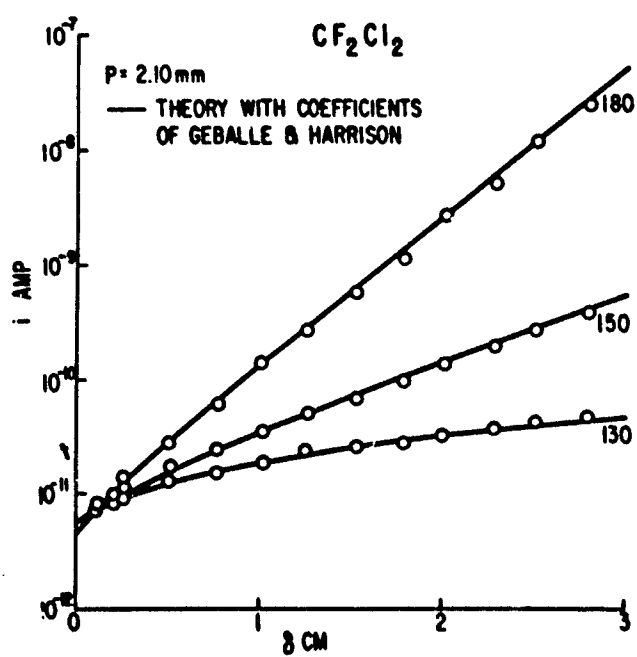


Figure I-18. Dependence of Current on Gap for  $\text{CF}_2\text{Cl}_2$  at Various Values of  $E/P$

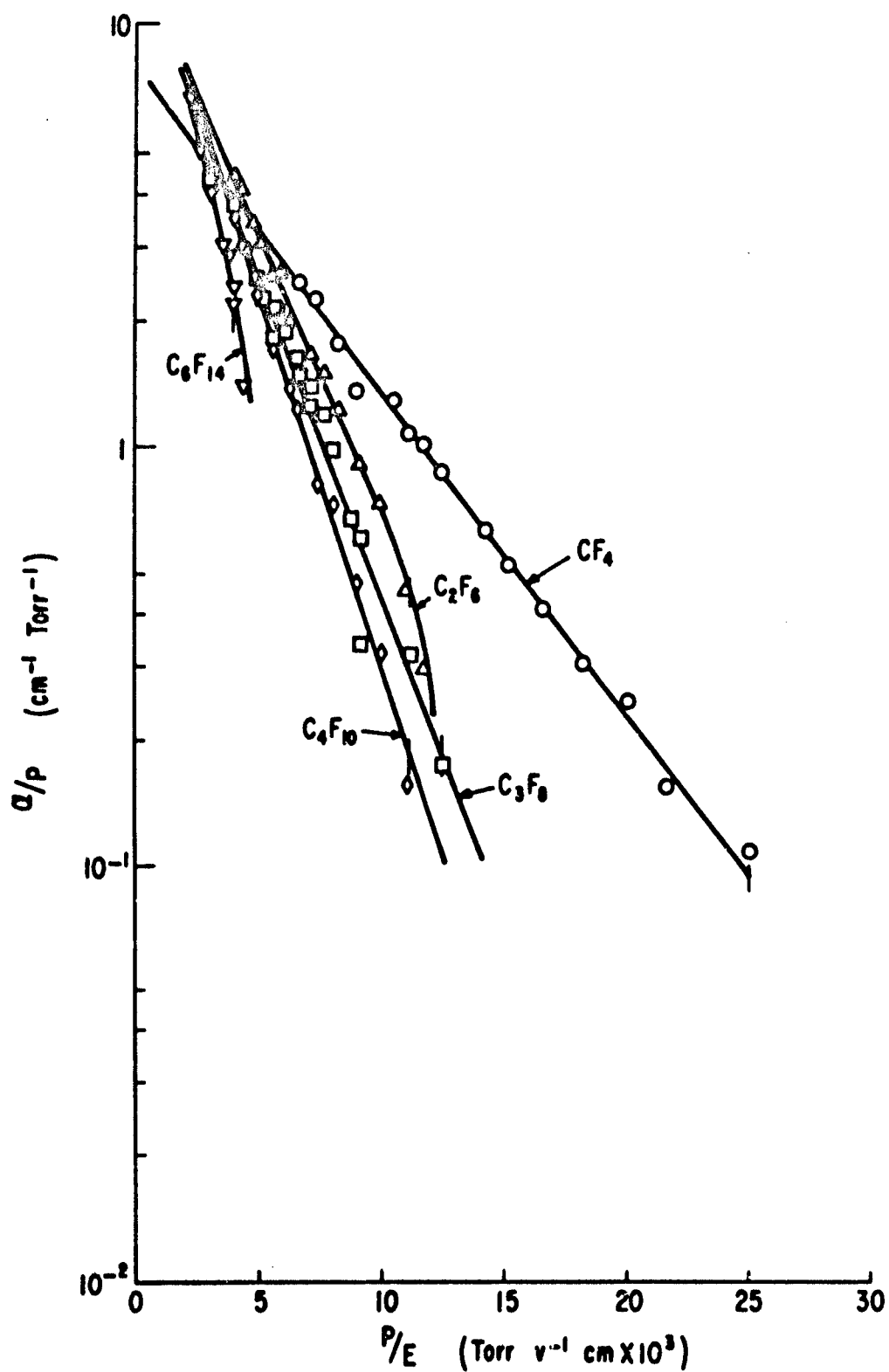


Figure I-19. Dependence of Ionization Coefficients on  $P/E$  for the Perfluoroalkanes

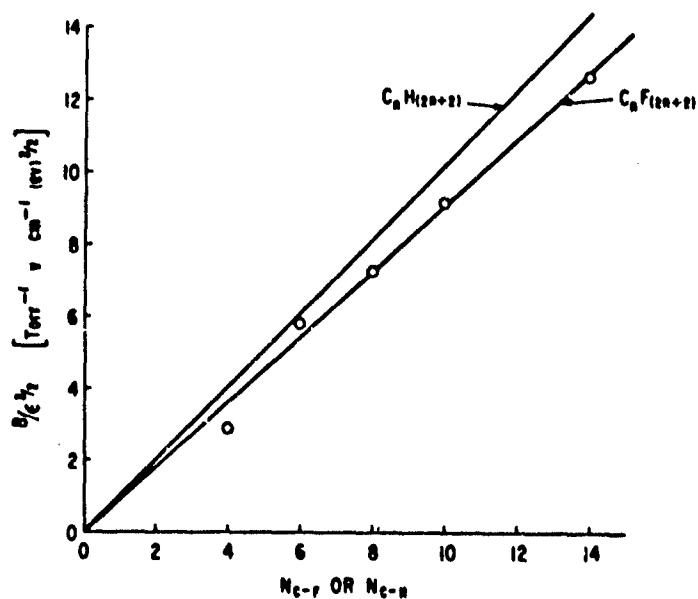


Figure I-20. Relationship Between Composite Cross Section and Number of Carbon-Fluorine or Carbon-Hydrogen Bonds in the Alkanes

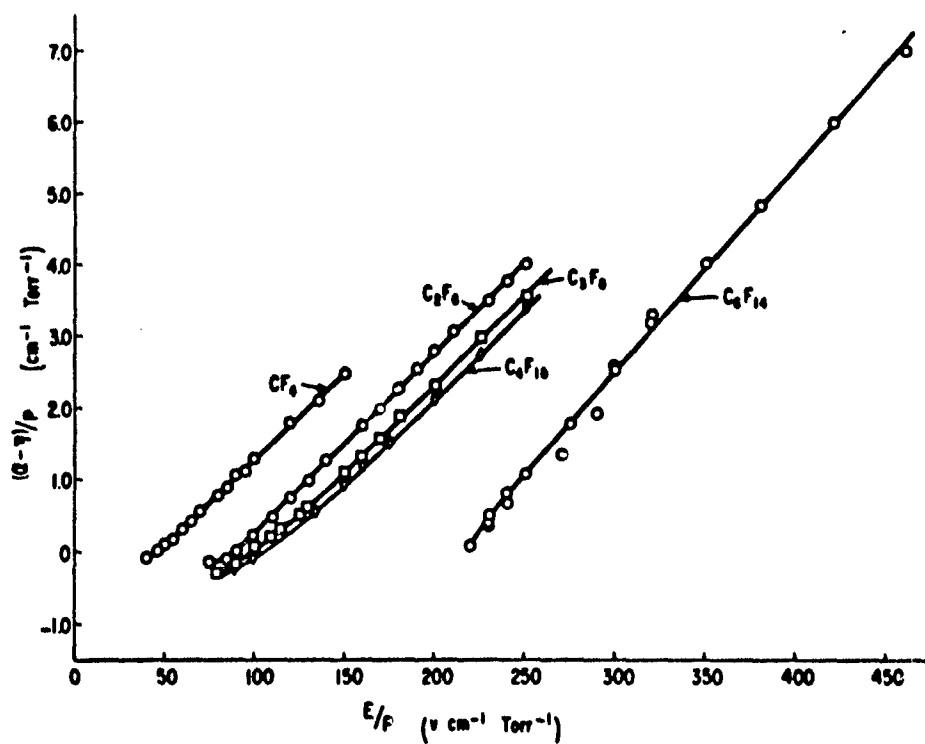


Figure I-21. Dependence of  $(\alpha-\eta)/P$  on  $E/P$  for the Perfluoroalkanes

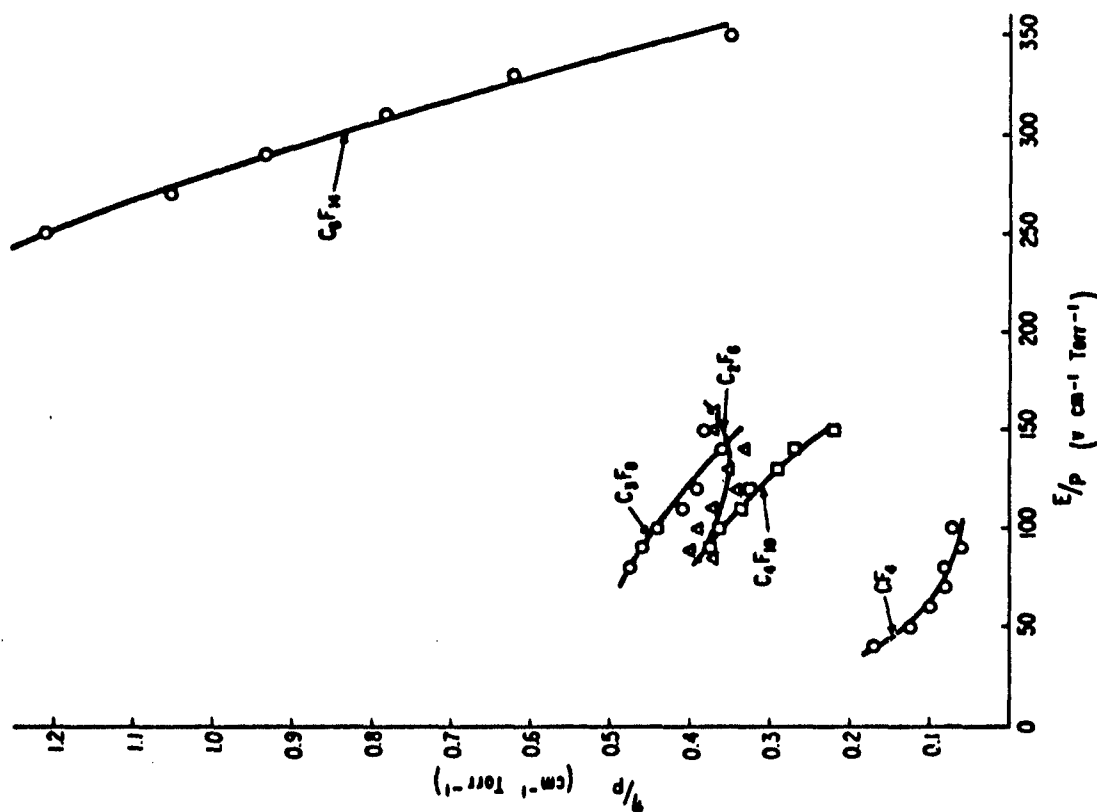


Figure I-22. Dependence of  $\eta/P$  on  $E/P$  for the Perfluoroalkanes

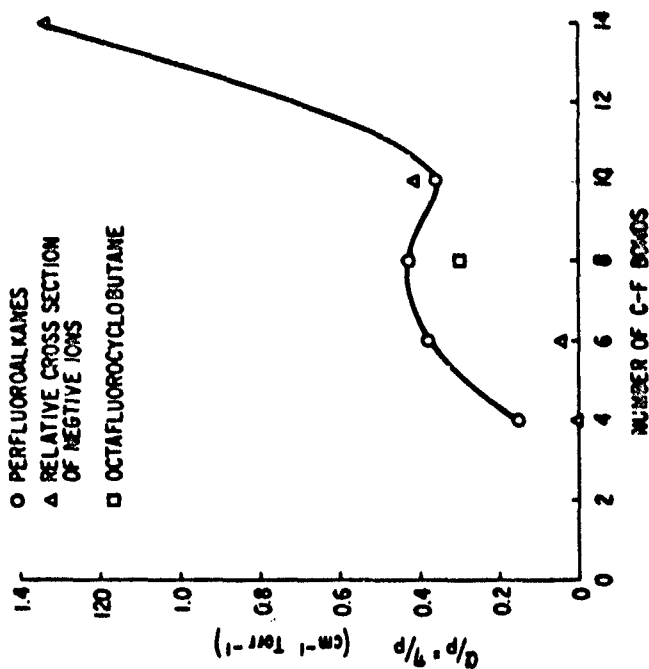


Figure I-23. Dependence of  $\nu/P$  Measured at the Limiting  $E/P$  on the Number of C-F Bonds for the Perfluoroalkanes

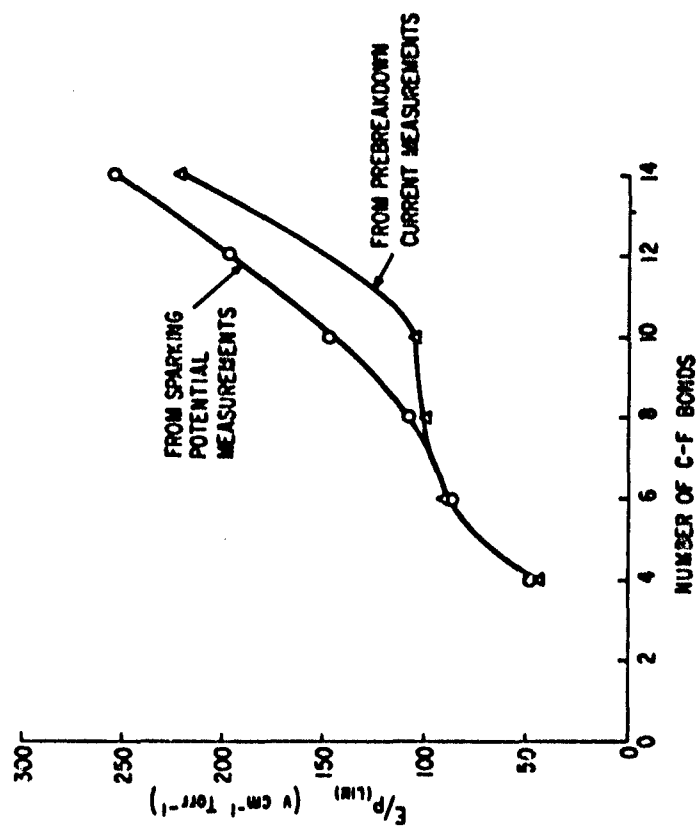


Figure I-24. Variation of  $(E/P)_{lim}$  with Chain Length for the Perfluoroalkanes

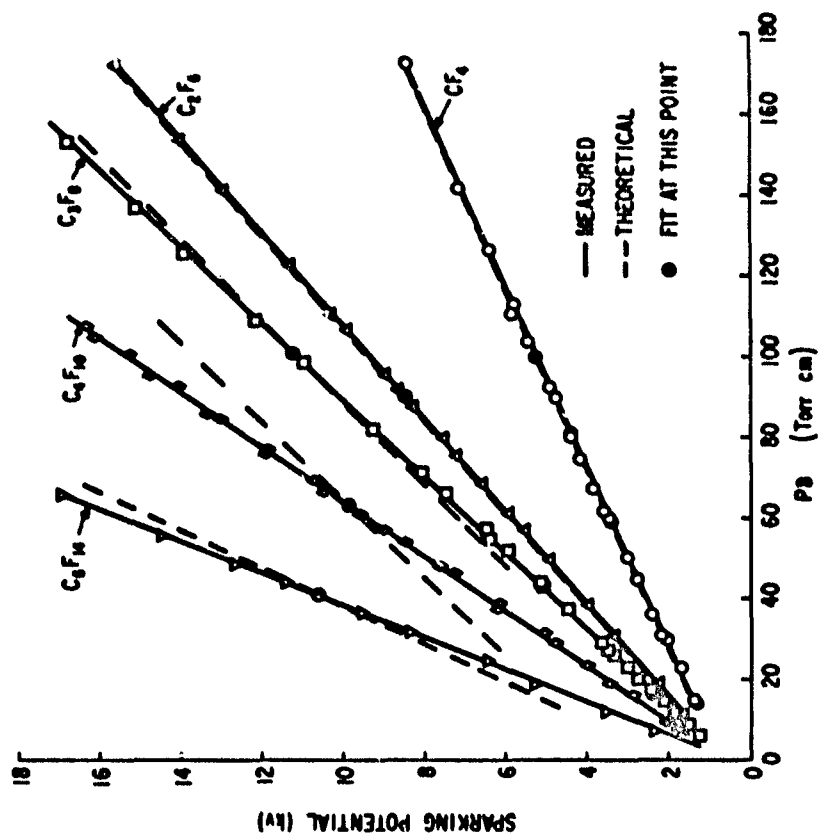


Figure I-25. Comparison of Measured and Calculated Values of Sparking Potential for the Perfluoroalkanes



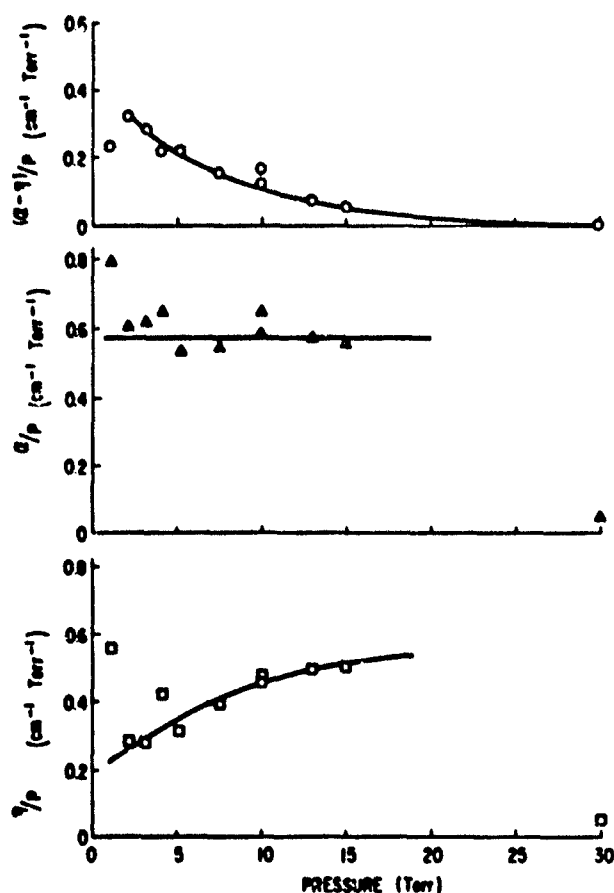


Figure I-26. Dependence of  $\alpha/P$ ,  $(\alpha - \eta)/P$ , and  $\eta/P$  on Pressure for  $C_4F_{10}$  at  $E/P$  of 125 Volts  $cm^{-1}$  torr<sup>-1</sup>

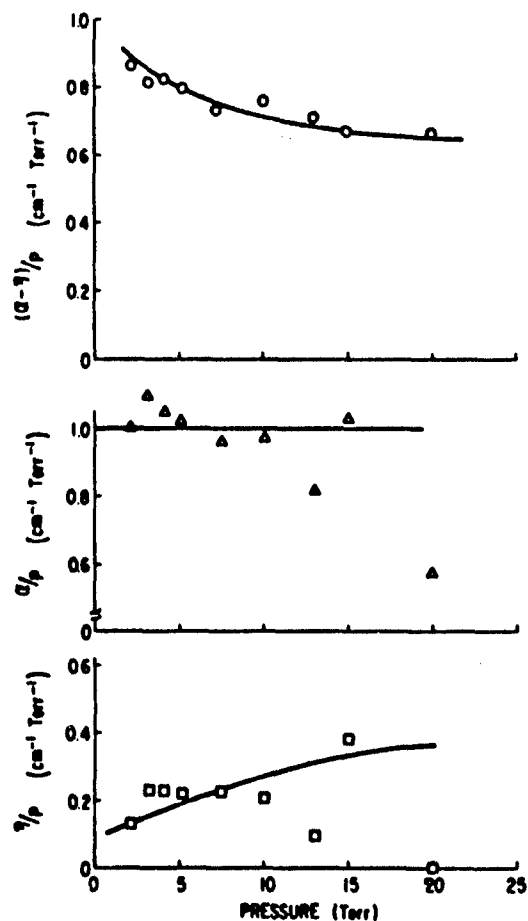


Figure I-27. Dependence of  $\alpha/P$ ,  $(\alpha - \eta)/P$ , and  $\eta/P$  on Pressure for  $C_4F_{10}$  at  $E/P$  of 150 Volts  $cm^{-1}$  torr<sup>-1</sup>

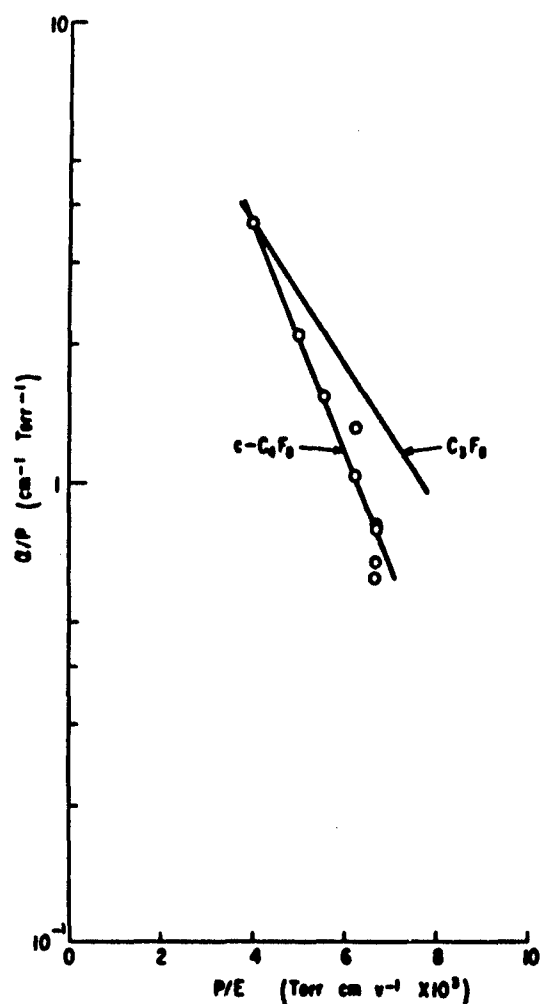


Figure I-28. Comparison of the Dependence of  $\alpha/P$  on  $P/E$  for Octafluorocyclobutane and Octafluoropropane

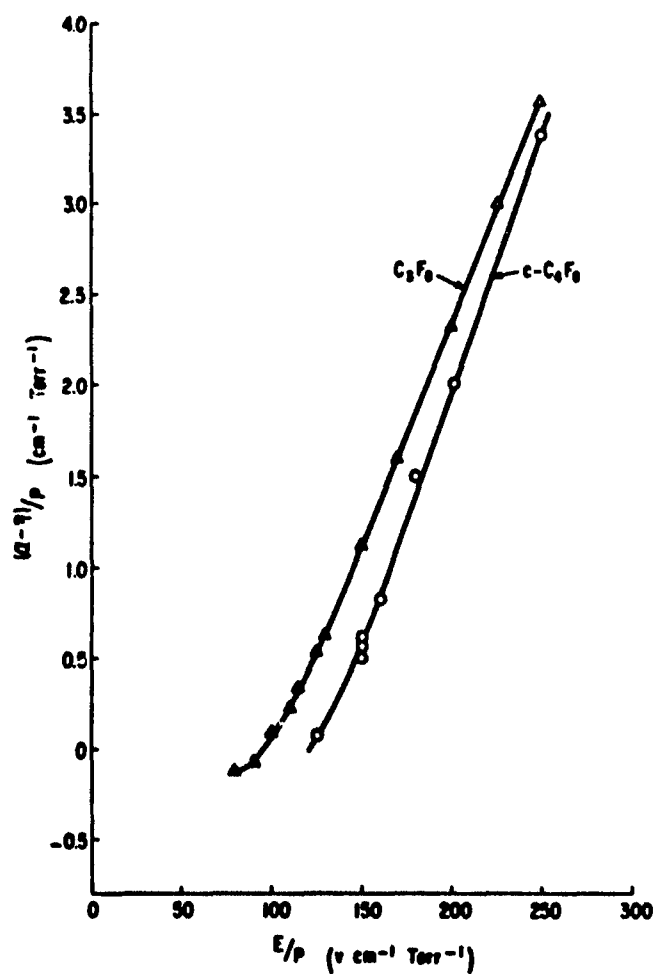


Figure I-29. Comparison of the Dependence of  $(\alpha-\eta)/P$  on  $E/P$  for Octafluorocyclobutane and Octafluoropropane

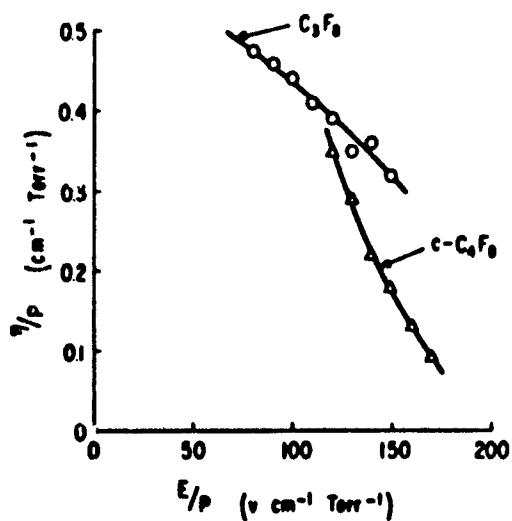


Figure I-30. Comparison of the Dependence of  $\eta/P$  on  $E/P$  for Octafluorocyclobutane and Octafluoropropane

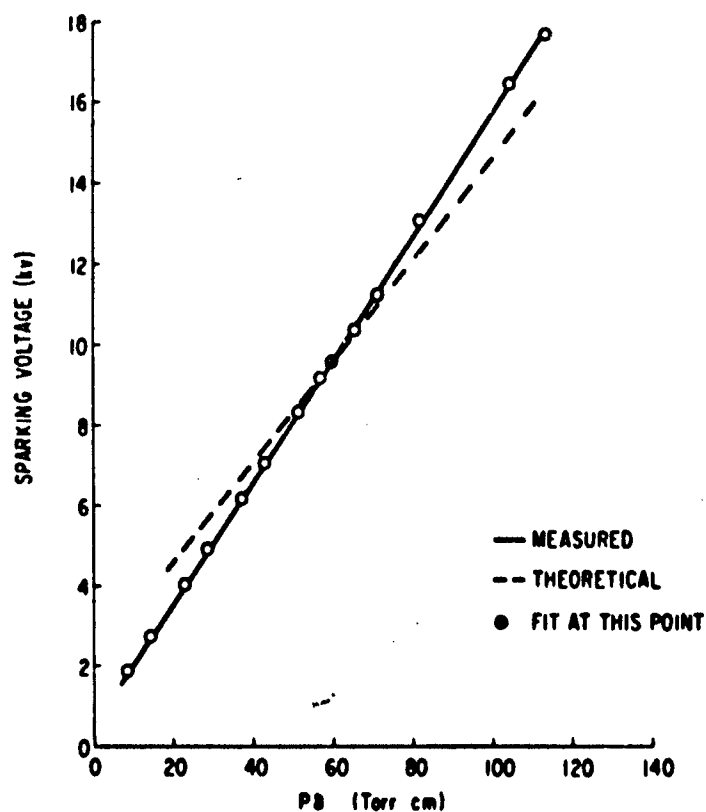


Figure I-31. Comparison of Measured and Calculated Values of Sparking Potential for Octafluorocyclobutane

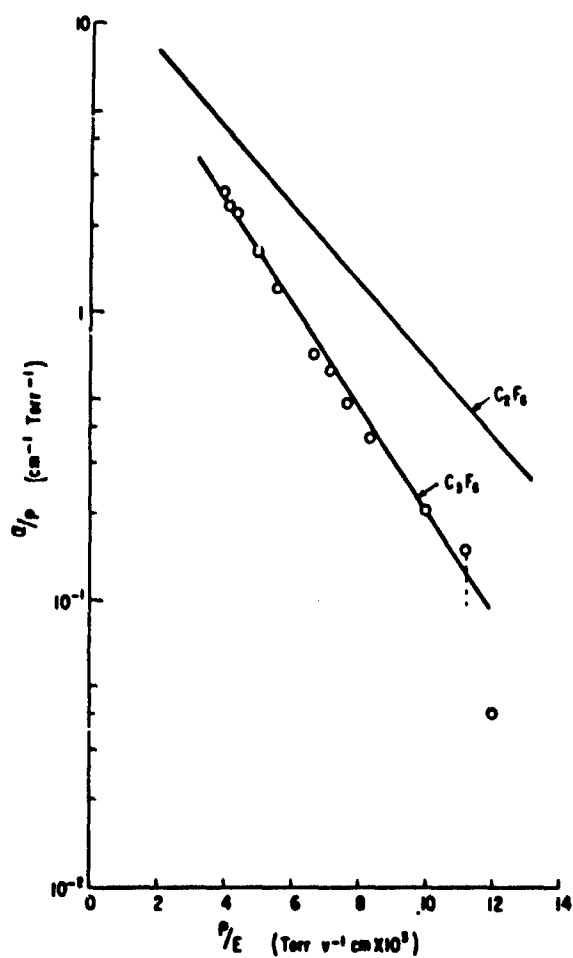


Figure I-32. Comparison of the Dependence of  $\alpha/P$  on  $P/E$  for Hexafluoropropene and Hexafluoroethane

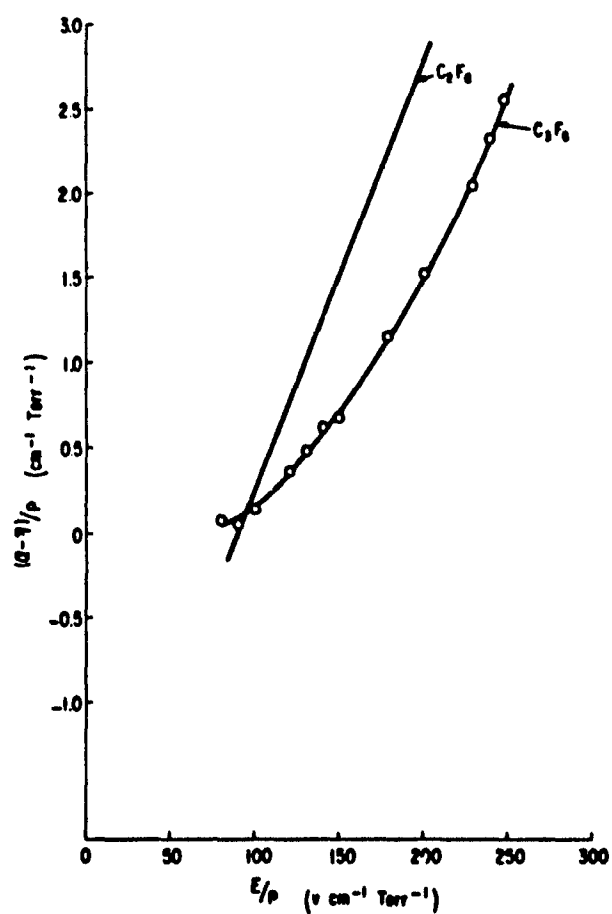


Figure I-33. Comparison of the Dependence of  $(\alpha-\eta)/P$  on  $E/P$  for Hexafluoropropene and Hexafluoroethane

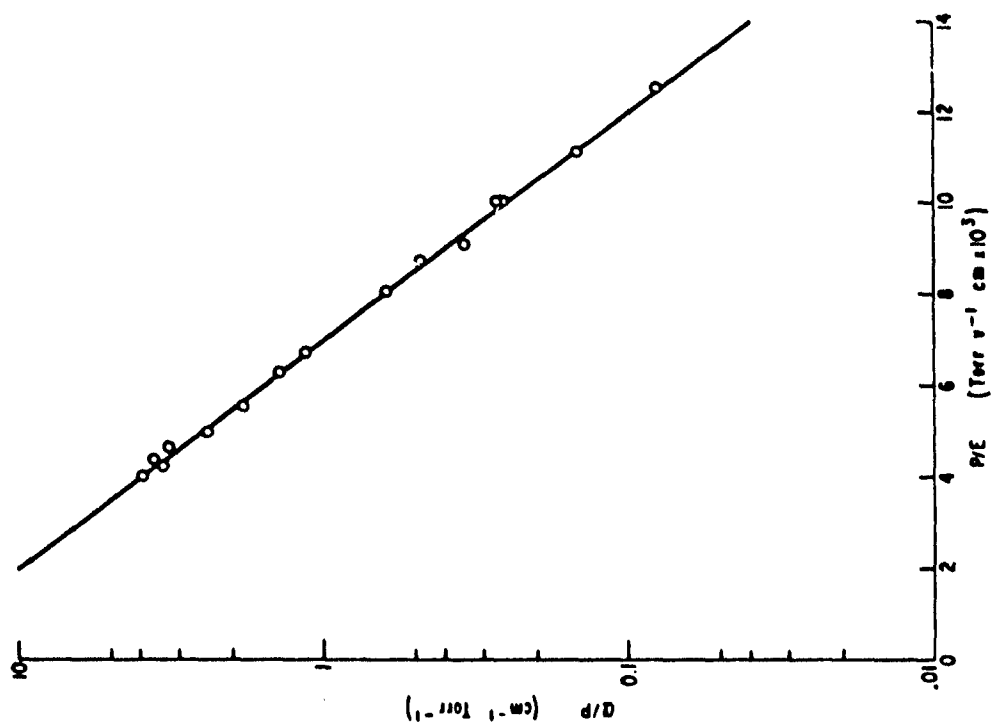


Figure I-35. Dependence of  $\alpha/P$  on  $P/E$  for  $t$ -Butyl Chloride

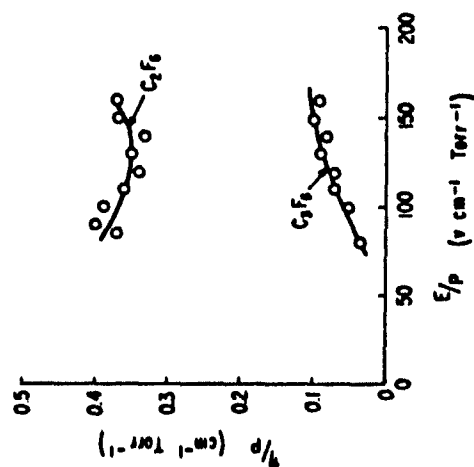


Figure I-34. Comparison of the Dependence of  $n/P$  on  $E/P$  for Hexafluoropropene and Hexafluoroethane

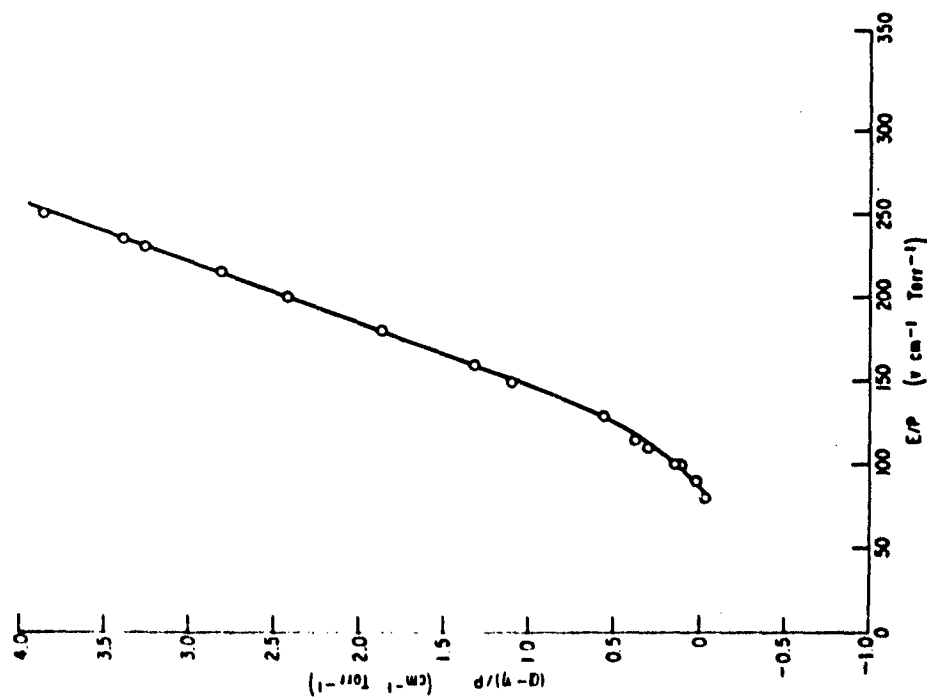


Figure I-36. Dependence of  $(n-n)/P$  on  $E/P$  for *t*-Butyl Chloride

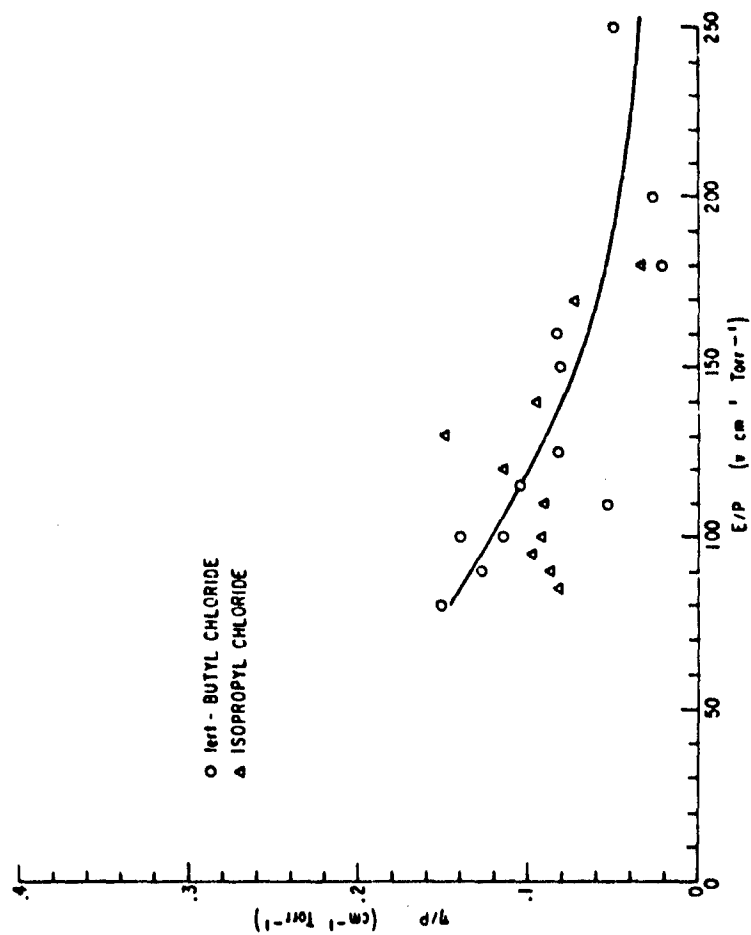


Figure I-37. Comparison of  $n/P$  for *t*-Butyl Chloride and Isopropyl Chloride

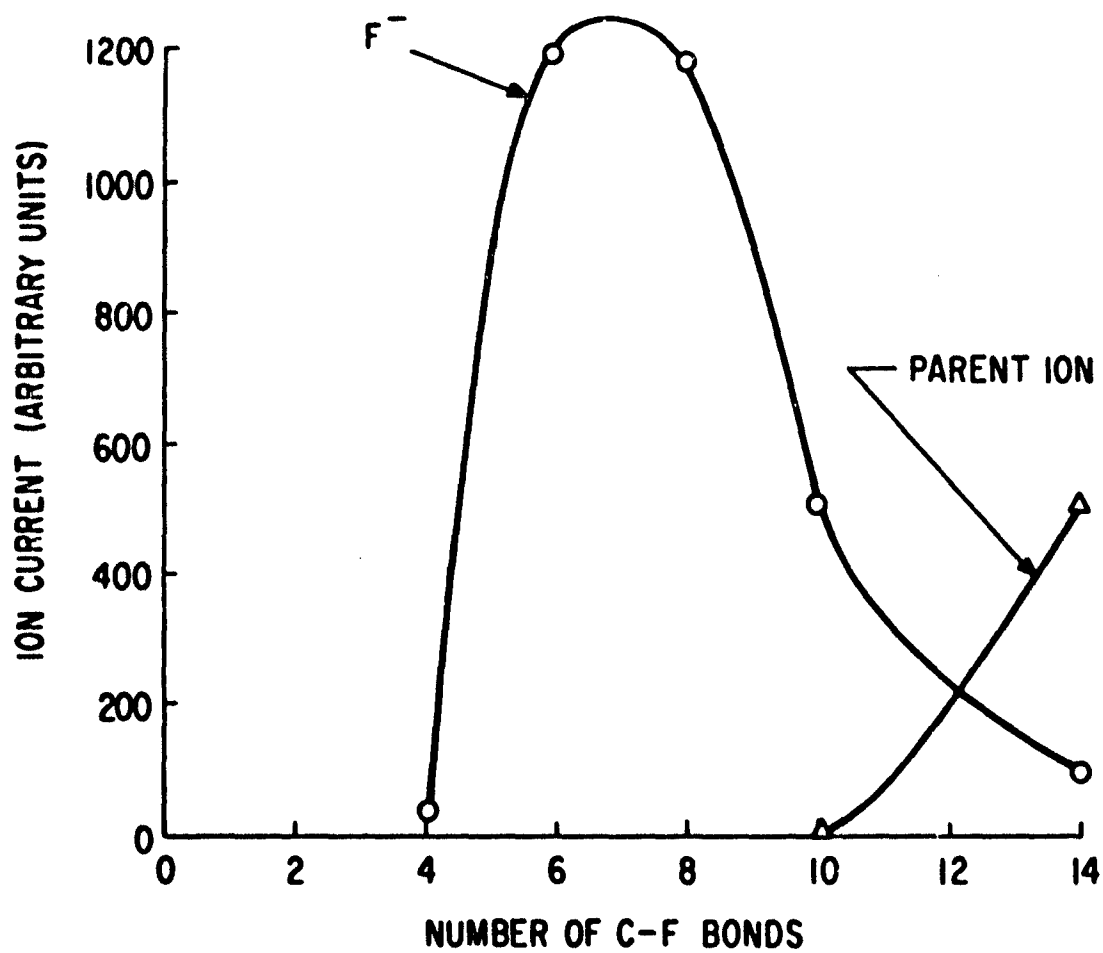


Figure I-38. Maximum Relative Cross Sections for Negative Ion Formation as a Function of Chain Length in the Perfluoroalkanes

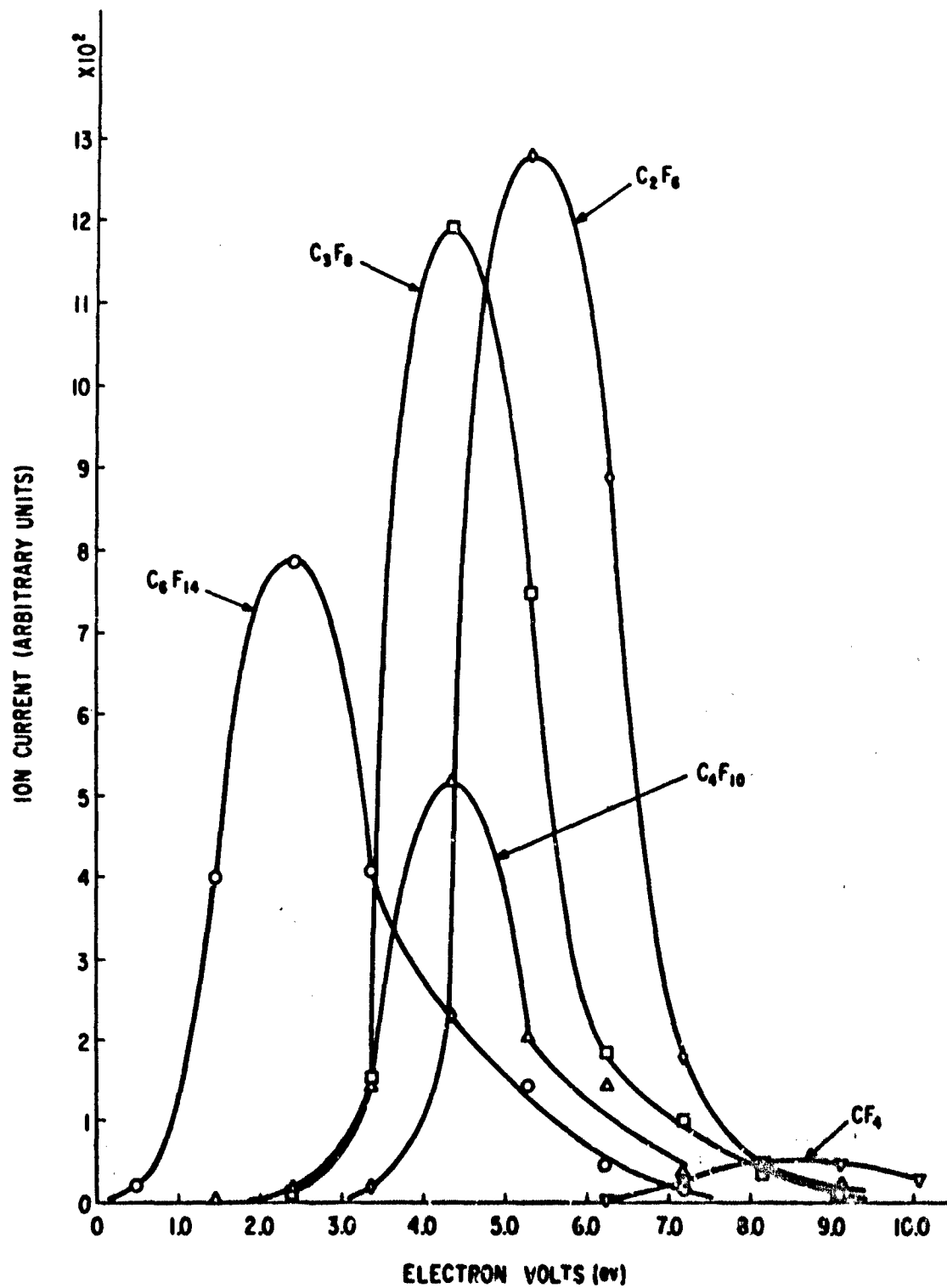


Figure I-39. Relative Cross Sections for Total Negative Ion Production as a Function of Electron Energy in the Perfluoroalkanes



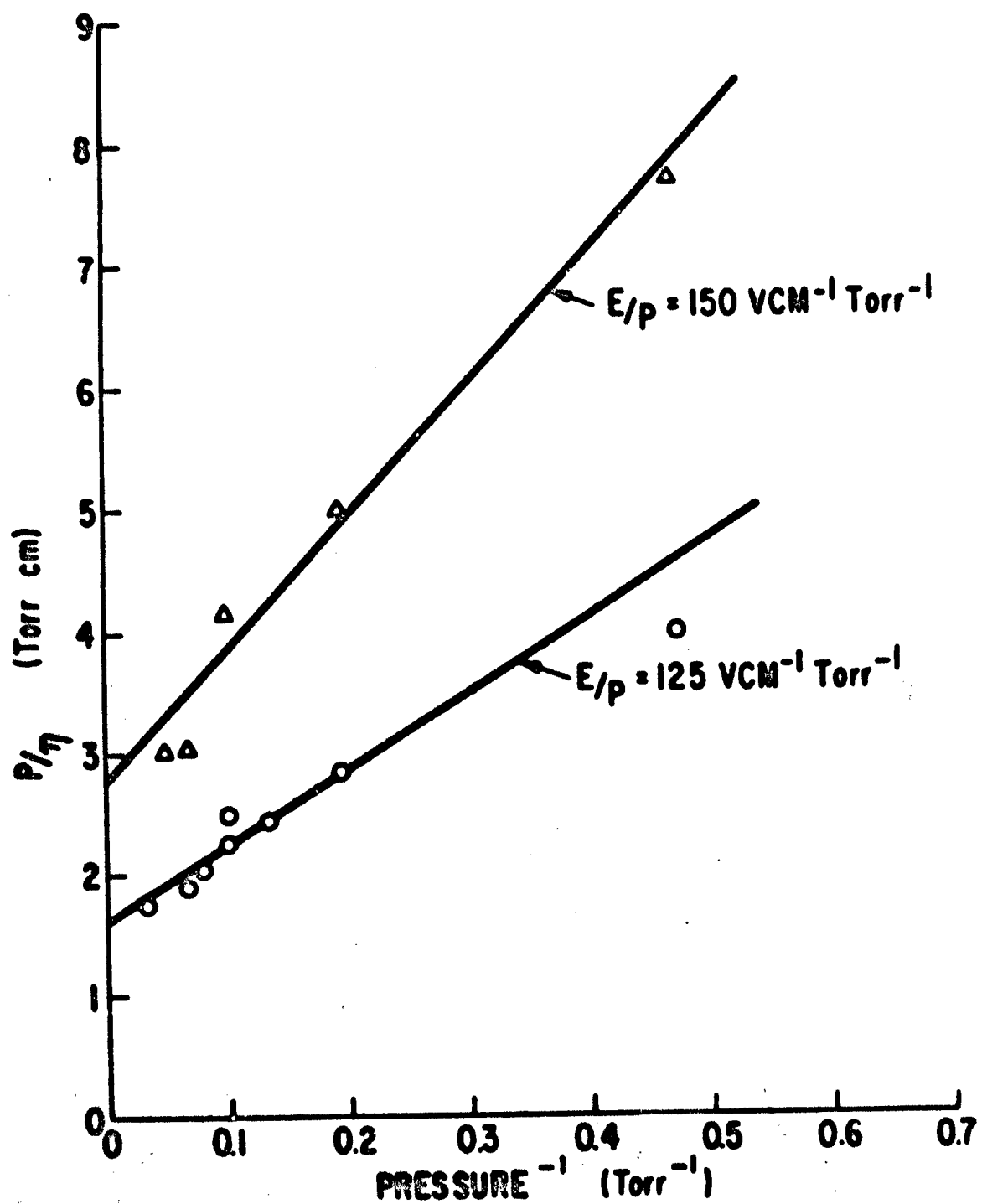


Figure I-40. Dependence According to Theory of  $\eta/P$  on  $P$  for  $C_4F_{10}$

## PHASE II. CHEMICAL EFFECTS OF CORONA ON MATERIALS

F.F. Carini, D.R. Johnston, and A. Pletenik

### A. STUDIES OF CORONA DAMAGE TO MATERIALS USING POSITIVE AND NEGATIVE D-C DISCHARGES

#### 1. Introduction

Corona damage to materials has been related to many different electrical parameters of the system with more or less agreement by a number of different investigators. Chief among these factors have been: applied voltage, frequency of applied potential, pulse size, and energy of the corona. Many of these parameters are interrelated so that it is not too surprising that if a relationship between damage and any one of these parameters obtains, corresponding relationships will exist between others of these parameters. As will be seen in Part B of this phase of the contract, this technique of associating damage with energy has a rather limited range of usefulness. This approach is particularly susceptible to error at the lower stresses--a condition commonly encountered under operating conditions.

Where a correlation between energy and efficiency of corona (rate of weight loss/corona energy) exists, one is inclined to think that the damaging species must be either ions or electrons. This is thought to be the case since the number of discharges per half-cycle will be proportional to the applied voltage above that required for corona onset. For a given gap, and, for a given pressure, the energy is also proportional to the excess applied potential. However, it is well known that most organic insulations show degradation products that are formed due to oxidation, i. e., carbonyl groups and acids. It is reasonable to assume, then, that physical erosion may not be the whole explanation for the mechanism of corona damage.

In addition to positive ionic and electronic bombardment and oxidation possibly due to ozone, other potentially damaging species exist. These species are: photons, negative ions, nitrogen oxides, and electronically excited states. In addition to these, one must also consider heating effects that may result from conduction of charge through a streamer to a very small point on the insulation. However, here as with all the other damaging species, there are some questions to be raised. Such a heating mechanism must generate very high temperatures, indeed, since Teflon has about the same order of magnitude of life as polyethylene, yet their temperature stabilities are much different at the more useful end of the temperature scale. Another pair to consider would be mica vs "H" film. As will be seen in this report, "H" film has about the same corona resistance as Mylar, yet

It is said to decompose somewhere above 700°C, whereas mica begins to decompose (lose its crystalline water) at about 550°C. The extraordinary corona resistance of mica is well known.

In addition to all the above-mentioned complications that beset the investigation of the mechanism of corona damage to materials, there is yet another complication. This is that there is more than one kind of silent discharge. In the previous report (ASD Technical Report No. 61-693), Devins described the Townsend-like discharge and the streamer discharge, and discussed how they were related to each other. The report also discussed what idealized shapes for these two kinds of pulses would be on an oscilloscope. These ideal shapes are seldom seen, however, and there is always some question as to whether other kinds of discharges should also be considered. Some pictures of such questionable pulses are shown in this section.

In light of the above discussion one can see what a formidable task it would be to separate all of these various effects from each other. Our approach in this part of Phase II was to concentrate particularly on separating bombardment of the insulation when the insulation was the anode from that bombardment when the insulation was the cathode. Clearly to do this one must go to d-c corona; since the number of discharges involved in d-c corona is much fewer per unit time than for a.c., this required some special techniques that will be discussed. In addition to this, we have looked at the differences between materials and differences due to different kinds of discharges. This section logically precedes Section B of Phase II in that we have relied on some of the discoveries in this section to explain some of the results obtained for weight loss experiments in Section B.

## 2. Experimental Method

The cell used is shown in Figure II-1. It consists of a variable air gap with a micrometer head. The top electrode is of stainless steel, 1 inch in diameter with a 1/16-inch radius. The bottom electrode was shaped to contain a 2 7/8-inch, 0.040-inch-thick glass plate, which itself was backed with silver paint to assure good electrical contact with the steel plate that holds it. Parallelism in the gap was assured by means of four adjustment screws on the top electrode; when they are parallel the gap can be closed and no light can be seen coming through regardless of which angle the gap is viewed through the cylindrical quartz section. The glass was cleaned with ammonium bifluoride and then rinsed with distilled water and further cleaned with "Tide" and rinsed for about 1/2 hour. It was then rinsed with ethanol and allowed to dry before application of the film to be studied. The dielectric constant of the glass was measured over a range from 10 cps to 45 Mc/sec and found to be constant at  $8.0 \pm 0.4$ . The capacity of the glass plate was 28.4 pf. The d-c resistivity of the glass was  $1.0 \times 10^{12}$  ohm-cm as measured with a Keithley electrometer at 100, 250, and 500 volts using painted silver electrodes. The time constant of this plate was 1 second.

This amount of discharge would not produce very much damage, so we have gone to applied potentials much higher than the sparking potential.

Another cell was also used in these experiments that differs from the one just described in two ways: (1) the parallelism of the cell is obtained by means of a ball-and-socket joint on the top electrode, and (2) instead of being surrounded by a cylindrical section of quartz it simply had a small (1/2-inch diameter) quartz window. In both cells, three capacitors of 500 pf each were placed between the high voltage and ground; thus giving 1500 pf capacitance across the cell. The dropping resistor in both cells was 160 ohms between the low potential electrode and ground. A schematic diagram of the circuit is shown in Figure II-2.

Other equipment used consisted of a Tektronix Type 531 oscilloscope with a 0.03  $\mu$ sec rise time. The d-c source was a Condenser Product 30 kv power supply. This supply has about a 1% stability and was adjustable in voltage by means of a Variac. It was found necessary to energize this power supply with a General Electric voltage stabilizing transformer. This was particularly important at voltages near the corona starting potential.

The counter used for the radioactive counting consisted of an Atomic Instrument Co. "Multiscales" Model 1228 timer unit together with the associated Model 1070A counter unit. The Geiger tube used was a Tracerlab Type TGC-2/1B84. The counter used for counting the number of discharges (from the corona) was a Berkeley Model 2105 decimal scaler. This was used in conjunction with the Tektronix oscilloscope. The "volt/cm" setting on this oscilloscope follows the trigger on the scope and was, therefore, used as a "gate" for discriminating the intensity of the corona discharge. Thus, the "gate out" signal of the scope was fed into the input of the Berkeley counter.

The dotriacontane ( $C_{32}H_{66}$ ) was obtained from Vold. This material was labeled with  $C^{14}$  at the 16 and 17 positions. As-received, it had an activity of 500  $\mu$ C; this was diluted by us to 25.5 mg of the material with 250 ml of benzene. The eicosane ( $C_{20}H_{42}$ ) was diluted to 0.03 gram of radioactive material with an activity of 1 mC/mmole with 0.4 gram of normal eicosane in 50 ml of benzene. The stearyl alcohol was received with an activity of 500  $\mu$ C and was mixed with nonradioactive stearyl alcohol to form a 1/2% solution in benzene.

After some trial-and-error attempts in applying these materials to the glass plate, it was finally discovered that the best way of obtaining a smooth coating was to place a few drops of the solution on the plate and to buff it with the smooth side of a piece of chamois. Attempts to make a thin layer by solvent evaporation resulted in small islands of crystalline material.

The first step is to consider the magnitude of the effect that one might expect from such an experimental arrangement of Figure II-2. In Townsend-like discharge, Devins<sup>(1)</sup> has shown that at about 10 volts overvoltage the pulse magnitude was about  $2.0 (10)^{-9}$  coulombs or  $1.2 \times 10^{10}$  charges; see Figure II-3. A  $\text{CH}_2$  group has an area of about  $10^{-15} \text{ cm}^2$ . Since the area under the electrode is about  $4.5 \text{ cm}^2$ , there are  $4 (10)^{15}$   $\text{CH}_2$  groups on the surface covered with a monomolecular layer of hydrocarbon. Assuming 100% efficiency of the radiation, it would take  $4 (10)^5$  pulses (5 days at a pulse rate of 1/sec) for all the  $\text{CH}_2$  groups to be acted upon. If there are  $n$   $\text{CH}_2$  groups per molecule, the time required for each molecule to react would be reduced by  $n$ .

These order of magnitude calculations indicate that it is important to use a technique that is sensitive to small changes in properties. Radiotracers appeared to give the needed sensitivity and provided a means for rapid quantitative analysis. Because damage from low-energy discharges should be confined to molecules close to the surface, it is necessary to use thin layers of organic materials so that a large fraction of the material is changed.

At the beginning of the contract it was decided to do these experiments on eicosane ( $\text{C}_{20}\text{H}_{42}$ ) and dotriacontane ( $\text{C}_{32}\text{H}_{66}$ ). Some delay was experienced in obtaining these as radioactive materials and some radioactive stearyl alcohol, which was on hand, was used for the preliminary experiments.

### 3. Results

#### 3.1 Stearyl Alcohol and Eicosane

The glass plate with thin layer of stearyl alcohol was then placed in the corona cell with a 0.22-mm air gap and a voltage of 1430 volts imposed across the cell. The radioactivity of the stearyl alcohol was followed as a function of time as shown in Figure II-4. The stearyl alcohol was on the negative electrode and, therefore, was bombarded with the positive ions of the discharge. The gap was irradiated by ultraviolet light to insure that the discharges would be Townsend-like.

For the eicosane experiments, it was found that all of the discharges were Townsend-like for this applied voltage and this gap setting even without ultraviolet light, and illumination was therefore not used. The eicosane solution consisted of 0.4 gram of normal eicosane and 0.03 gram of radioactive eicosane, tagged on the end carbon, in 50 ml of benzene. The activity of tagged eicosane was 1 mC/mole. The results for the eicosane are shown in Figure II-6 and in Table II-1. During the exposure of stearyl alcohol, it was not possible to run the d-c power supply overnight because of voltage fluctuations; by the time the eicosane was run, a voltage-stabilizing transformer was obtained that allowed continuous operation.

The data for streamer discharges on stearyl alcohol are shown in Figure II-5. The condition for these discharges was a 30-mil gap and 7.35 kv. The apparent damage done on a net count basis is about the same for positive bombardment with Townsend discharge (see Figure II-4) as for either positive or negative bombardment with streamerlike discharges. Later on we shall have more to say about the extent to which we really can discriminate between Townsend and streamer discharges as a function of time. We shall also compare these data on stearyl alcohol with data for eicosane and dotriacontane. For the present, it will suffice to comment that the technique described above worked very well for eicosane and dotriacontane, but not very well for the stearyl alcohol; with the latter, there was still a lot of clumping, and small crystals were visible on the surface. It is possible that an occasional streamer during the Townsend discharge condition could have knocked a small crystal over to one side. In any case, the condition of the surface for the experiments with the stearyl alcohol does obscure the results.

An early run of Townsend-like corona damage on eicosane is shown in Figure II-6; the detailed conditions and counts are shown in Table II-1. From this table the reader can see what the authors found out very soon, namely, that the eicosane has a sufficiently high vapor pressure to sublime from the plate at about the rate that any damage due to corona discharges takes place.

Having made this observation, three more samples were run; one of these was a control and the other two were bombarded with positive and negative species, respectively, without undue exposure to noncorona conditions. These data are shown in Figures II-7 and II-8 and the same data together with some longer time data are shown in Table II-2. Some justification for showing these data plotted as per cent loss and also absolute loss per unit time is shown in Figure II-9. This generally accepted picture of how this kind of material deposits<sup>(2, 3)</sup> shows that an ion could go through a first layer and strike a molecule in the second layer or as the piles get larger at the base the area exposed to damaging species increases. The point here is that for films of the order of monolayer coverage, the efficiency of the discharge is some function of the amount of material that is present to be damaged. In this sense, then, it is appropriate to consider damage as a per cent of the material present to begin with. However, since there is only a certain number of discharges per unit time and since each of these is only capable of so much damage, there is also a reason why one should expect a constant amount of damage in terms of counts per minute for a given time of exposure; hence Figure II-8. This latter expression of damage rate does pertain to Mylar, "H" film and other materials. With films of the order of one monolayer, however, it is not quite right to think of it either way.

In these data on the damage done on positive vs negative bombardment, the reader can readily see that whether one takes the view that damage should be linear with time or linear per cent with time that the ion bombardment is

more damaging than the electron bombardment. The electrons are accelerated across the gap without losing much kinetic energy on each collision, whereas the ions lose much of their kinetic energy on each collision before arriving at the surface. However, the ions arrive not only as ions but with a variety of charged states. It may be this "potential" energy that causes the damage.

One other comment on the eicosane results is in order. During the counting process, the background measurements showed an increase from 30 to 70 counts/min and stayed around this value; this was presumably due to the volatile eicosane and perhaps lower molecular weight materials being deposited inside the lead shield. Gradually, as experiments with dotriacontane were begun, this background fell to a more conventional level.

### 3.2 Townsend-like Discharge on Dotriacontane

The same voltage and gap used in the eicosane and stearyl alcohol experiments with Townsend-like discharges (1.48 kv at 9 mils) were used with a thin dotriacontane film. This 32-carbon-atom hydrocarbon was dissolved in benzene as described in the Experimental section. The sublimation rate of dotriacontane is negligible within our experimental limits for exposures of 20 days.

Table II-3 shows that the radioactive count increased by 15% when the film was cathodic as compared to no appreciable change for the anodic bombardment. This appears to be quite different from the case of eicosane, but the position of the radioactivity in the molecule is changed. The dotriacontane is labeled at the 16- and 17-carbon atoms, that is, at the center of the molecule; whereas the eicosane is labeled at the 1-position at the end of the molecule. Therefore, even though the dotriacontane might have been losing end groups, no change in radioactivity would have occurred.

The increase in count is somewhat surprising; however, if the molecules within the film are packed as shown in Figure II-9 some surface diffusion can be expected to occur. It is well known that liquid films in a configuration such as this will be drawn into the region of high field since the energy of the system is reduced by replacing the air by higher dielectric constant material. Such a phenomenon might possibly explain the increased count we observe with dotriacontane if, in addition, we assume that positive ion bombardment is causing a decrease in viscosity.

On the average, the film thickness in these experiments was about 150 Å. The sample exposed to positive ions was measured for smoothness of the film on the glass plate. The method used was an interferometric attachment on a microscope at a magnification of 156X. It was found to be smooth within 100 Å. Therefore, the increase in radioactivity is not due to clumping of the material.

### 3.3 Streamerlike Discharge on Dotriacontane

The over-all effects of Townsend discharge on the organic materials have been relatively small. As will be shown, streamerlike discharges have a much more profound effect on the dotriacontane. Attack by both positive and negative species resulted in decreasing the radioactivity of the plates. Furthermore, we shall see that the electrode systems and gas phase exert a profound effect on the type of discharge and, therefore, on rate of damage to the organic layer.

The results will be given in the order that the experiments were performed to emphasize the changing character of the discharges. At the start only one cell was used; therefore, the films were exposed as cathode and anode consecutively. The gap was set at 15 mils and voltage at 7.3 kv, at which point the oscilloscope trace indicated streamerlike discharge as shown in Figure II-22. A large number of energetic Townsend discharges were also noted. The cell (Figure II-1) was open to the atmosphere through the two glass tubes. Therefore, the gases in the enclosure and those produced by the discharge were virtually stagnant.

The decrease in radioactivity is given in Table II-4 and Figure II-10. The radioactivity of the film subjected to positive ion attack remained relatively constant for quite a period of time before decreasing to a low level. Conversely, the film that was anodic decreased rapidly at the start and the rate of removal decreased considerably after 1025 minutes.

The short-time plateau of the cathodic run is somewhat similar to the Townsend-like discharge that showed an increase in count. Apparently in this case, there is a tying up of mobile molecules, which diffuse into the area of high field. However, after a period of time the molecules are degraded and are removed from the plate.

While the anodic discharges were being run, the glass plate was noted to have a spotted appearance in the discharge area. Subsequent to the discharges, an analysis of these spots (Figure II-11) was made. The darkened spot in Figure II-11 is actually a mound of material about 1 micron in height. The original dotriacontane film thickness on this plate was about 30 Å. The material was mainly lead nitrate. The nitrate was probably a product of the discharge in air that filled the cell. The glass plate was analyzed and found to have small amounts of lead present.

Typical Lichtenberg figures were also observed, which one associates with streamerlike discharge. In addition to these characteristics, the silver paint backing of the glass slide was darkened; this effect was not observed on the ion-bombarded sample.

In analyzing the spots, first an attempt was made to dissolve the material in carbon disulfide (a solvent for dotriacontane). However, the spots did not



dissolve in the carbon disulfide and also the solution was nonradioactive. The spots were then scraped and rubbed with KBr, and a pellet 4 1/2 mm long by 0.75 mm wide was made for infrared analysis. This was run in the beam condenser using Baird Model 455 double-beam spectrophotometer. Four major peaks were found. Two peaks at 7.25 $\mu$  and 11.95 $\mu$  are due to an inorganic nitrate; one at 6.15 $\mu$  is due to water and a peak at 12.83 $\mu$  was unidentified. X-ray diffraction and x-ray fluorescence were used to identify the material as lead nitrate. An emission spectrographic analysis of the glass showed that lead was present in the glass. Therefore, the reaction is between the nitrate formed in the streamer from oxygen and nitrogen present in air and the lead from the glass.

Since the plateau of the ion-bombarded sample was similar to the results of the Townsend discharges, the gap was increased to 30 mils. Although this should maximize the chances for streamers, no increase of these was noted.

Another cell was set up so that the cathodic and anodic bombardments could be run simultaneously. The results of these corona discharges are shown in Table II-5 and Figure II-12. Again the cells were open to the atmosphere through narrow tubes; therefore, the atmosphere was stagnant. Although deposits were formed with the 30-mil gaps used here, they were much less prominent than had occurred when the gap setting was 15 mils.

The only change noted was that the radioactive count plateau at the beginning, on the ion-bombarded film, was shorter than on the narrower gap. The results shown in Figure II-12 lead to the observation that both anodic and cathodic films are disappearing at the same rate. However, the character of the discharges was found to be changing on the two cells.

The anodic cell discharges appeared to be relatively stable with time. Conversely, the cathodic cell was undergoing a radical increase in Townsend-like discharges at the expense of the streamers.

All of these earlier runs were carried out in the cell open to the atmosphere but with no gas flow. When it was discovered that the streamers were converting to Townsend-like discharges as shown in Figure II-13, air dried with Drierite was passed through the cell with resultant increase in the streamerlike discharges. The run using nonradioactive DTC (dotriacontane) did not degenerate into Townsend discharges under these static conditions. At this time only the cells in which the film was the cathode appeared to degenerate. The second cell with the film as the anode maintained its streamerlike character. From this it appeared that the radioactive decay would yield enough electrons to inhibit the formation of streamers. The nonradioactive DTC was applied in exactly the same manner as the radioactivity tagged film. Four drops of solution composed of 275 mg of DTC in 250-ml benzene was buffed onto the plate.

A flow of gas through the cell apparently swept away the gaseous fragments containing the radioactivity so that the decay would not affect the discharge area. However, even though the cells were swept by air or nitrogen, there was a decrease in the number of discharges per unit time of lower magnitude. The number of largest discharges increased.

Flowing air through the system resulted in a better maintenance of streamer conditions and the results are shown in Table II-6 and Figure II-14. The two cells were used, so that the runs were made simultaneously. The rate of loss of radioactivity is slightly greater under conditions of positive bombardment than for negative bombardment.

The run under stagnant conditions showed a loss of count of 32 counts/min after 1200 minutes whereas in the flowing system the decrease was 53 counts/min. This is partly due to radioactive gases being swept out of the high field area. Another improvement caused by the flowing gas was the elimination of the deposits in the other cell under negative bombardment. Apparently, the nitrogen oxides are swept from the cell before they react with the lead in the glass.

The film under negative bombardment showed a decrease of radioactivity 34 counts/min after 1200 minutes of exposure. This compares quite closely with the loss of 36 counts/min of the cell run under static conditions as shown in Table II-5.

The rate of discharges of each cell was monitored during the runs with flowing air. The results are tabulated in Table II-7. These are by no means the total count, but just those over 0.5 volt/cm. Considerable variations were noted, but no specific trend was detected other than that fewer discharges occur in the cell in which positive bombardment is taking place.

The same type of experiments was repeated using flowing nitrogen rather than air. The results are tabulated in Table II-8 and in Figure II-15. Here the rate of reaction for positive bombardment is about twice that of the negative. About 37 counts/min were lost in 1200 minutes compared to 19 counts/min for the negative bombardment.

The decreased reactivity in the anodic cell may be due to the inability of nitrogen to form negative ions. In air, conversely, oxygen is capable of forming negative ions. Over-all, both cathodic and anodic attack were less in the nitrogen, which is reasonable since that part of the decomposition due to oxidation is minimized.

Figure II-16 shows that the rate of discharges was found to decrease as the aging progressed. This figure also shows that the number of discharges was less in the cathodic cell than in the anodic.

In the course of the above discussion we have raised many questions about the nature of the discharge and connection this may have with damage to the material. One of the most interesting observations has been the transition of the discharges from streamers to Townsend-like pulses, and we shall next discuss possible reasons for this.

It is not clear at this time why this transition should occur. Since we start with an uncharged plate, the initial streamers could only serve to increase the nonuniformity of the field that would tend to favor more streamers. Any increase in the conductivity of the plate would lead to a decrease in the time constant of the plate that would favor a faster rise in the voltage following a discharge, thus providing the next discharge with a higher over-voltage; this should also favor streamerlike discharges.

Another interesting aspect of the changing nature of the discharge is that the conditioned plate can be returned to the starting condition much more rapidly than it can be conditioned. For example, a conditioned plate having 43.3 pulses/sec at a gate setting of 0.2 volt/cm was left in the cell and the voltage turned off for 1 minute. The voltage was then turned on again and the rate was found to have dropped to 18 counts/sec. The plate was then allowed to remain this way for about an hour. At this time the pulse rate had climbed to 36 counts/min. The voltage was once again turned off, this time for 10 minutes, and then on again. The following shows the rate of conditioning after this procedure.

Before turning voltage off	Pulse rate 36 (counts/min)
Voltage off 10 minutes	--
On 1 minute	10
On 4 minutes	17, 13, 15
On 30 minutes	27, 18, 24
On 120 minutes	24, 25

One possible explanation for this effect is as follows: as the streamers strike a surface, the positive charge goes out in "fingers" from the strike spot. Thus after awhile the area under the plus electrode will have a ring of positive charge there that is limited to some steady-state value by the resistivity of the plate. It may be that this positive charge eventually lowers the effective voltage across the gap. The result would be that voltage rise time after a discharge would not be longer and the overvoltage would be smaller; this would favor Townsend-like discharges.

If we attempt to explain this changeover from streamers to Townsend-like discharges by interpreting changes in  $\gamma$  (the second Townsend coefficient), the resulting explanation is not in the right direction. Thus, if we say that the surface conductivity of the plate becomes greater and that, because of this, electrons are more available to add to the avalanches that go toward creating a critical number of avalanches needed for the transition from

Townsend to streamer breakdown, then we see that with time the streamer discharges should predominate.\*

One other explanation seems likely, and that is that the electrons produced in the beta disintegration of carbon -14 can act as initiating electrons for the discharge process, thus causing the time lag on the voltage rise to be shorter; hence the overvoltage to be smaller. As a result of this, the discharges would tend to become more Townsend-like in character. (For more details of this argument, see Reference 1.)

An order of magnitude calculation makes this seem not unreasonable. We have a net count of about 100 disintegrations/min as counted by the Geiger tube assembly. Some of the radiation could be masked by the layers of material on top of the bottom-most layers of radioactive material. Carbon -14 is a very weak emitter and even small amounts of water on top of a layer of the material will attenuate the counts received at the tube, as we have mentioned previously. Considering this effect together with the possibility that the amount of carbon -14 in the gap may increase with time, due to formation of  $\text{CO}_2$  and low molecular weight fragments together with the fact that the efficiency of the tube is about 30%, it is not unreasonable to suggest that the disintegrations per minute in the gap may be of the order of 1000 counts/min. This would be of the order of 16 electrons/sec, which is about enough change in the number of initiating electrons to account for the effect of the changing nature of the discharge. Indeed, when a plate of nonradioactive material was placed in the cell with the same voltage and gap setting, a difference in the kind of discharge (as a function of time) was noted. It is felt that a change of streamer to Townsend-like discharges could be partly accounted for in this way.

It is also interesting to speculate as to why there should be more discharges in air corona than in nitrogen corona. Referring to the above discussion of the changing character of the discharges, we note again that a conducting surface is more inclined toward the production of Townsend discharges. Then more discharges would be expected in air corona if one agrees that (1) an air corona results in a more conducting surface than a nitrogen corona; (2) that conductivity of a surface may mean availability of electrons and, hence, decreased time lag before breakdown; and finally (3) that the amount of charge per unit time will be determined by the time constant of the plate and will be roughly a constant.

---

\*However, one could just as easily argue that the increased conductivity of the surface increased the availability of the initiating electrons and, hence, lowers the time lag and the required overvoltage; this would favor the Townsend-like discharges. Other information on this will be discussed in the paragraphs to follow.

We have seen differences in the rate of damage due to ion bombardment vs negative bombardment. Some of the reasons for this have been discussed. In the course of this investigation, however, it became clear that there is still another complicating factor in addition to those we have already mentioned. Figure II-17 shows the difference between the cell running with ion bombardment vs the cell running with electron bombardment. The time scale has been compressed to show particularly the greater number of tall peaks (ion bombardment) that we feel are indicative of the number of streamers as against the small rounded discharges (electron bombardment) that are probably Townsend-like. Many pictures of this kind convinced the authors that there was a significant difference between the two cells. Figures II-18 and II-19, showing ion and electron bombardment, respectively, are exhibited as supporting evidence for the difference in the character of the discharges. In all of these cases, and for the following oscillograms, air was blowing through both cells.

As a result of this finding it was decided to wire both cells for ion bombardment of the sample; the result is shown in Figure II-20. With both cells connected for negative bombardment of the plate, the result is as shown in Figure II-21. One can only conclude that the distribution of streamers vs Townsend discharges is, among other things, a function of whether the cathode is metallic or not. With the cathode metallic, the distribution favors Townsend discharges and vice versa.

This effect may be due to the difference in densities of glass and metal and hence their differing capabilities for stopping a cosmic ray to make electrons that initiate the avalanches. The same argument that was used before may also apply here, i. e., that the higher conductivity could be a reflection of the ease with which electrons can be initiated. In either case, more initiating electrons mean lower overvoltages and hence more Townsend-like discharges.

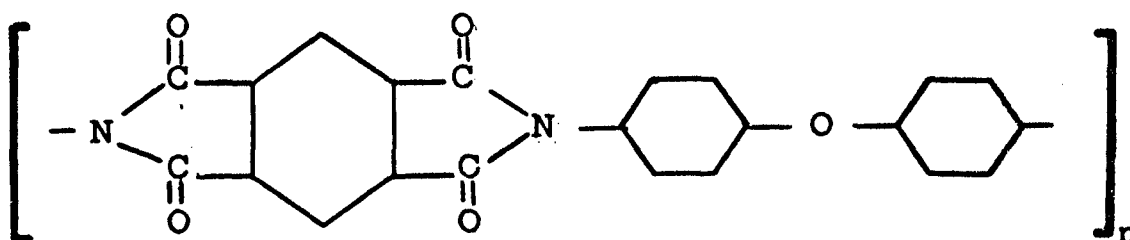
Figure II-22 shows the discharges in the two cells with increased sensitivity and a faster sweep on the oscilloscope. Here again, one can see, for every picture, a difference between the number of large discharges between the positive and negative bombardment. These pictures are shown principally to draw attention to the details of these discharges that we have been calling streamers. Our reluctance to call these discharges streamers is also shared by Park and Cones. <sup>(4)</sup> Their oscillographs of ball-to-plate discharges in some respects look like some we have obtained. In particular, they distinguish between a first and second discharge pip; we have many pictures showing a sort of camel's hump in the current vs time oscillographs. Admittedly, our gaps are much shorter than theirs, but it is still of interest to note this similarity.

## B. CORONA EFFECTS IN COAXIAL CORONA CELLS

### 1. Introduction

Research in this section is more or less a continuation of work that was reported in Ref 1 on effects on films of materials exposed to corona in coaxial corona cells. Some of this work is a continuation of corona damage to Mylar and the remainder of it concerns corona damage to "H" film, at the request of ASD.

"H" film is a polyimide of pyromellitic dianhydride and oxydianiline. Structurally this polymer is



Since this polymer is noted for its resistance to chemical and physical changes through various degrees of heat aging, i. e., it is truly a class H insulation system, it was decided that this would be an ideal material with which to explore corona damage to organic insulating materials with various pressures, temperatures, and corona energy distributions.

We have already discussed the idea that energy of the discharge is linearly related to damage done. In this section we shall show that this is not so, at least not for weight loss experiments over a wide variety of pressure, voltage, and temperature.

### 2. Experimental

The coaxial cell was selected as a convenient type of cell for evaluating the degradation of materials subjected to controlled corona conditions. Referring to Figure II-23, it consists of two concentric Pyrex glass cylinders separated by an air gap of 125 mils. Voltage applied to the platinum electrodes, placed on the outside of the outer cylinder and the inside of the inner cylinder, causes electrical breakdown of the enclosed air gap. Materials to be evaluated are placed in the air gap by wrapping them around the outside of the inner cylinder. Care was taken to cut the tapes (of the films to be tested) on a bias at both ends in such a way that the right circular cylindrical electrode was completely covered and so that none of the film extended beyond the electrode.

### 3. Discussion of Results

Figures II-24, II-25, and II-26 show the results of weight loss measurements on Mylar. Figure II-25 is from the previous contract period. (3) Clearly, the points now confirm that the "activation energy" is 4.7 kcal/mole (see Figure II-27) and is nearly voltage independent. Cooper and Prober (5) have suggested that in the discharge area, the oxidation of polyethylene is balanced by volatilization at the surface; they also point out that weight loss in the nondischarge area reaches a plateau after a short time. Taking these facts together with the above-mentioned weight loss results, one could conclude that the rate determining step in the discharge may very well be the step at which the low molecular weight fragments,  $\text{CO}_2$ , or water either volatilize or are knocked off the surface by bombardment from the discharge.

With this explanation, however, it would be difficult to explain why the positive bombardment with nitrogen on dotriacontane should be nearly the same as that for positive bombardment in air. Meats and Starnett (6) have shown, using an artificial void and monitoring the pressure change in the void, that many different gases behave about the same. We would rather say that damage to materials by streamer discharges is more of a momentum effect and that it has very little meaning to talk about an activation energy.

At the time we began this work on "H" film it was decided to do some of the experiments we had originally intended to do with Mylar with the "H" film instead. The initial work consisted of mapping out the energy spectrum of the coaxial corona generators wrapped with "H" film.

Energy measurements were made with this system in the same manner by which energy measurements were made on the Mylar system (1) ASD Report No. 61-693. By the use of this technique, the charge transferred across the cell is determined by the voltage drop across a series external capacitor from the low-voltage side of the cell to ground. This charge produces a parallelogram when it is plotted against the voltage across the cell on an oscilloscope. The area of the resulting parallelogram is proportional to the energy of the corona discharge.

The results of the measurements of corona energy, as a function of pressure, temperature, and voltage, are seen in Figures II-28 through II-31. At room temperature,  $24^\circ\text{C}$ , the resulting graph of applied voltage against energy indicates a proportionality between the two at all pressures that were measured. At  $70^\circ\text{C}$  the data show some deviation from proportionality, and at  $98^\circ$  and  $120^\circ\text{C}$  the deviation is clearly outside of experimental error. Since the deviation from the expected straight line is so apparent, some justification of experimental procedure is in order. The Tektronix oscilloscope was checked for accuracy of the calibration. The pressure was maintained by means of a Matheson vacuum pressure regulator. The pressure was measured by means of a diaphragm type pressure indicator, which had

been calibrated against a mercury manometer and found to be accurate to within 1% of full scale (760 mm). The voltage was measured with an electrostatic voltmeter, which had also been calibrated recently.

In this regard it was of interest to us to observe the values of  $E_0$ , which is supposedly constant according to Manley. <sup>(7)</sup> The values of  $E_0$  as a function of pressure, temperature, and voltage are given in Table II-9. Here we see that  $E_0$  varies considerably with voltage for a given set of conditions of pressure and temperature. According to Manley's theory, the energy of the corona is given by

$$W = 4f C_g E_0 [E_m - (1 + C_a/C_g) E_0],$$

where  $W$  = energy of the corona

$f$  = frequency

$C$  = the capacitance of the glass in series

$E_0$  = the voltage from the midpoint of the parallelogram to the edge, i. e., the average voltage across the gap during the discharges

$E_m$  = peak voltage

$C_a$  = capacitance of the air gap without discharge.

Clearly, the variation in values of  $E_0$  that we have observed might explain the nonlinearity of the energies ( $W$ ) that are plotted in Figures II-28 through II-31. Why the deviation from proportionality between energy and voltage should be more severe at the higher temperature is not known at this time.

Devins <sup>(8)</sup> has explained the deviation of  $E_0$  and  $V_s$  as being due to the charge distribution. According to this theory,

$$E_0 = V_s - \frac{\delta\sigma_a}{2C_a},$$

where  $V_s$  is the sparking potential and  $\delta\sigma_a = \delta\sigma_a (\text{max}) - \delta\sigma_a (\text{min})$  where  $\delta\sigma_a (\text{max})$  is the maximum and  $\delta\sigma_a (\text{min})$  is the minimum charge density in the air gap.

Tables II-9 and II-10 show the following with regard to changes in  $\delta\sigma_a$  as a function of the operating parameters. (1) A decrease in  $V_0$ , the amplitude of the applied voltage, causes a decrease in  $E_0$  and hence an increase in  $\delta\sigma_a$  with decreasing  $V_0$ . (2) An increase in temperature at constant pressure and  $V_0$  causes an increase in  $\delta\sigma_a$ . (3) An increase in  $P$ , with  $V_0$  and  $T$  being constant, causes an increase in  $\delta\sigma_a$ .

The first and third observations above can be explained on the basis of the distance between the  $\theta_s$  (the angle of the applied wave where corona begins) and  $\pi/2$  (the angle of the wave where corona is extinguished). Thus, the larger the distance between these two angles, the more the discharge will occur on the steeply rising portion of the curve where, statistical time lag being a constant, the overvoltage for each pulse will be greater and they



will tend to be streamerlike, which would favor a large value for  $\delta\sigma_a$ . The second observation mentioned in the above paragraph could probably best be explained by noting that  $\alpha$  and  $\gamma$  vary in such a way that the efficiency of the overvoltage may be changed in such a way that, at higher temperatures, lower overvoltages could result in the transition from Townsend to streamerlike corona. Certainly,  $V_g$  as measured in this way, i. e., by extrapolating to energy/cycle equals zero, gives values of  $V_g$  that are in the opposite direction from those one would expect from the usual Paschen's Law.

The experimental values of weight loss of "H" film as a function of time for various conditions of pressure and temperature are shown in Figures II-32 through II-36. The rates are summarized in Table II-11. The temperature, pressures, and voltage were determined in large part by the facilities available. An interesting sequence in the change of the efficiency of the corona discharge from one temperature to another is seen in Table II-12. The energy is a function of how many ions or electrons are bombarding the material placed in the gap. Since corona energy cannot simply be related to weight loss, one would conclude that damage done by streamerlike corona is considerably more complicated than ionic or electronic bombardment. Figure II-36 is more complicated as we had one cell in which the air was shut off to begin with and later turned on. We will have more to say about this in the concluding remarks in this section.

Infrared investigation of the corona-damaged surface of "H" film showed no definitive spectral differences. Slight differences in the unexposed film that are noted can hardly be considered meaningful on the basis of one sample. The sample shows a weak absorption due to amide groups, but this peak is not always apparent even in "H" film unexposed to corona.

Weight loss rate measurements at various temperatures for various pressures are plotted in Figure II-37. No significant differences are noted between the activation energy for "H" film damaged by corona at two different pressures: 200 and 760 mm. As was previously noted, no differences in apparent activation energy were seen for three different voltage levels using Mylar as a sample.

Figures II-38 and II-39 show the effect of corona damage to the surface of "H" film. The pits formed are very small and uniform. No evidence of any compound or crystalline material is seen. Both of these results are in agreement with the infrared results.

One can see that the concept of linearity between damage done to materials and energy of the corona must be modified considerably. Pressure, temperature, and whether or not it is a flowing system, all drastically influence the damage done by the available energy. In particular, Figure II-36, which shows the effects of passing air vs a stagnant system, is remarkable. Upon a more careful look at this system, using an oscilloscope, it was

found that very soon after the air is shut off, the nature of the discharge is changed markedly from streamerlike to Townsend-like in character. This is consistent with behavior in the parallel plate cells, but here can be accounted for by a different reason. Namely, the conductivity of the surface becomes high enough so that charge that is deposited during one-half of the cycle can be conducted away so that it does not distort the field during the next half of the cycle; thus Townsend discharges are favored relative to streamers. These observations and the concurring observations made in Part A of this phase of the report point to a very important aspect of corona damage.

#### 4. Life Tests on Insulation Systems

A series of corona life tests was made on a variety of insulating materials to provide data of interest in practical insulating system design. To determine the relative lives of several materials under a-c corona attack, in a reasonable time, an accelerated life test with an applied voltage of 2.5 kv rms at 3000 cps was employed in a cell having point-to-plane electrode geometry. This geometry also simulates a detrimental condition that often leads to insulation failure in practical applications.

The data in Table II-13 were obtained using a needle-point electrode spaced 0.015 inch above the surface of the sample material with a flat-plate electrode in contact with the sample's opposite surface. Sample thickness in each case was 0.030 inch except for mica, which was 0.005 inch. The data in Table II-13 were obtained by exposing the samples to corona attack in air at atmospheric pressure at 105°C until breakdown of the solid insulation occurred. Relative life values given are based on the life of Mylar, which was 20 hours. In the case of mica and the silicone rubber, sample breakdown had not occurred after a relative life far in excess of the other samples tested. The tests on these two samples were terminated before failure.

In addition to showing the relative differences in corona life for different solid insulating materials, an experiment was performed to demonstrate the relative life of one material, Mylar, with two different ambient gases. The electrode arrangement, serving as a representative system, was a point-to-plane geometry similar to the one previously described. The needle-point electrode had a radius of 0.005 inch and was positioned 0.012 inch above the Mylar surface. An applied voltage of 1.8 kv rms at 3000 cps was used. Tests on three samples were run in air and in a high electric strength electronegative gas, Freon-12 ( $\text{CCl}_2\text{F}_2$ ). The latter is a high-strength gas by virtue of its ability to form negative ions and thereby act as a "sink" for electrons that would otherwise participate in field intensified collisional ionization leading to corona.

Failure occurred in the Mylar samples run in air after 5.1, 5.1, and 5.2 hours. Mylar samples similarly tested in Freon-12, at approximately 17 lb absolute pressure, showed no sign of damage after 90 hours of exposure, at which time tests were terminated. The high-strength electronegative gas has suppressed corona that causes failure of the Mylar in an air environment.

## **5. Conclusions**

By the use of d-c discharges on thin films of radioactive polyethylene-type materials, it was concluded that:

1. Ion bombardment is somewhat more damaging than negative bombardment; there is also evidence that negative ion bombardment is as damaging as positive ion bombardment.
2. Streamer-type discharges are much more damaging than Townsend-like discharges.
3. The nature of the discharge can be changed depending on whether or not the cathode is metallic or nonmetallic and also can be changed by the conductivity of glass plate that is being bombarded in this d-c corona.

## REFERENCES

1. "Research and Development on Corona Resistant Materials" ASD Technical Rept. No. 61-693 (March 1962).
2. H. Ries, J. Phys. Chem., S-2, 94 (1955).
3. H. Ries, Sci. Am. (March 1961).
4. J.H. Park and H.N. Cones, J. Res. Natl. Bur. Std., 56, 201 (1956).
5. G.D. Cooper and M. Prober, J. Polymer Sci., 44, 397 (1960).
6. R.J. Meats and A.W. Starnett, E. I. Fifth Electrical Insulation Conf. (1963), p. 104.
7. T.C. Manley, Trans. Electrochem. Soc., 84, 82 (1943).
8. J.C. Devins, private communication.

**BLANK PAGE**

TABLE II-1  
CORONA DAMAGE TO EICOSANE

v = Corona exposure                      a = Air exposure

Eicosane with Positive Ion Bombardment

<u>Conditions</u>	<u>Counts/Min</u>	<u>% of Original</u>
0 hr	109.8 ± 3.9	100
16 v	80.7 ± 2.9	74.2
16 v, 24 a	47.3 ± 4.1	43.4
16 v, 24 a, 20 v	54.8 ± 4.0	50.2
16 v, 24 a, 20 v, 28 a	45.4 ± 4.0	41.7
16 v, 24 a, 20 v, 28 a, 68 v	39.4 ± 4.0	36.1

Eicosane Exposed to Air

0 hr	125.0 ± 4.0	100
16 a	54.6 ± 3.4	43.7
40 a	31.1 ± 3.9	24.9
60 a	29.1 ± 3.8	23.3
88 a	23.6 ± 3.8	18.8
156 a	15.2 ± 3.8	13.2

TABLE II-2  
CORONA DAMAGE TO EICOSANE

	<u>Time (hr)</u>	<u>Total Counts</u>	<u>Background</u>	<u>Net Counts</u>	<u>Counts/Min</u>	<u>% Retained</u>
I	0	5998	1317	4681	234 ± 5	100
	4	5645	1304	4341	217	93
	8	5638	1286	4352	217	93
	23	5187	1308	3879	194	83
	47	4790	1356	3364	168	72
	119	4093	1383	2700	125	58
	139	3605	1464	2141	107	46
	193	3166	1453	1713	88	37
	266	2886	1418	1468	73	31
II	0	2713	1263	1450	72 ± 4	100
	24	2364	1354	1010	50	70
	48	2280	1362	918	48	64
	145	2213	1433	780	39	54
	169	2092	1450	642	32	44
	219	1826	1440	386	19	26
	315	1789	1461	328	16	22
III	0	3958	1380	2578	129	100
	1	3813	1433	2380	119	92
	4	3655	1455	2200	110	85
	19	2680	1460	1220	61	47
	24	2529	1442	1087	54	42
	46	2418	1445	967	48	41
	74	2220	1494	726	36	28
	96	2047	1467	580	29	22
	118	1988	1480	508	25	19

I = Electron bombardment

II = Blank

III = Ion bombardment

TABLE II-3  
TOWNSEND PULSE BOMBARDMENT OF DOTRIACONTANE FILM

9-mil air gap; 1.48 kv

	<u>Aging Time (min)</u>	<u>Counts/Min</u>	<u>% Retained</u>
I	0	974 $\pm$ 12	100
	60	969	100
	1,020	992	102
	4,080	972	100
II	0	971 $\pm$ 12	100
	120	1,000	103
	1,320	995	102
	9,960	1,085	112
	17,160	1,112	115

I = Electron bombardment

II = Ion bombardment

TABLE II-4  
ELECTRON AND ION STREAMER DISCHARGES ON DOTRIACONTANE

15-mil gap; 7.3 kv

<u>Aging Time (min)</u>	<u>Electrons (counts/min)</u>	<u>Ions (counts/min)</u>
0	220	110
1,025	166	
1,213		114
2,165	155	
2,481		112
7,111		67
8,166		64
9,365	127	
9,408		60
15,125	124	
19,248		42
20,885	122	

100

TABLE II-5  
STREAMER BOMBARDMENT OF DOTRIACONTANE.  
STAGNANT AIR IN CELL

30-mil gap; 7.3 kv

<u>Aging Time</u> (min)	<u>Electrons</u> (counts/min)	<u>Ions</u> (counts/min)
0	116	97
120	120	103
240	115	102
1200	80	71
5100	63	53
6113	62	48
7478	60	53
8678	58	54

TABLE II-6  
STREAMER BOMBARDMENT OF DOTRIACONTANE.  
FLOWING AIR THROUGH CELL

<u>Aging Time</u>	<u>Ion</u> <u>Bombardment</u>	<u>Electron</u> <u>Bombardment</u>
0	153	84.7
150	155	88.6
270	144.6	77.5
420	140.4	62.7
600	131.	67.
750	116.8	60.3
990	108.7	52.7
1140	103.6	54.1
1405	86.7	48.5
2320	79.1	50.7
2320	34.0	22.7



TABLE II-7  
NUMBER OF STREAMER PULSES PER MINUTE WITH AIR FLOWING

See Fig. II-14. Dotriacontane

<u>Time (min)</u>	<u>Pulses/Min (negative)</u>	<u>Pulses/Min (positive)</u>
0		
7	437	212
120	490	220
		--Voltage interrupted
170	510	208
200	540	212
		--Voltage interrupted
250	540	214
330	565	328
		--Voltage interrupted
350	369	139
590	445	150
		--Voltage interrupted
650	364	129
695	480	165
800	415	173

TABLE II-8  
STREAM BOMBARDMENT OF RADIOACTIVE  
DOTRIACONTANE IN FLOWING N<sub>2</sub>

<u>Time (min)</u>	<u>Ion Bombardment</u>	<u>Electron Bombardment</u>
0	133.	103.3
6		
166		
180	127	104
190		
240		
310		
320	127	98
335		
435		
670	111.	93.
1580		
1610	86.4	77.9
1610	50.2	51.2
1618		
1728		

TABLE II-9  
AVERAGE VOLTAGE ACROSS A 0.22-mm  
GAP DURING CORONA DISCHARGES

<u>Temp</u> (°C)	<u>Pressure</u> (mm Hg)	<u>Voltage</u> (kv rms)	<u>E<sub>0</sub></u> (kv)	<u>Temp</u> (°C)	<u>Pressure</u> (mm Hg)	<u>Voltage</u> (kv rms)	<u>E<sub>0</sub></u> (kv)
24	285	9.33	3.08	98	760	15.3	7.36
		6.25	2.60			12.4	6.14
		4.6	2.53			9.5	5.78
		3.5	2.18			7.6	3.30
	445	9.33	4.53		200	15.3	4.06
		7.79	4.10			13.4	3.70
		6.25	3.76			10.7	2.66
		4.6	1.51			7.6	2.48
	590	12.5	6.23		400	5.1	2.20
		9.33	5.75			3.1	1.38
		6.25	2.31			15.3	4.88
						11.7	4.08
70	760	18.8	8.14	120	550	7.6	2.24
		15.7	7.50			4.7	2.74
		12.5	7.07			15.3	5.98
		9.33	4.75			12.4	5.26
	290	12.5	2.82		760	9.5	4.84
		9.5	2.72			6.8	4.70
		8.6	2.68			15.3	8.12
		7.6	2.72			13.4	6.76
		6.6	2.84			11.5	7.32
		5.9	2.48			7.6	5.12
		4.7	2.14		400	15.3	7.88
		4.1	2.50			12.4	6.38
	400	15.3	3.84			9.5	5.76
		12.4	3.50			6.6	4.40
		10.3	3.50		550	15.3	8.02
		6.6	3.30			12.4	6.72
		4.8	2.46			9.5	6.48
	550	15.3	4.24			6.6	5.52
		12.4	4.04		760	15.3	8.92
		9.5	3.86			12.4	5.40
		7.6	3.86			9.5	5.70
		4.7	1.06			6.6	3.66

TABLE II-10  
CHANGES IN  $\delta\sigma_a$  AS A FUNCTION OF PRESSURE AND TEMPERATURE

$V_0 = 9.33 \text{ kv (rms)}$

	<u><math>V_s</math> (rms)</u> <u>(kv)</u>	<u>Temp</u> <u>(°C)</u>	<u>Pressure</u> <u>(mm Hg)</u>	<u><math>E_0</math></u> <u>(kv)</u>	<u><math>\delta\sigma_a</math></u> <u>(kv)</u>
Part A	3.5	25	400	4.0	0.9
	3.9	70	400	3.4	2.1
	4.0	98	400	3.3	2.4
	6.3	120	400	5.7	3.2
Part B	2.8	25	285	3.1	0.9
	4.3	25	445	4.5	1.6
	5.3	25	590	5.7	1.8
	7.3	25	760	4.7	5.3

TABLE II-11  
CORONA DAMAGE TO "H" FILM

<u>Pressure</u> <u>(mm Hg)</u>	<u>Temp</u> <u>(°C)</u>	<u>Voltage</u> <u>(kv rms)</u>	<u>Wt Loss</u> <u>(%/hr)</u>	<u>Corona</u> <u>Power (watts)</u>	<u>Rate of Wt Loss</u> <u>(%/w-hr x 10<sup>2</sup>)</u>
400	124	10.3	0.263	2.70	9.75
760	70	18.0	.186	4.0	4.65
760	124	10.3	.168	1.72	9.73
760	22	10.3	.00625	1.2	0.521
760	50	18.0	.0964	3.95	2.44
760	70	10.3	.0567	3.10	1.83
760	22	18.0	.0532	4.10	1.30
760	110	14.0	.183	3.75	4.88
200	124	10.3	.157	3.4	4.62
760	22	14.0	.0187	2.6	0.72
500	22	10.3	.114	--	.785
200	22	10.3	.0125	0.94	1.33

TABLE II-12  
RATE OF WEIGHT LOSS/CORONA ENERGY AT 22° AND 124°C. "H" FILM

<u>Pressure (mm Hg)</u>	<u>Temp (°C)</u>	<u>Voltage (kv)</u>	<u>Rate of Wt Loss/Corona Energy (x 10<sup>2</sup>)</u>
200	124	10.3	4.62
400	124	10.3	9.73
760	124	10.3	9.75
200	22	10.3	1.33
500	22	10.3	0.785
760	22	10.3	.521

TABLE II-13  
LIFE TEST OF INSULATION SYSTEMS

<u>Material</u>	<u>Relative Life* under Corona Attack</u>
Butyl rubber	0.3
Cast polycarbonate resin	.7
Cast oil modified phenolic resin	.9
Epoxy varnish on woven glass	.9
Mylar	1.0
Cast epoxy resin	1.0
"H" Film	1.1
Polyethylene (irrachene)	1.7
Oil modified asphaltic varnish on woven glass	2.2
Teflon loaded with carbon black	4.6
Silicone rubber	500+
Mica	500+

\*The relative listing is based on the life of Mylar, which is 20 hours.

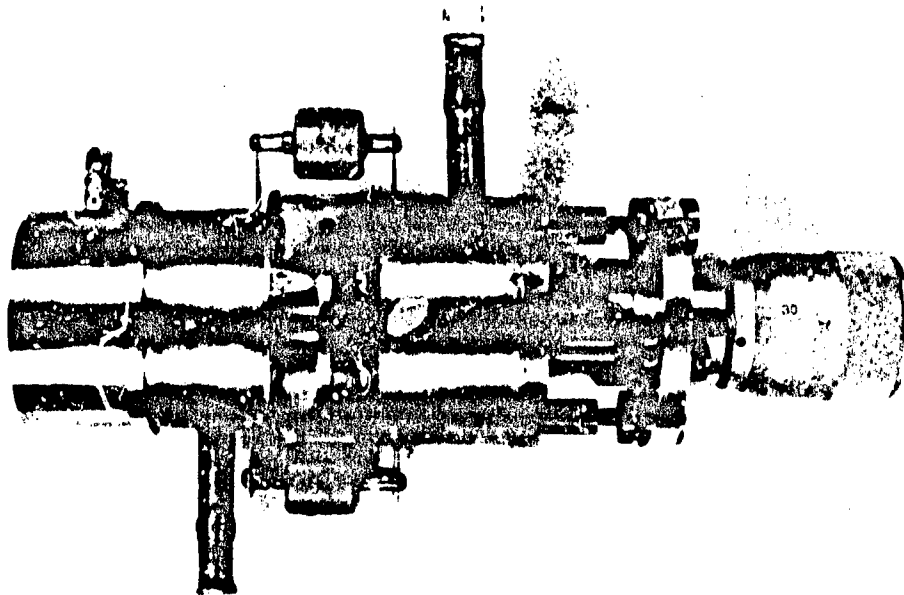


Figure II-1. Corona Cell

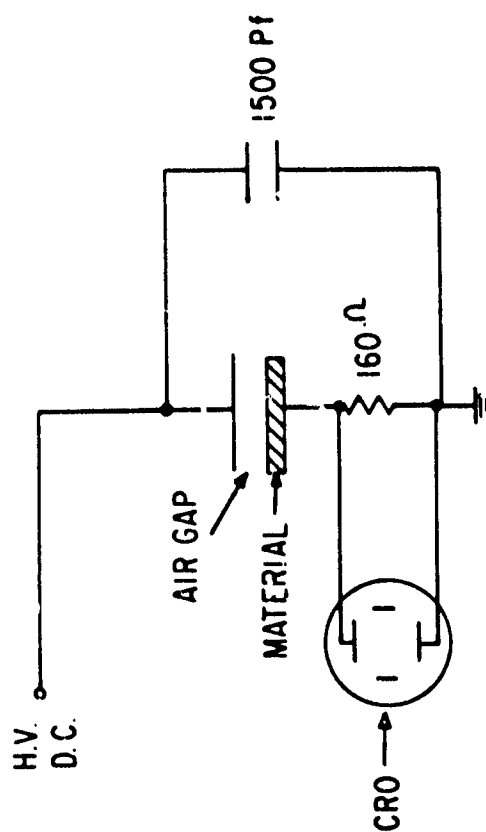


Figure II-2. Schematic Diagram of the Corona Cell and Associated Equipment

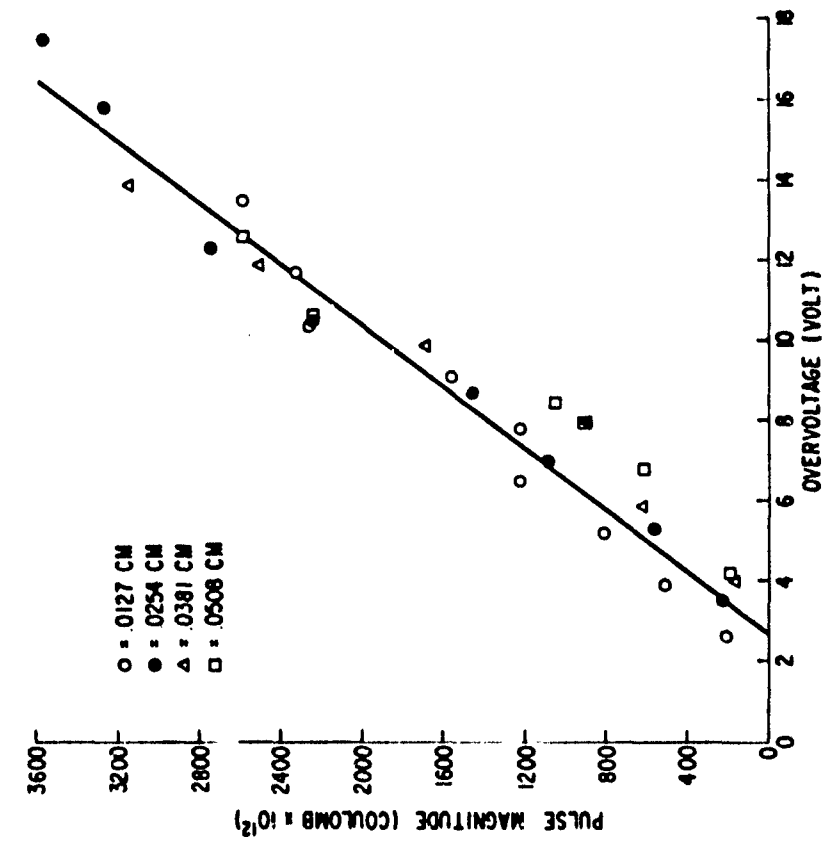


Figure II-3. Dependence of Pulse Magnitude on Overvoltage for Various Electrode Separations.  
Townsend Discharges

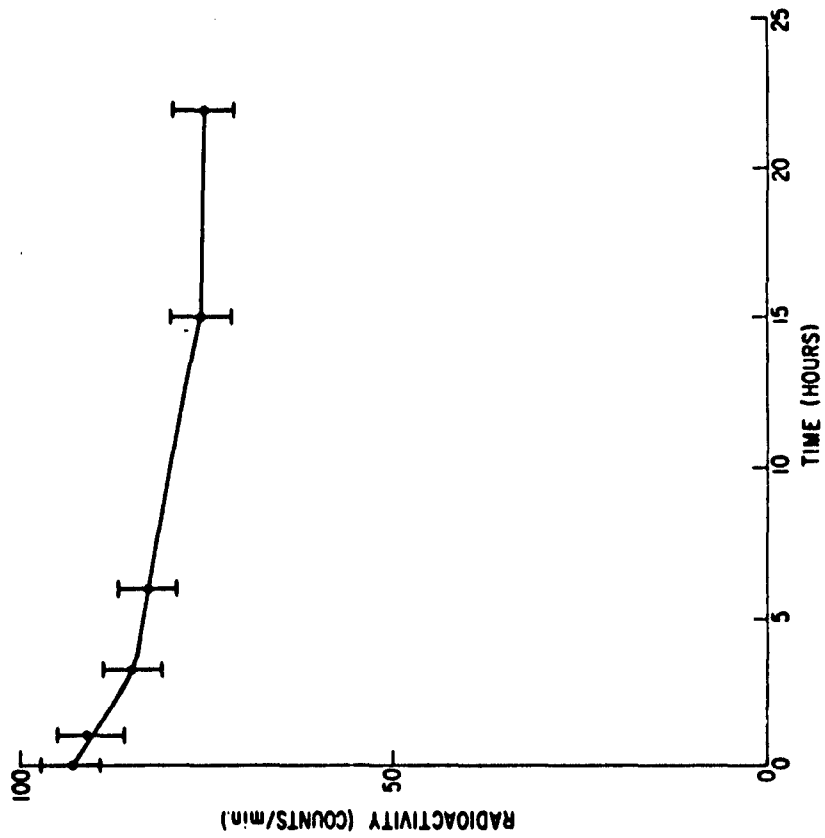


Figure II-4. Positive Ion Bombardment of Stearyl Alcohol: 50 Discharges/Sec; 4 Monolayers.  
Townsend Discharges

**BLANK PAGE**

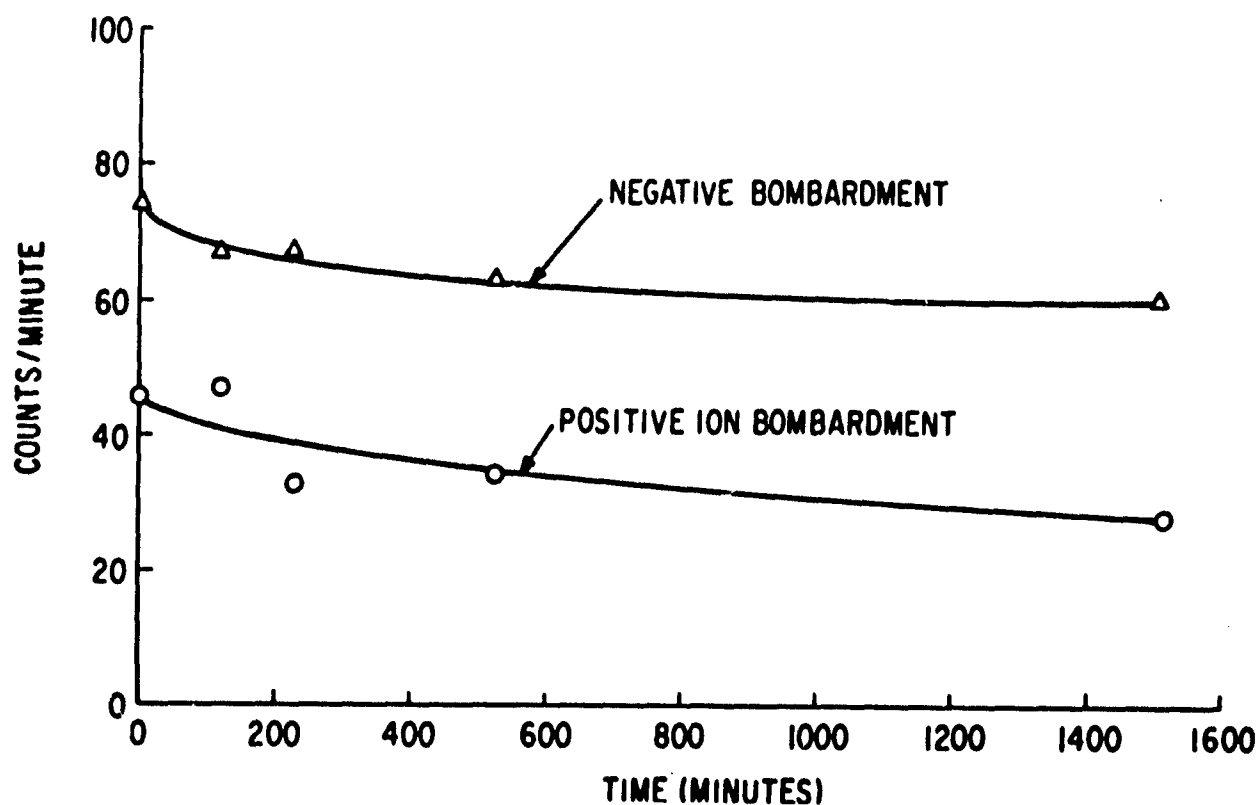


Figure II-5. Corona Damage to Radioactive Stearyl Alcohol. Streamer Discharges; 30-Mil Gap; 7.33 kv

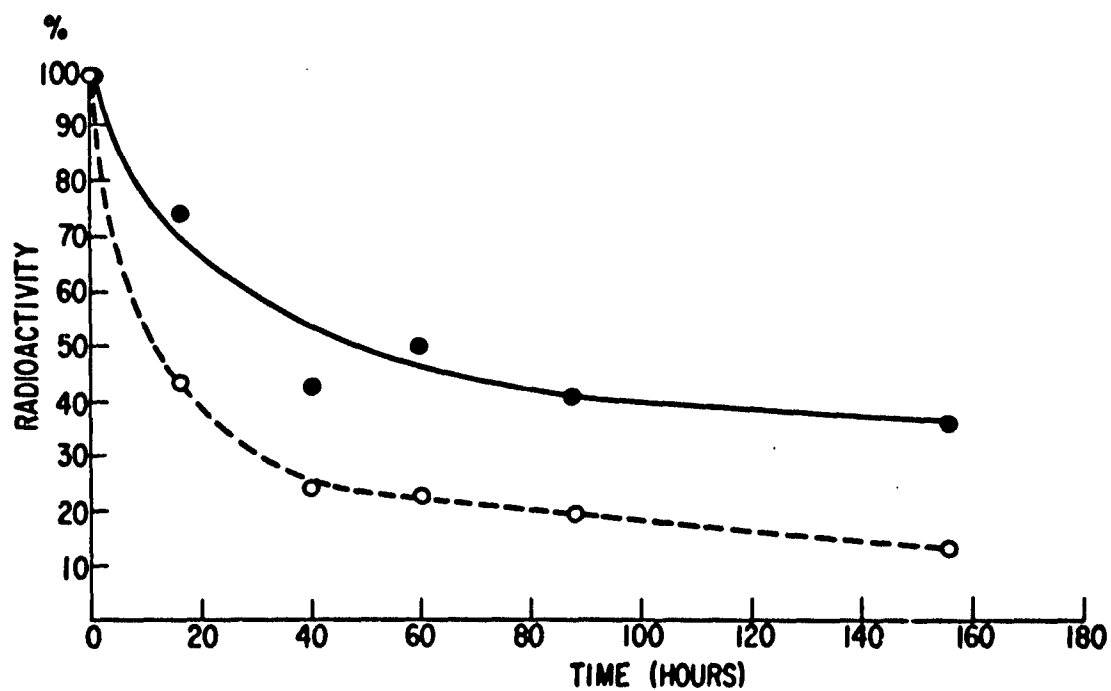


Figure II-6. Corona Damage to Eicosane: O--Air Exposure; ●--Townsend Discharges



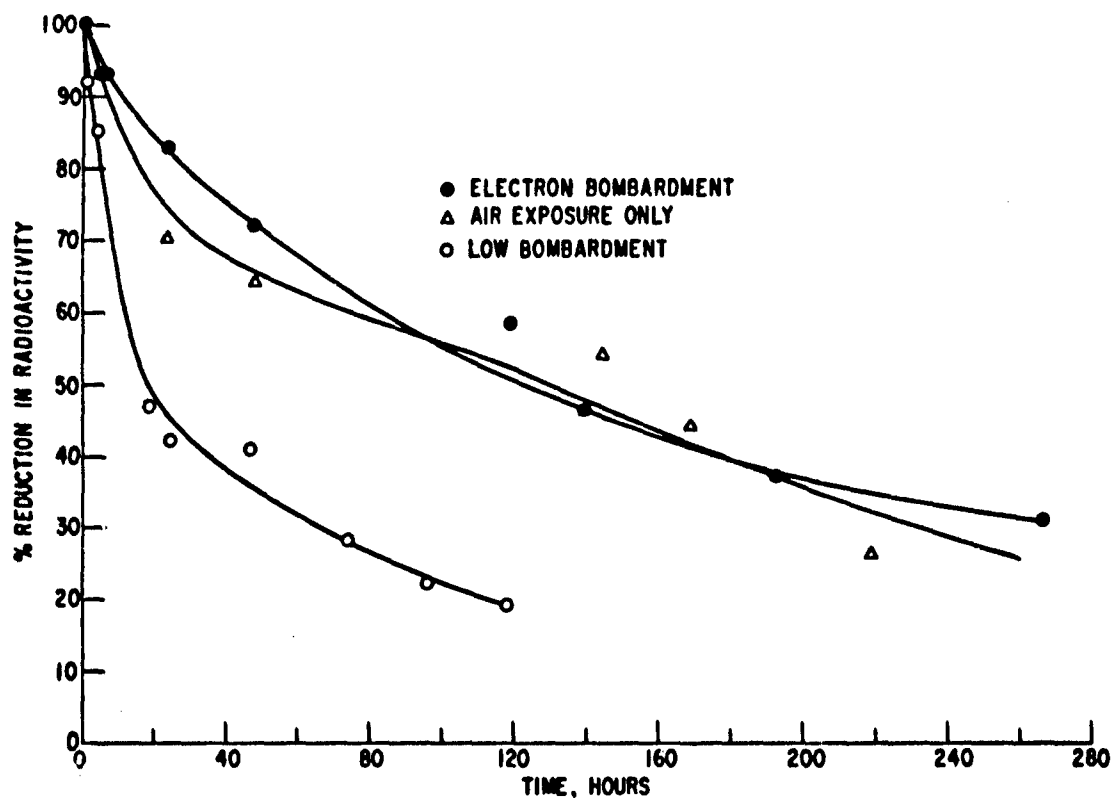


Figure II-7. Per Cent Loss of Radioactivity of Eicosane Film

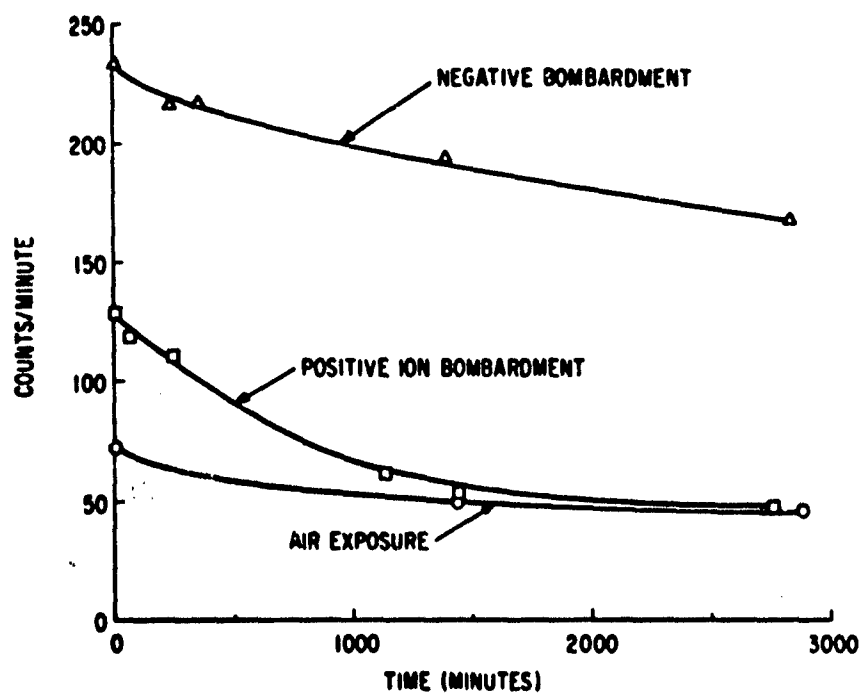


Figure II-8. Absolute Loss in Radioactivity of Eicosane Film with Corona Exposure

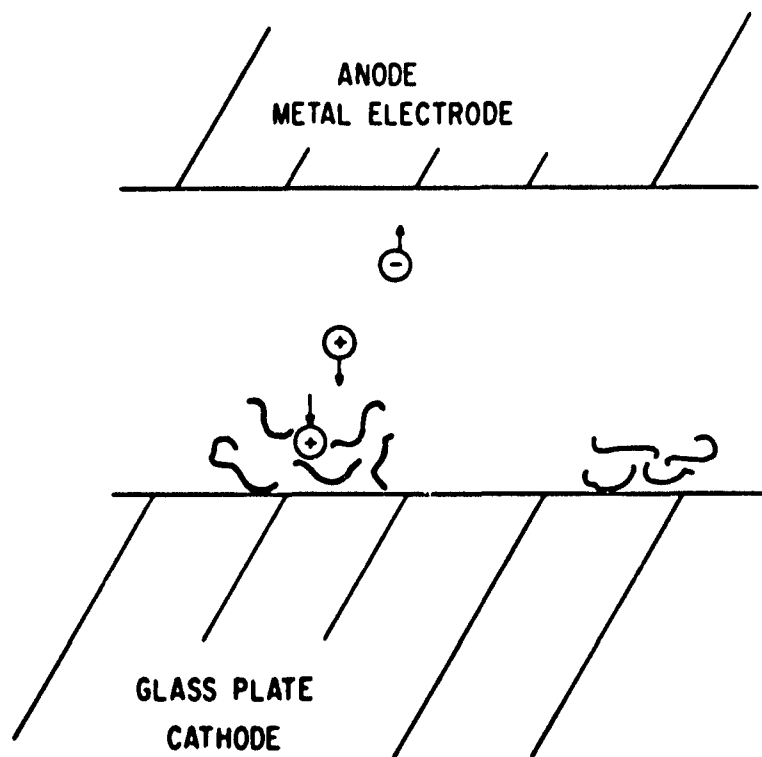


Figure II-9. Morphology of Dotriacontane Films on Glass Plate

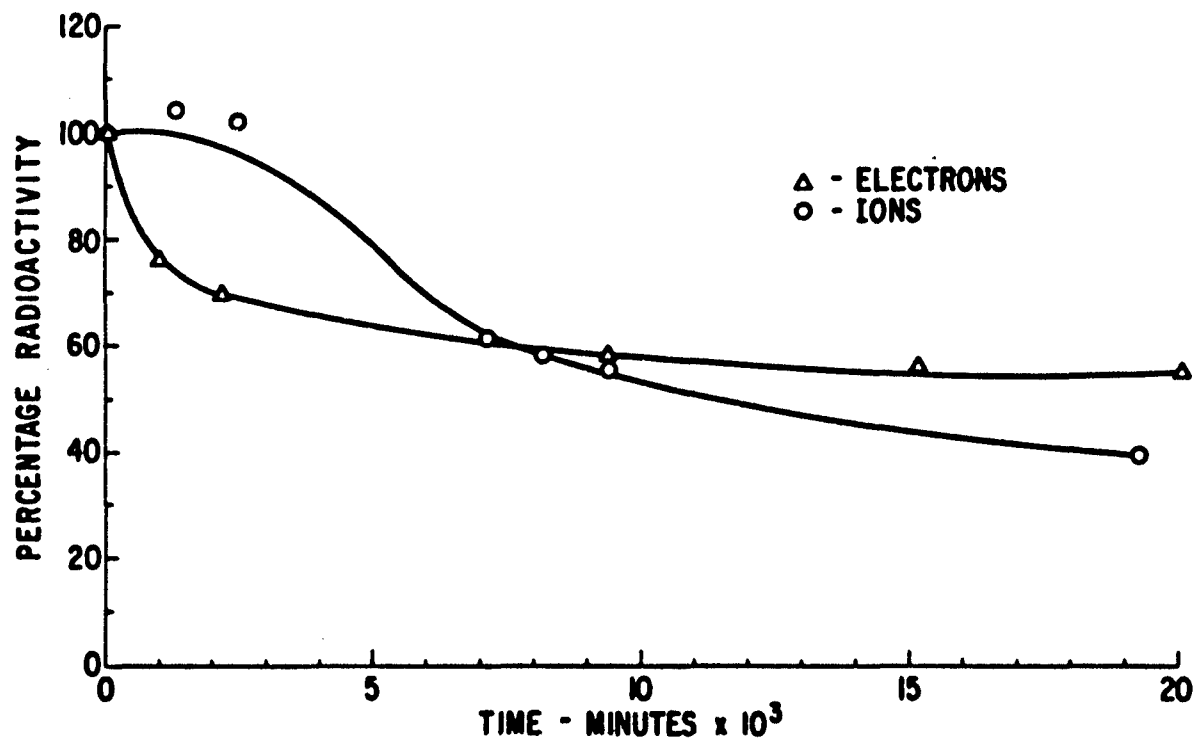


Figure II-10. Electron and Ion Discharges of Dotriacontane: 15-Mil Gap; 7.33 kv



Figure II-11. Discharge Area of Electron  
Bombarded Sample of Dotriacontane 25X

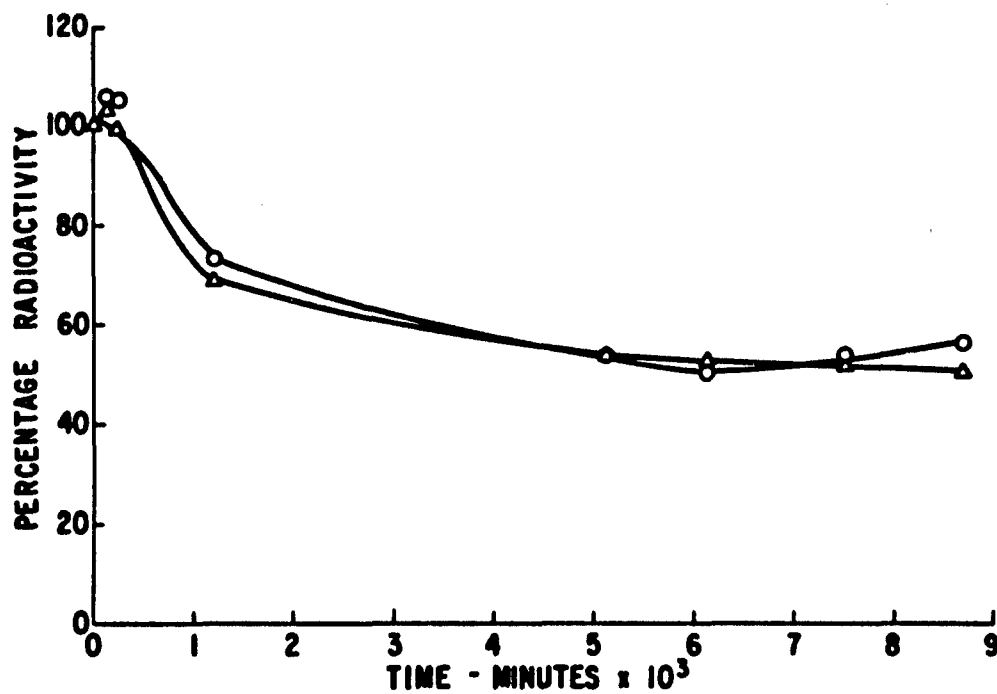


Figure II-12. Electron and Ion Discharges on Dotriacontane:  
30-Mil Gap; 7.33 kv

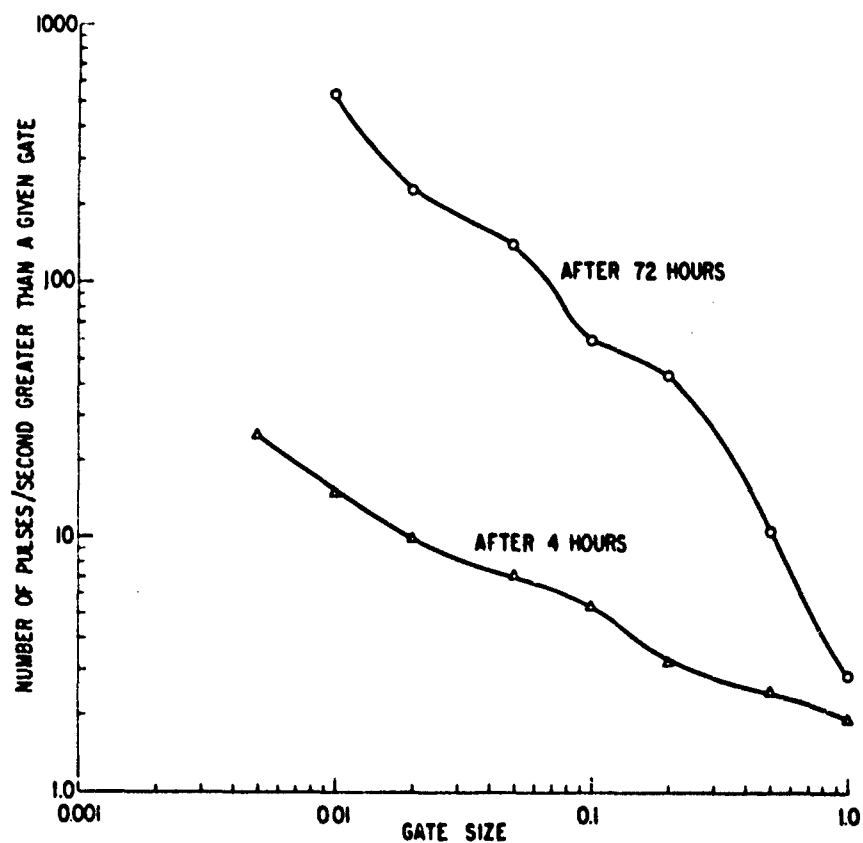


Figure II-13. Change of Pulse Size with Time

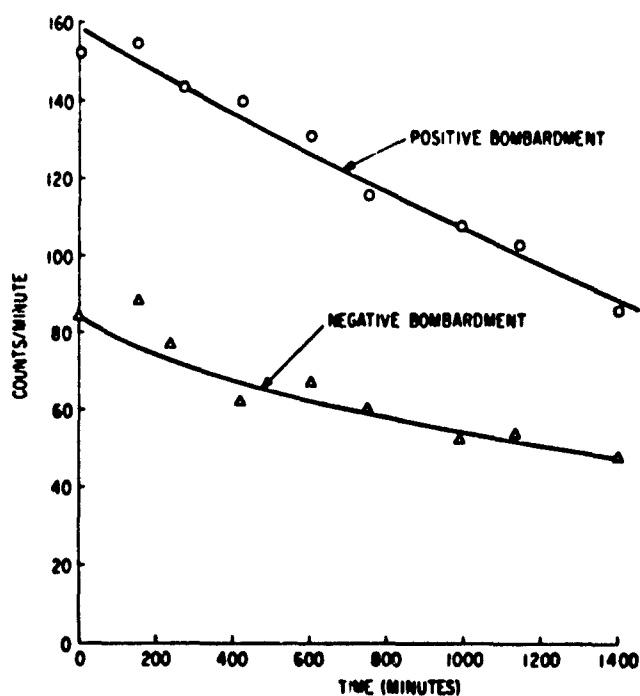


Figure II-14. Steamer Bombardment of Radioactive Dotriacontane. Air Flowing Through Cell

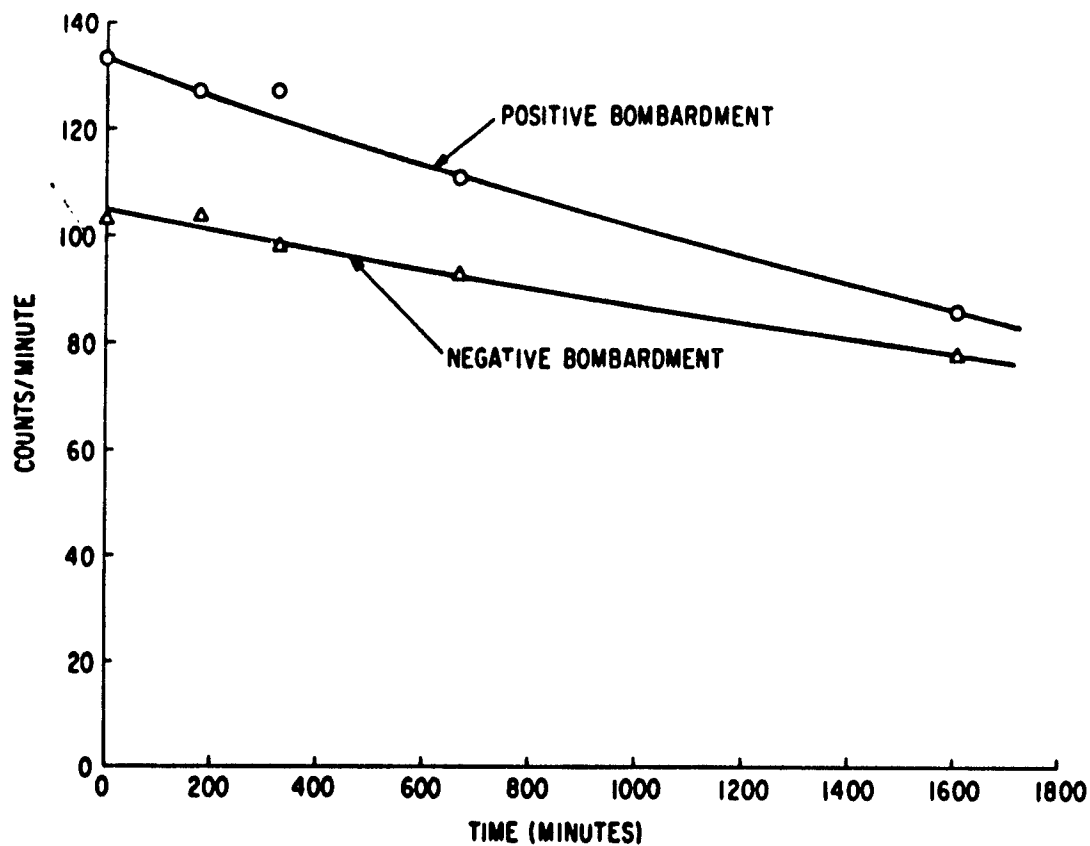


Figure II-15. Streamer Bombardment of Radioactive Dotriacontane.  $N_2$  Flowing Through Cell

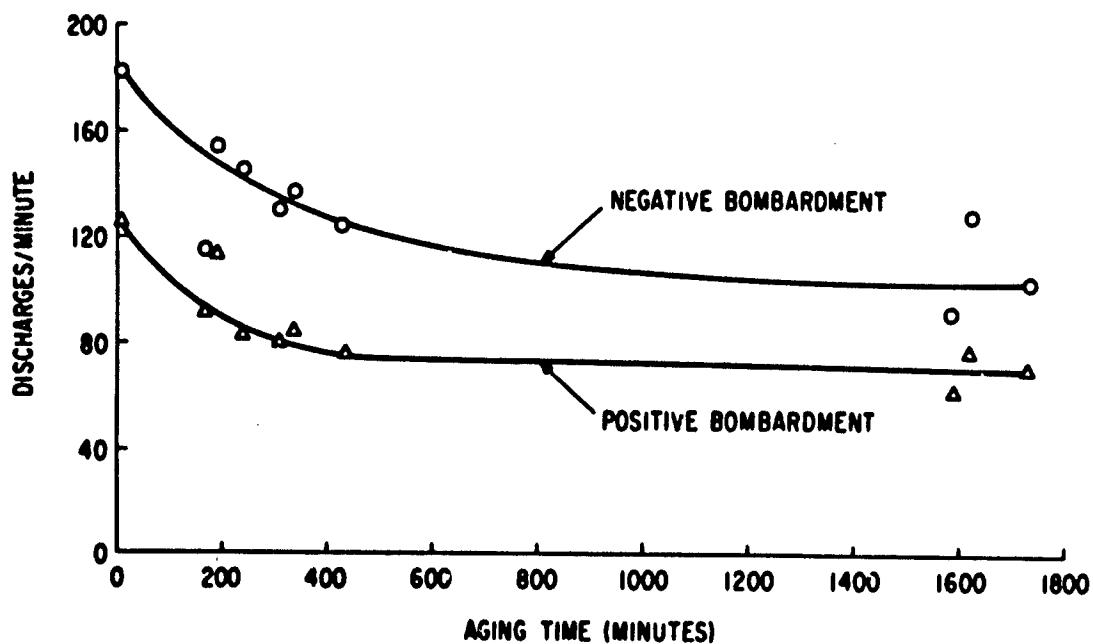


Figure II-16. Number of Discharges Per Minute During Aging Dotriacontane.  $N_2$  Atmosphere

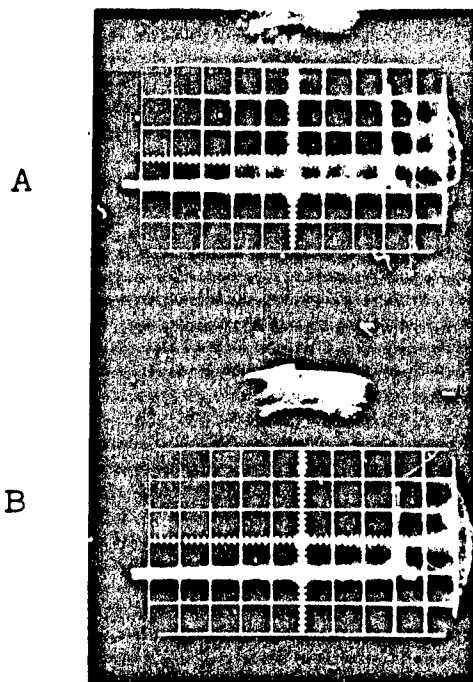


Figure II-17. Pulse Shapes for A--Ion Bombardment; B--Electron Bombardment of Dielectric; 5 volts/cm; 0.5  $\mu$ sec/cm

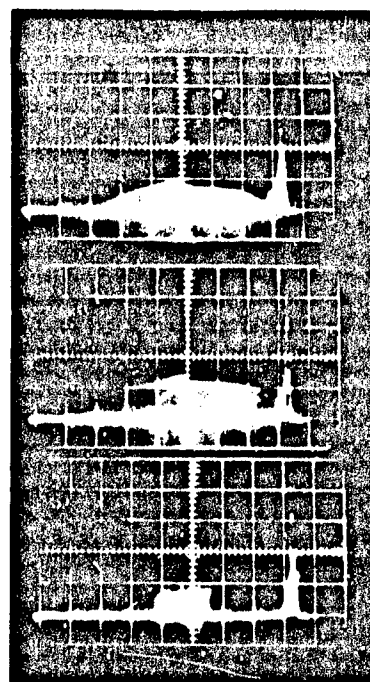


Figure II-18. Pulse Shapes for Ion Bombardment of Dielectric; 5 volts/cm; 0.54  $\mu$ sec/cm

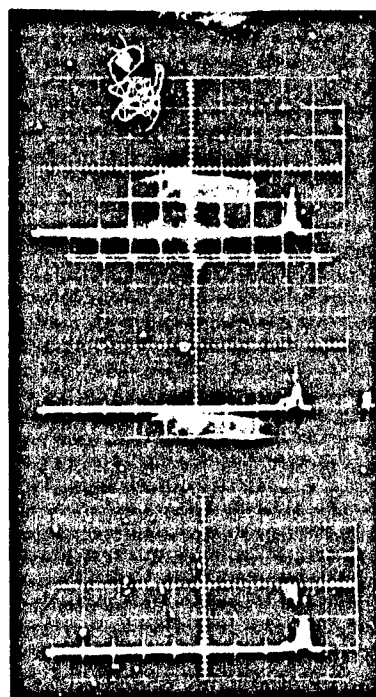


Figure II-19. Pulse Shapes for Electron Bombardment of Dielectric; 5 volts/cm; 0.5  $\mu$ sec/cm

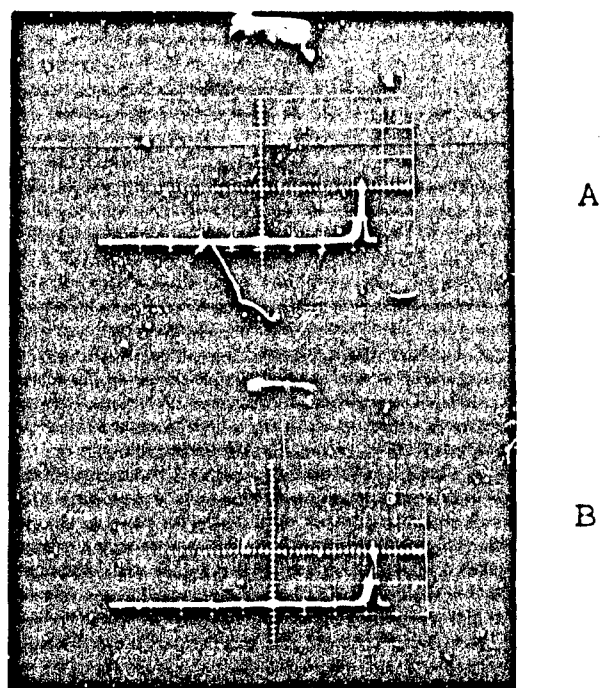


Figure II-20. Pulse Shapes for Ion Bombardment of Dielectric: A--Cell 1;  
B--Cell 2

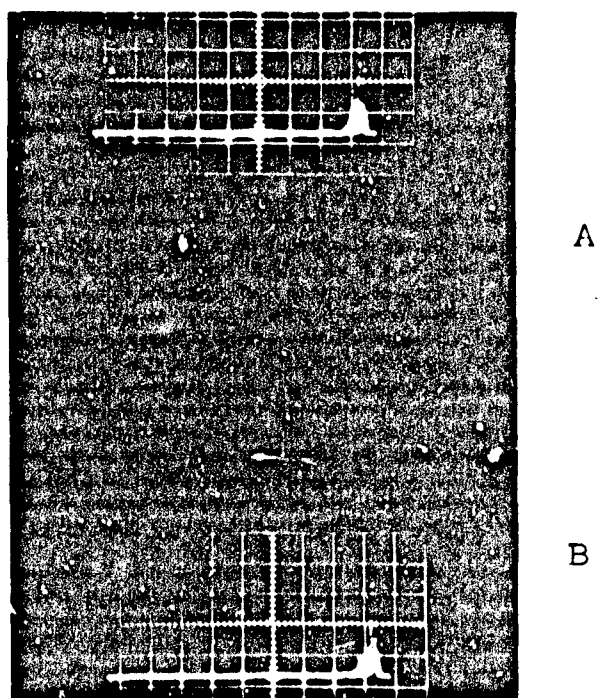


Figure II-21. Pulse Shapes for Electron Bombardment of Dielectric: A--Cell 1;  
B--Cell 2

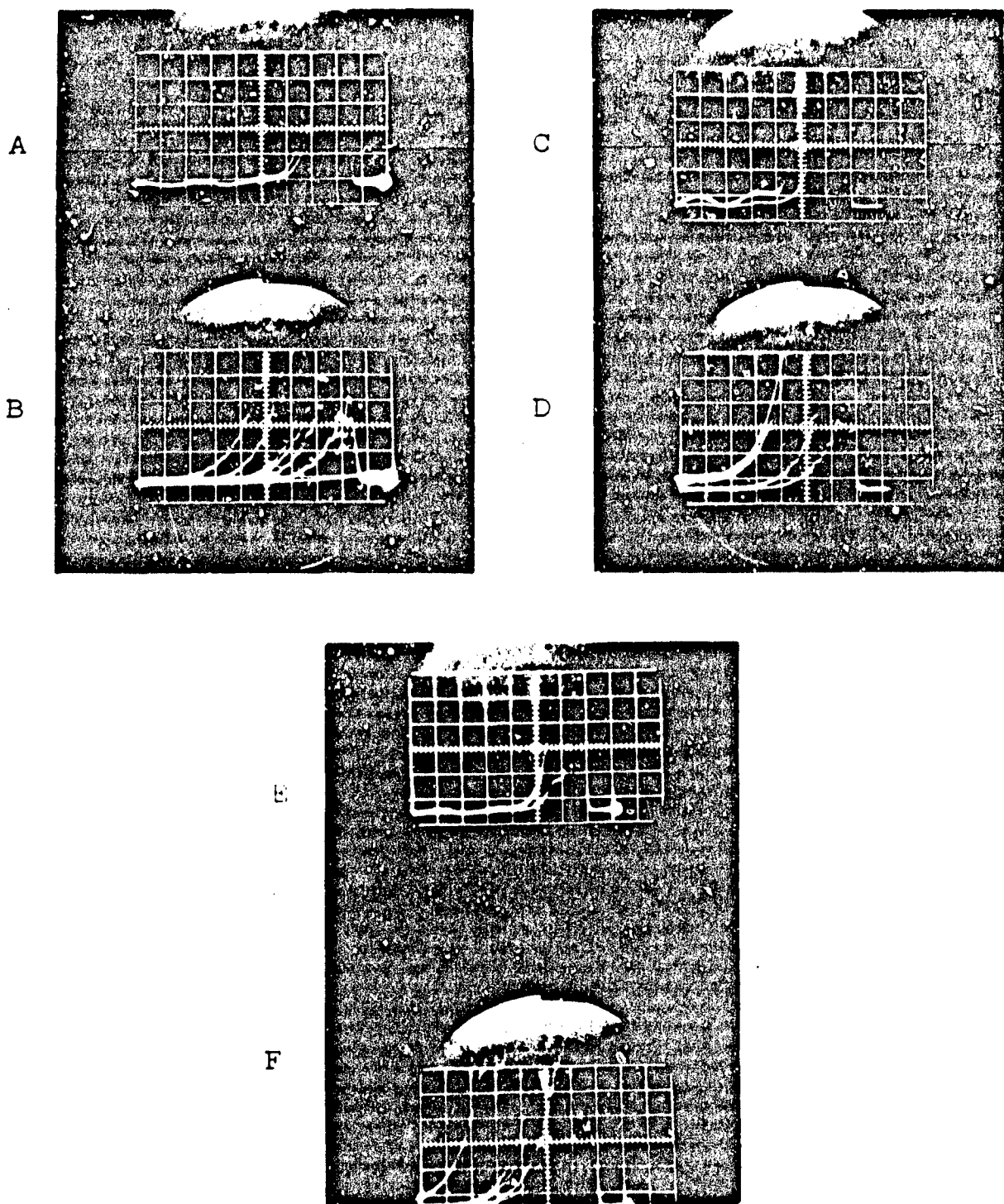


Figure II-22. Streamerlike Discharges on Dotriacontane: A, C, and E are Electron Bombardment; B, D, and F are Ion Bombardment; 0.5 volt/cm; 0.1  $\mu$ sec/cm



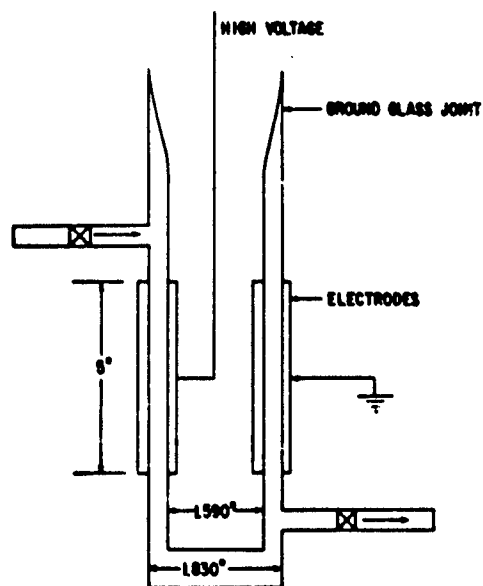


Figure II-23. Schematic Diagram of Coaxial Corona Generator

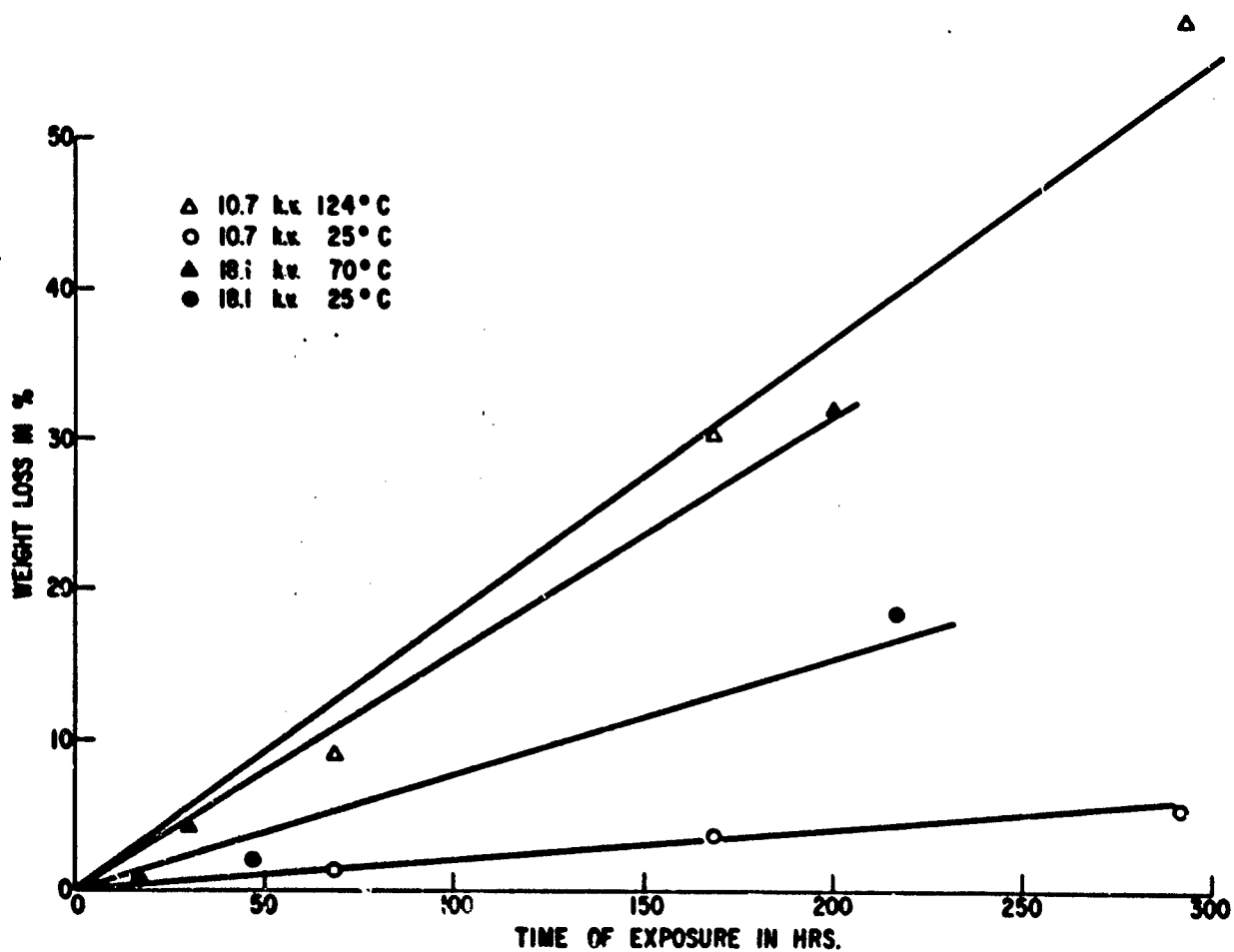


Figure II-24. Weight Loss of Mylar Due to Corona

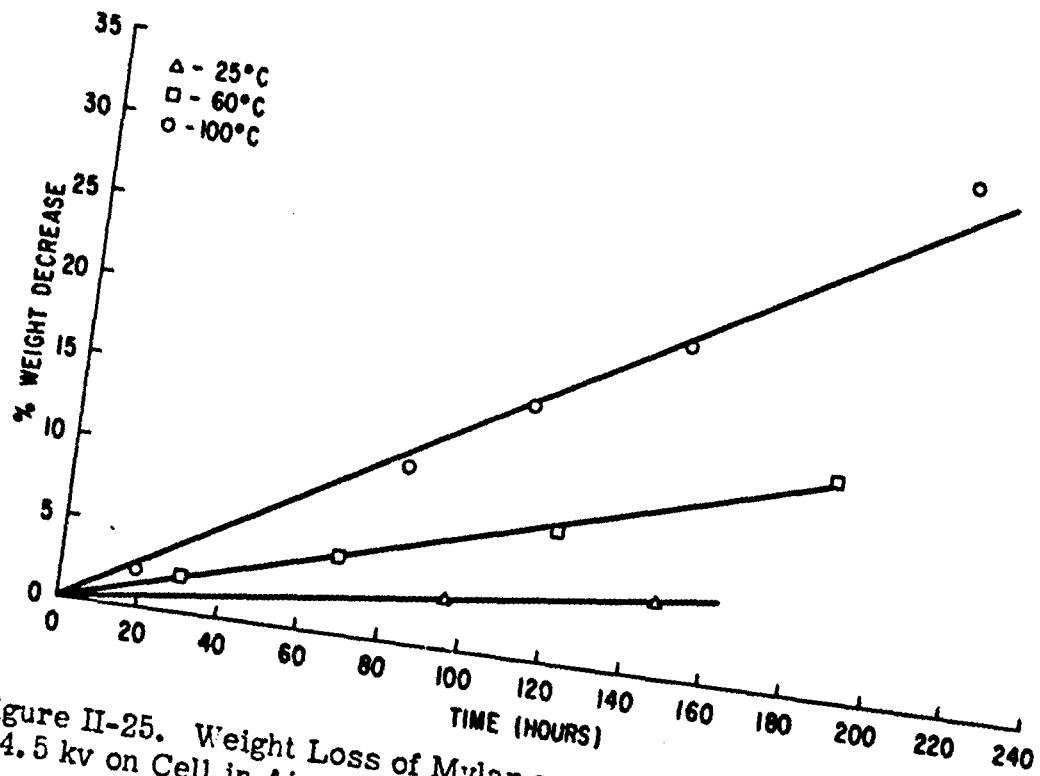


Figure II-25. Weight Loss of Mylar as a Function of Corona Exposure; 14.5 kv on Cell in Air

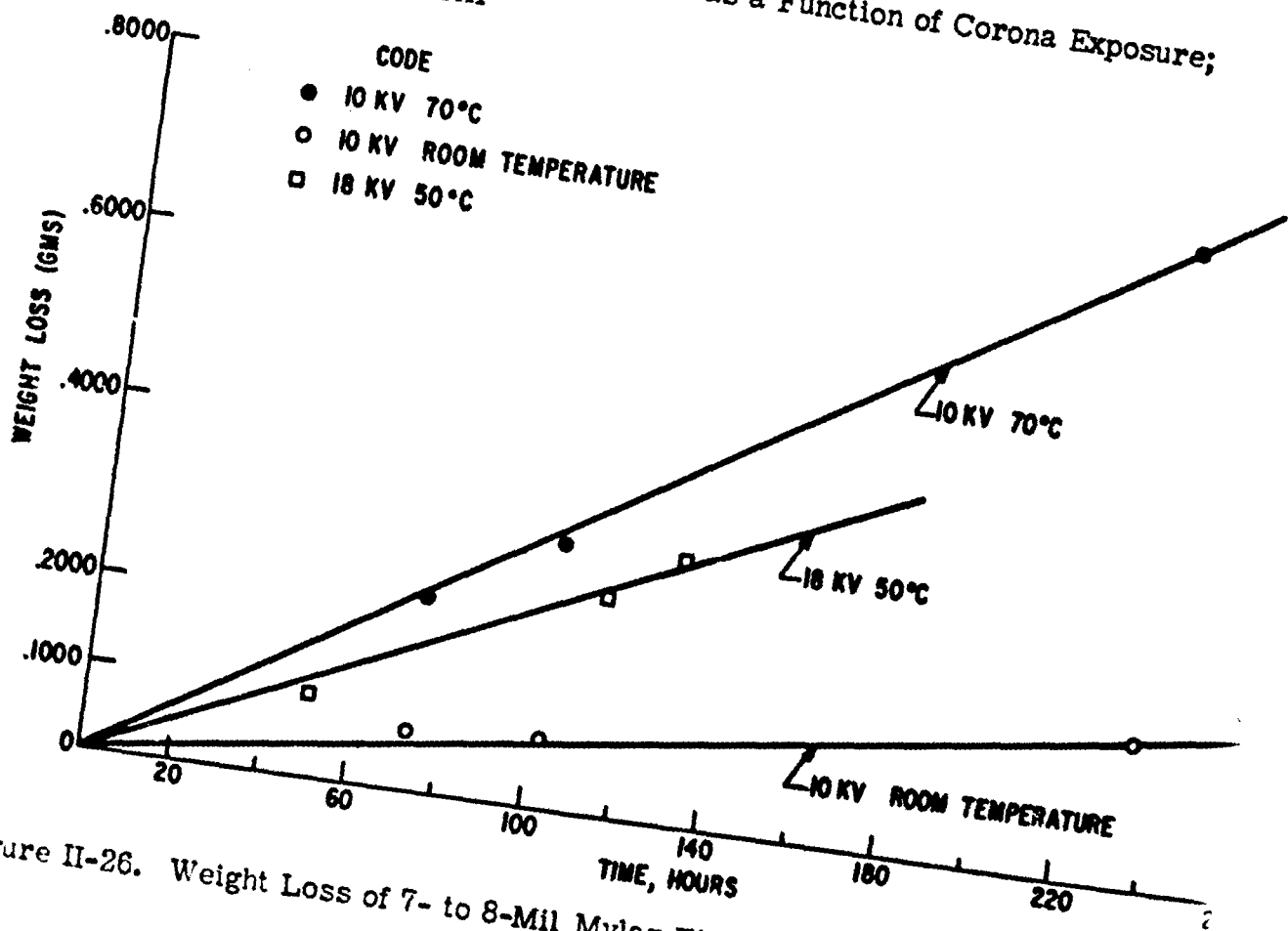


Figure II-26. Weight Loss of 7- to 8-Mil Mylar Film

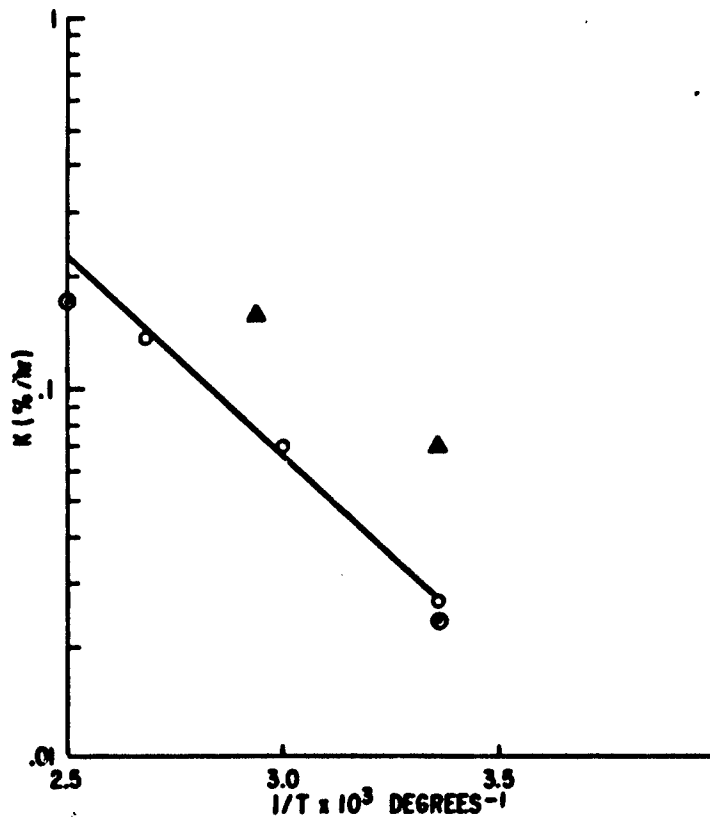


Figure II-27. Weight Loss Rate Constant of Mylar as a Function of Inverse Absolute Temperature; 14.5 kv on Cell in Air (○ 10.7 kv; △ 18.1 kv)

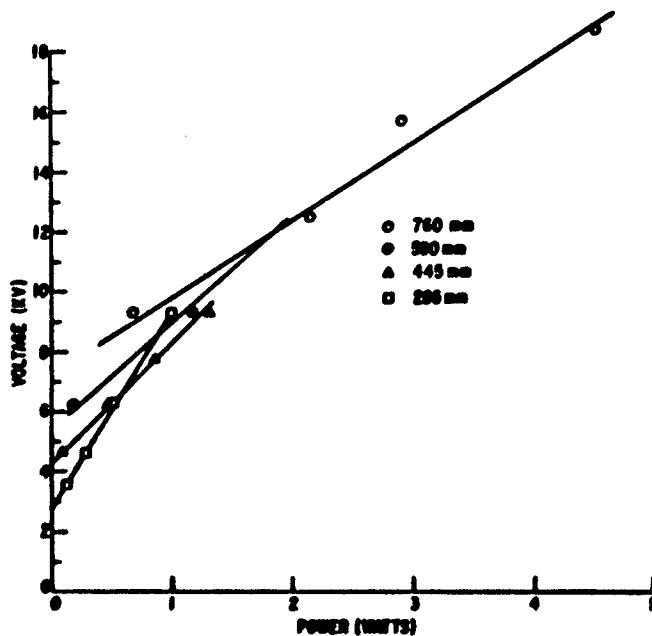


Figure II-28. Corona Energy as a Function of Voltage at 24°C

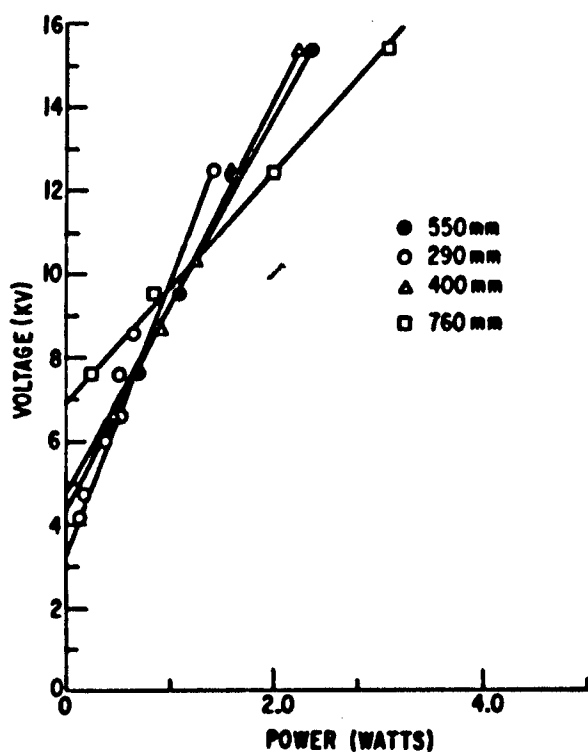


Figure II-29. Corona Energy as a Function of Voltage at 70°C

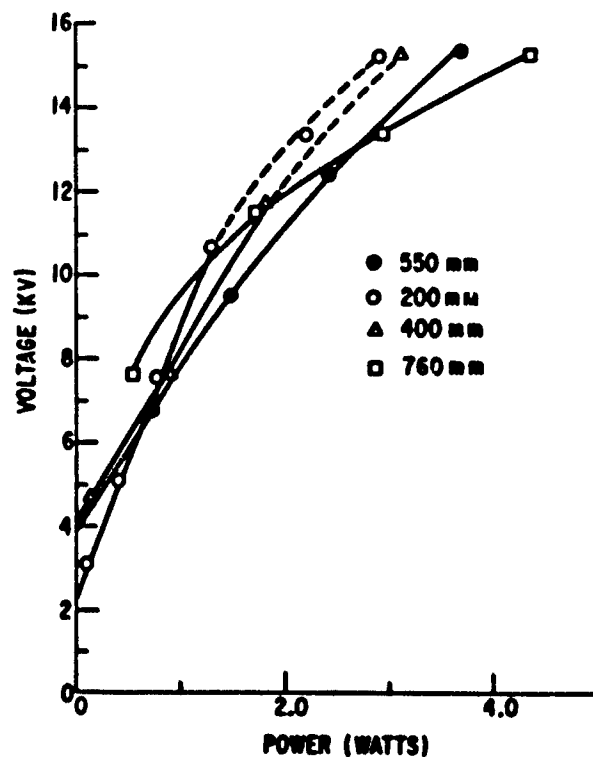


Figure II-30. Corona Energy as a Function of Voltage at 98°C

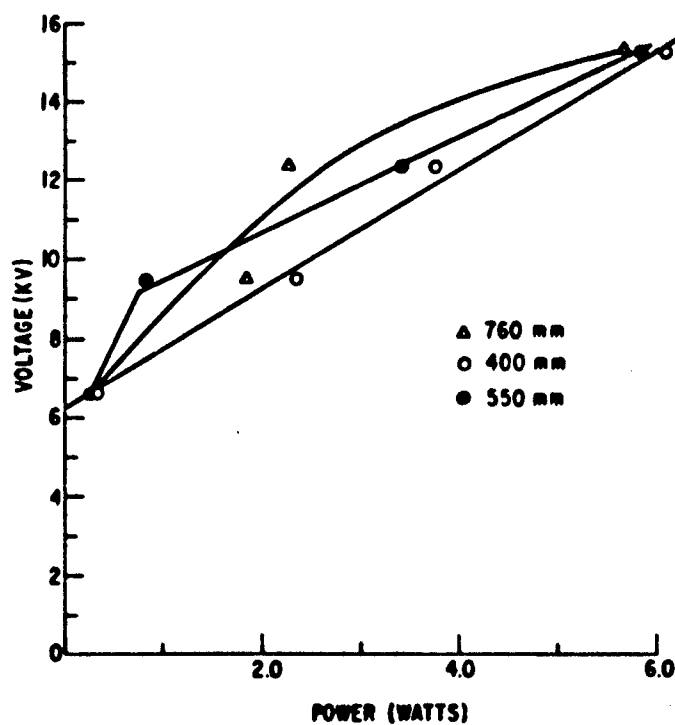


Figure II-31. Corona Energy as a Function of Voltage at 120°C

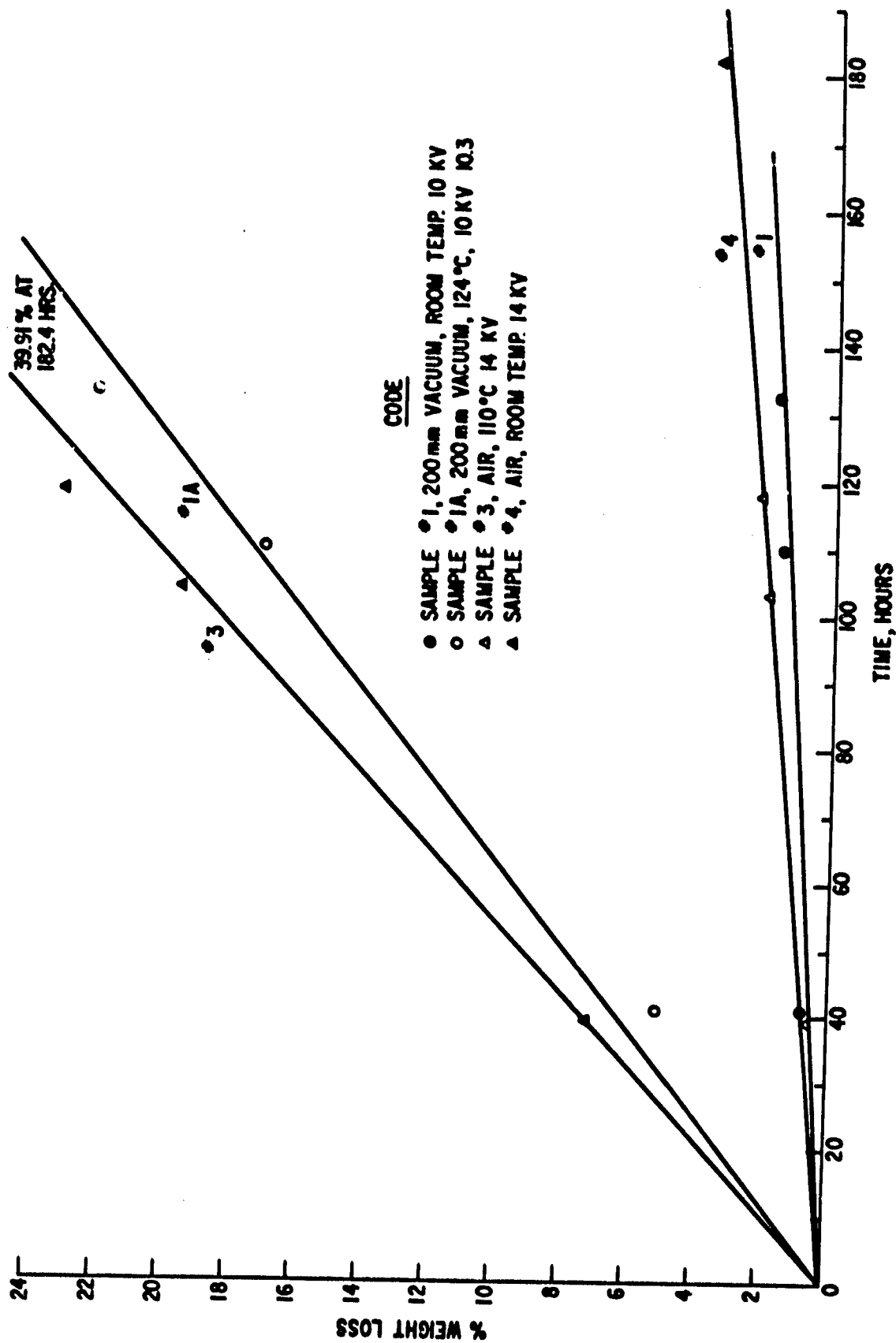


Figure II-32. Weight Loss of "H" Film

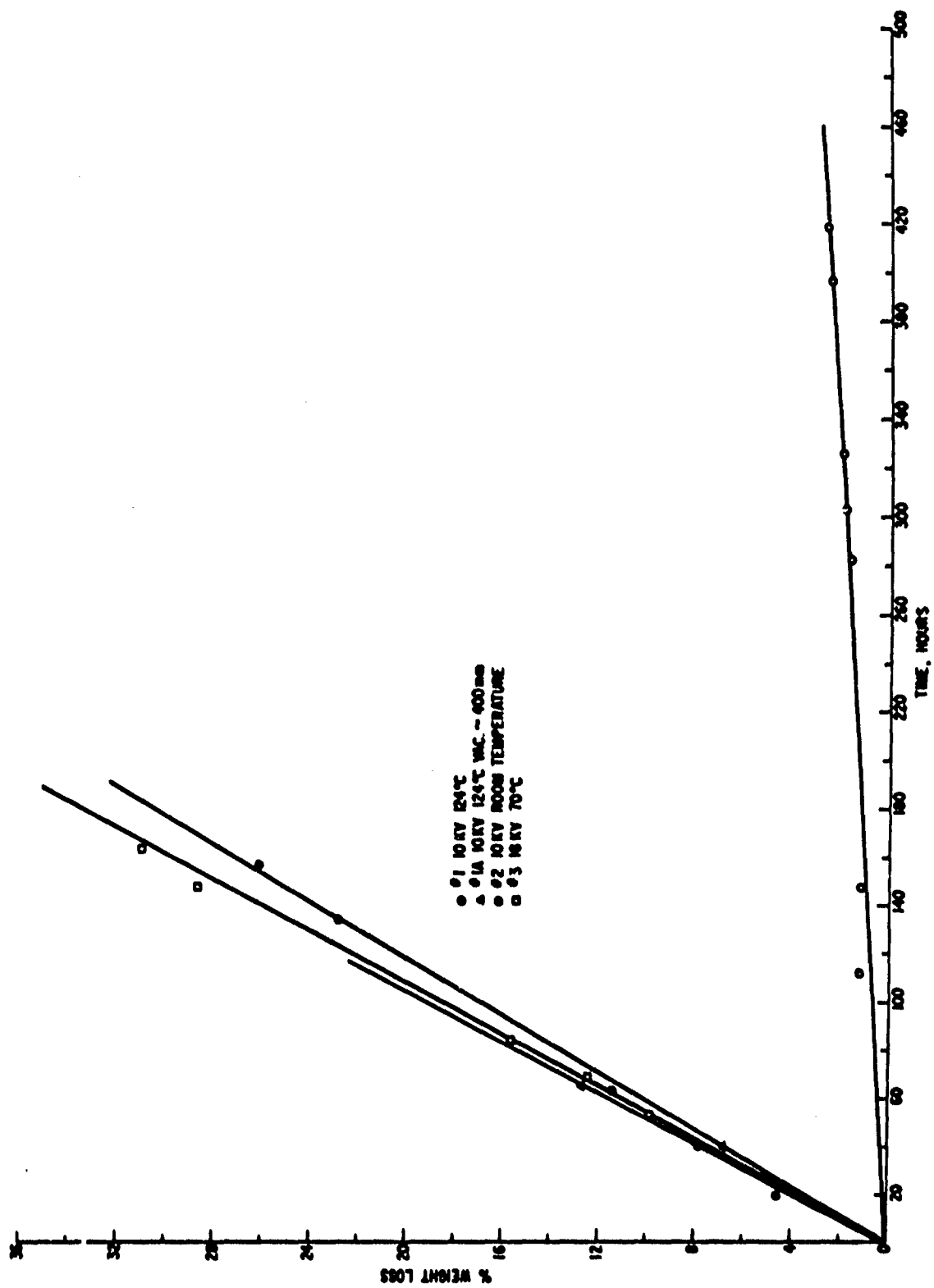


Figure II-33. Weight Loss of  $H_2$  Film

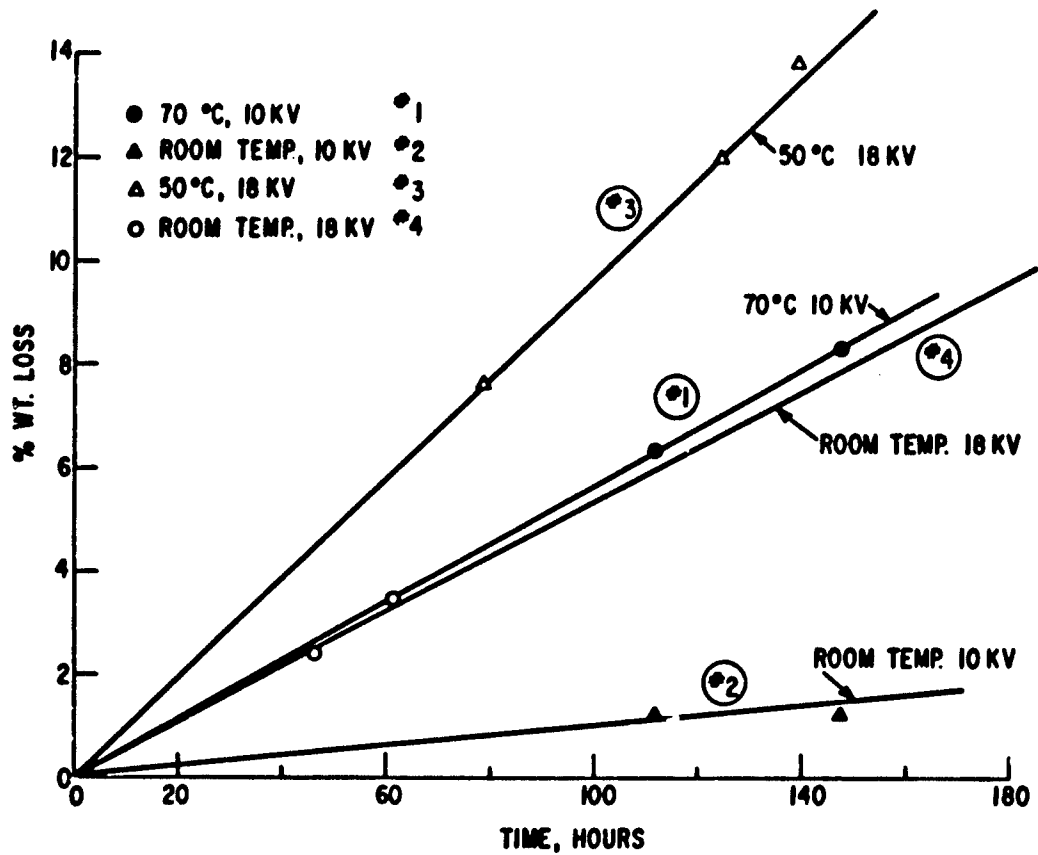


Figure II-34. Weight Loss of "H" Film

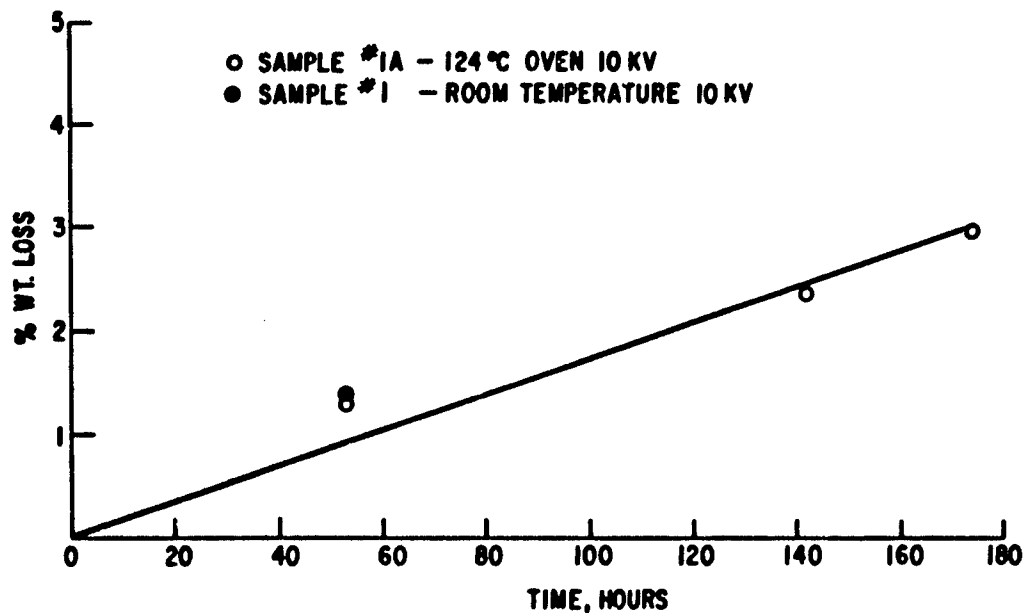


Figure II-35. Weight Loss of "H" Film at 10 kv; 500-mm Vacuum

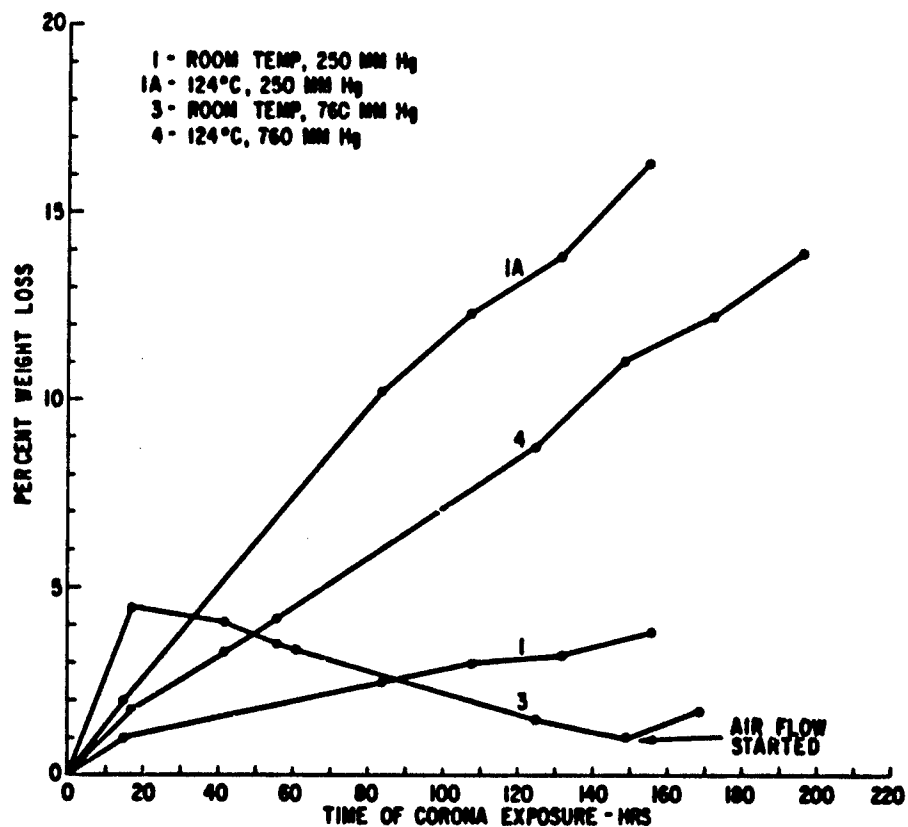


Figure II-36. Weight Loss of "H" Film at 10.3 kv

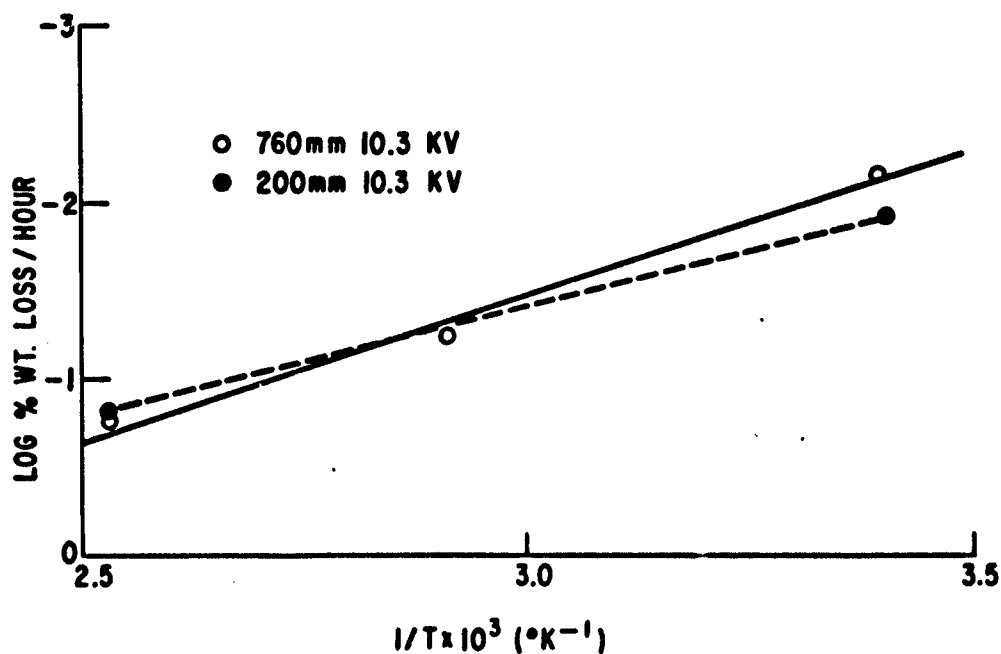


Figure II-37. Per Cent Weight Loss of "H" Film as a Function of Temperature and Pressure



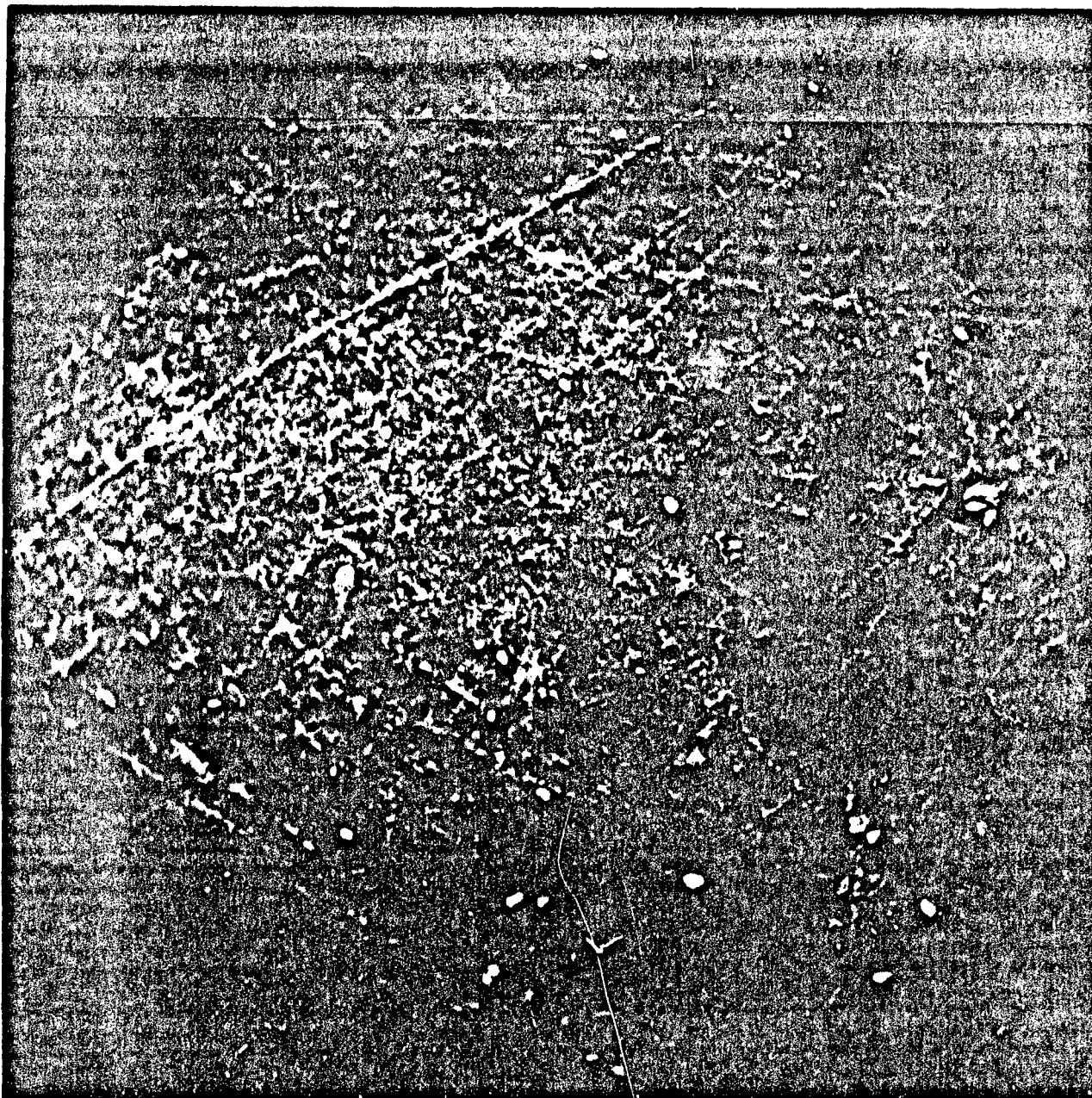


Figure II-38. Corona Damaged "H" Film Surface

110X

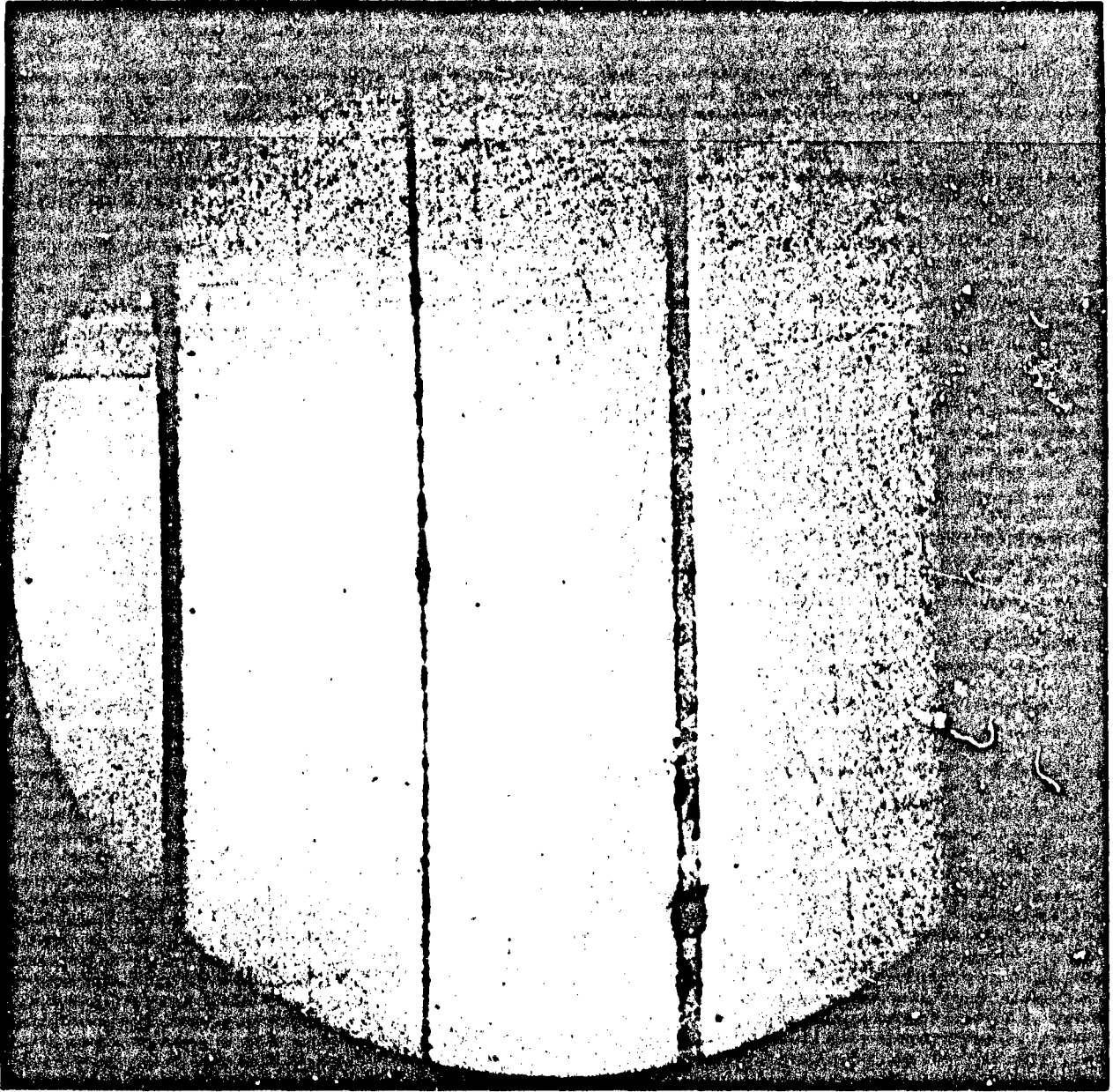


Figure II-39. Corona Damaged "H" Film Edge

110X

**BLANK PAGE**

## C. SUMMARY AND CONCLUSIONS

H. G. Pfeiffer

The purpose of this contract and the previous one was to upgrade the performance of insulating materials under corona conditions. The approach was twofold: a study of the exact nature of the corona discharges, and the study of the mechanisms of corona damage. It was hoped that these two parts could then be reconciled and recommendations for the use of insulation be made. To a large extent we have managed to do this.

Corona is a type of gas discharge; it is differentiated from other types by its self-extinguishing nature. It can take place only in systems where some form of current limitation exists, e. g., insulation in series with the gas space, highly divergent fields, or a high impedance voltage source. We will be concerned with the first case as embodied in a solid insulation system with accompanying voids subjected to high fields.

As was demonstrated in the previous contract No. AF-33(616)-7485, the nature and size of the discharges may be classified broadly into two categories: "Townsend" and "streamer." In a given insulation system, either type can take place depending on the specific conditions; transitions from one to the other are frequently observed. The total amount of charge carried across an insulated gap during a half-cycle of a-c voltage is almost the same, but the distribution in the discharge space is quite different and could well affect the degree of damage done to the gap insulation. This latter question is one of the major ones Phase II of this contract was designed to answer.

When the insulation has a surface resistivity of greater than  $10^{10}$  ohms/sq, streamers usually occur. This process is described in ASD Technical Report No. 61-693, pages 16 through 26. In the absence of overvoltage and at surface resistivities in the interval  $10^6$  to  $10^8$  ohms/sq, Townsend discharges occur as described on pages 7 through 16 of the above report. A third type of discharge will occur when the surface becomes even more conducting ( $<10^6$  ohms/sq) and enough current flows to produce a glow discharge or arc.

One of the objectives of the present study was to determine the relative effects of the Townsend and streamer-type discharge. The study has found that the streamers produce more damage largely because of the greater energy density. The damage caused by the glow discharge type of phenomena is so great that it is unlikely that any organic system can be maintained very long in their presence. Normally, we have avoided this kind of discharge in our studies reported herein.

One of the damaging effects of both Townsend-like and streamer discharges can be a continual reduction in surface resistivity. Elimination of these discharges removes one source of the changes that can lead to the development of glow discharges and arcs. Use of materials that do not degrade to produce lower resistance surfaces is another approach.

The elimination of discharges can be accomplished by designing a system so that electric fields of sufficient magnitude to produce breakdown do not appear across gaps. The best approaches are: (1) filling any gaps completely with solid insulation; (2) coating the surface of insulation with a low resistance coating that is kept at ground potential, and (3) encapsulating with a high-pressure gas or liquid and thereby increasing the breakdown strength of the gaps.

For various reasons, systems have to be built to tolerate corona discharges. When this is the case, a satisfactory system can usually be designed in one of the following ways: (a) the use of a glass or other inorganic material not changed by the discharges or discharge products; (b) the use of an inorganic material as a filler, which can form a corona resistant surface layer, or (c) the incorporation of a material that on reaction forms an inert layer. Silicone rubber and silicone coatings are examples of materials that have a very inert surface due to the  $\text{SiO}_2$  formed in the discharge. Butyl rubber heavily loaded with  $\text{Al}_2\text{O}_3$  and Glyptal resin loaded with  $\text{Fe}_2\text{O}_3$  are examples of materials that end up with resistant surface coatings. Systems protected according to the above methods have operated successfully under corona conditions for many years.